ABSTRACT

Title of Dissertation: ADSORPTION AND MECHANISTIC STUDIES OF DIMETHYL METHYLPHOSPHONATE FOR CWA DEFEAT

Kim L. Huynh, Doctor of Philosophy, 2018

Dissertation Directed By: Professor Bryan W. Eichhorn, Department of Chemistry and Biochemistry

This thesis work systematically investigated carefully designed ASZM-TEDA deconstruction–reconstruction experiments. Our objective is to understand the role of each impregnant, the factors that influence filter performance, and filter lifetime. Chemical warfare agent simulant, dimethyl methylphosphonate (DMMP), is used to evaluate the adsorption properties and reactivity of different materials using a temperature programmed desorption (TPD)/quantitative ^{1}H-NMR method, combined with inductively coupled plasma-atomic emission spectroscopy (ICP-AES) bulk analysis.

Our investigation begins with a full analysis of the current commercial gas mask filter, ASZM-TEDA. In Chapter 2, studies with ordered mesoporous carbons (OMCs) and a disordered microporous carbon (BPL) reveal that surface area and pore volume dictate total adsorption loading. It was also discovered that an ordered

pore network would lead to higher DMMP desorption energies by 30–40%, confirming stronger binding to the carbon surface in pores ≤2.4 nm. In Chapter 3, our investigation of an ASZM-TEDA deconstructed analog, carbon/CuO, further our understanding of CuO functionality within the adsorbent. Our study reveals that CuO impregnation increases adsorption capacity (up to 64%) in comparison to native carbon adsorbents. The CuO surface activity (reported as DMMP area capacity) was over 3.5 times higher in comparison to the OMCs (0.075–0.078 m^2 g^{-1}), and 17 times higher than BPL (0.016 m^2 g^{-1}). In addition, the extent of DMMP decomposition is greater for nano sized endo-pore CuO relative to larger exo-pore CuO particles.

In Chapter 4, ordered mesoporous metal oxides (OMMs) are described with more reactive sites and designed to presumably have better mass transfer into the pores in comparison to impregnated carbons. DMMP chemisorption to the metal oxide reactive sites allow for greater decomposition (reported as the decomposed DMMP capacity), which is 2 to 4 times higher for the OMMs in comparison to OMC. TPD measurements for meso-Al_2O_3 and meso-Fe_2O_3 suggest that DMMP conversion to methanol is roughly one-to-one, whereas meso-TiO_2 undergoes greater decomposition with the cleavage of a second methoxy group. It was also discovered that meso-Al_2O_3 achieved the highest DMMP total volume capacity in comparison to the other materials, making it the most efficient adsorbent studied for CWA defeat.

ADSORPTION AND MECHANISTIC STUDIES OF DIMETHYL METHYLPHOSPHONATE FOR CWA DEFEAT

By

Kim Lien Huynh

Dissertation submitted to the Faculty of the Graduate School of the
University of Maryland, College Park, in partial fulfillment
of the requirements for the degree of
Doctor of Philosophy
2018

Advisory Committee:
Professor Bryan Eichhorn, Chair
Professor Liangbing Hu, Dean's Representative
Professor Zhihong Nie
Professor Efrain Rodriguez
Professor Michael Zachariah

Dedication

I would like to dedicate my dissertation to my family, especially my parents, who immigrated to America so I could have this opportunity. This is one of the many ways I intend to honor their sacrifices.

Acknowledgements

I am deeply thankful for everyone who helped make this dissertation a possibility. I would like to first acknowledge Dr. Bryan Eichhorn for his guidance, support, and patience throughout my studies. I would also like to thank my current, former, and honorary lab mates, in particular order, Dr. Junkai Hu, Scott Holdren, Miles Rehwoldt, Dr. Aaron Geller, Luning Wang, Dr. Samantha DeCarlo, Dr. Will Gibbons, Dr. Yi Wang, and Lauren Stevens, as well as my friends, Amanda Lee, Steven Wolf, Marcus Carter, Shweta Ganapati, Sitara Chauhan, Tessy Thomas, Andrea Tobochnik, Andrea Castillo, Jessica Long, Rebecca Monterusso, Rachael Riley, Tara Michael, Kyle Webb, and many others, for our discussions and your friendship. In addition, thank you to my many collaborators at the University of Maryland (Dr. Maija Kuklja, Dr. Michael Zachariah), Johns Hopkins University (Dr. Kit Bowen), Naval Research Lab (Dr. Jeffrey Owrutsky, Dr. Jeffrey Long), Lawrence Berkley National Lab (Dr. Hendrik Bluhm), and their students. This work would not have been possible without funding from the Defense Threat Reduction Agency.

Finally, I would like to acknowledge my advisory committee, Professor Michael Zachariah, Professor Efrain Rodriguez, Professor Zhihong Nie, and Professor Liangbing Hu.

And last but not least, I would like to thank my dog, Copper (someone will have to read this to him). He contributed the most man hours (metaphorically) in helping me complete my thesis with his endless love and support.

Table of Contents

List of Tables

Chapter 1:

Chapter 2:

Chapter 3:

Chapter 4:

Chapter 5:

List of Figures

Chapter 1:

Chapter 2:

Chapter 3:

Chapter 4:

Chapter 5:

Abbreviations

AC:	hydrogen cyanide
AES:	auger electron spectroscopy
APXPS:	ambient pressure X-ray photoelectron spectroscopy
ASC:	copper (A), silver (S), chromium (C) impregnated carbon
AsH_3:	arsine
ASZ:	copper (A), silver (S), zinc (Z) impregnated carbon
ASZM-TEDA:	copper (A), silver (S), zinc (Z), molybdenum (M), and triethylene diamine (TEDA) impregnated carbon
BET:	Brunauer-Emmett-Teller method
BJH:	Barrett-Joyner-Halenda method
BPL:	bituminous coal-based activated carbon
CD_3CN:	deuterated acetonitrile/acetonitrile-d_3
CG:	phosgene
CH_3I:	methyl iodide
CH_3OCH_3:	dimethyl ether
CH_3OH/MeOH:	methanol
CHCOOH:	formic acid
Chemisorption:	chemical adsorption/reaction
CHO:	formaldehyde
CK:	cyanogen chloride
CO:	carbon monoxide
CO_2:	carbon dioxide
CWA:	chemical warfare agent

DFT:	density functional theory
DMMP:	dimethyl methylphosphonate
DRIFTS:	diffuse reflectance infrared Fourier transform spectroscopy
EC:	ethylene carbonate
EDX:	energy-dispersive X-ray spectroscopy
Endo-pore:	inside the porous network
Exo-pore:	outside the porous network
GB:	Sarin, also known as (RS)-Propan-2-yl methylphosphono-fluoridate
GCMS:	grand canonical Monte Carlo simulations
^{1}H-NMR:	proton nuclear magnetic resonance
H_2S:	hydrogen sulfide
HCl:	hydrochloric acid
HCN:	hydrogen cyanide
HNO_3:	nitric acid
ΔH_{vap}:	heat of vaporization
ICP-AES:	inductively coupled plasma-atomic emission spectroscopy
Macropores:	pore diameter > 50 nm
Mesopores:	50 nm > pore diameter > 2 nm
Micropores:	pore diameter < 2 nm
MMP:	methyl methylphosphonate
MP:	methylphosphonate
NLDFT:	nonlocal density functional theory
O_{lat}:	lattice oxygen

OMC:	ordered mesoporous carbon
OMM:	ordered mesoporous metal oxide
P:	equilibrium pressure
P/P_0:	partial pressure
P_0:	saturation pressure
PAW:	projector augmented-wave
PH_3:	phosphine
Physisorption:	physical adsorption/interaction
Pluronic F127:	triblock copolymer, $EO_{106}PO_{70}EO_{106}$, where EO = ethylene oxide, PO = propylene oxide
Pluronic P123:	diblock copolymer, $EO_{20}PO_{70}EO_{20}$, where EO = ethylene oxide, PO = propylene oxide
PSD:	pore size distribution
SA:	arsine
SCCM:	standard cubic centimeters per minute
SMC:	disordered sucrose-based microporous carbon
SO_2:	sulfur dioxide
TEDA:	triethylenediamine, also known as 1,4-diazabicyclo-2,2,2-octane
TEOS:	tetraethyl orthosilicate
TGA:	thermogravimetric analysis
TPD:	temperature programmed desorption
UHV:	ultra-high vacuum
Whetlerite:	type of activated carbon
ZY:	zeolite Y-template microporous carbon

Chapter 1: Introduction and Background

Recent terrorist attacks and crime wars have increased the demand for long-lasting, highly reactive, cost efficient gas masks for protection against chemical warfare agents (CWAs). Our efforts are directed at removing a specific CWA, sarin (GB, also known as (RS)-Propan-2-yl methylphosphono-fluoridate), which is a lethal, toxic nerve agent that poses a current threat. For safety reasons, the GB simulant, dimethyl methylphosphonate (DMMP) will be used in our studies (Section 1.1).

Prior investigations of DMMP activity on model systems provide a general understanding of DMMP adsorption properties and decomposition mechanisms (Section 1.2). However, these studies relied on surface analytical techniques that require ultra-high vacuum (UHV), which does not mimic operating conditions with realistic materials. We will investigate DMMP interactions on porous materials, a typical filter support, under ambient pressure. Our studies begin with a thorough characterization of the materials' pore properties (Section 1.3), which play a significant role in our understanding of the adsorption process (Section 1.4).

Continuous research via an Edisonian approach has led to the invention of ASZM-TEDA, the current filter used in gas masks (Section 1.5). However, due to

numerous disadvantages including heavy weight, low breathability, and deactivation after surface poisoning (Section 1.6), we seek to improve ASZM-TEDA. Previous studies about ASZM-TEDA (Section 1.7) will help guide us in our investigation to develop, new superior filters to aid in the removal of CWAs (Section 1.8).

1.1 Sarin (GB) and its Simulant, Dimethyl Methylphosphonate (DMMP)

GB is a toxic nerve agent that is lethal at low concentrations. Despite being banned by the Chemical Weapons Convention in 1993,[1] GB was still used in multiple terrorist attacks (1994: Matsumoto, 1995: Tokyo)[2-4] and crime wars (1980-1988: Iran-Iraq war, 2011-present: Syrian civil war), killing thousands of soldiers and civilians. Since GB is relatively easy to synthesize and readily accessible, protection against GB will continue to be a persistent problem for years to come.[5] Therefore, we need a long-lasting, highly reactive, and cost efficient gas mask for protection against chemical warfare.

Our research objective is to study the adsorption and decomposition activity of a GB simulant to reveal crucial factors needed to rationally design new, more effective gas masks for CWA defeat. For safety reasons, DMMP is commonly studied due to its comparable functional groups, shown in Figure 1.1.[6-22] Due to similar physical and chemical properties, DMMP is used to study sorption properties and decomposition mechanisms on carbon and metal oxide

surfaces.[23-25]

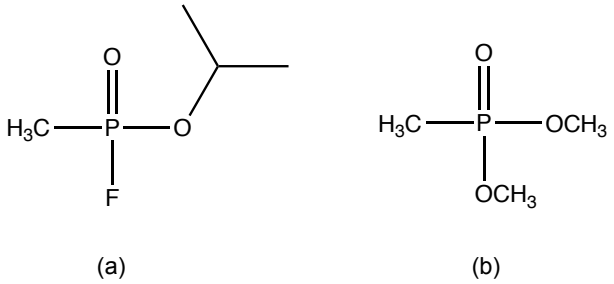

Figure 1.1. Chemical warfare agent, (a) GB and its simulant (b) DMMP.

DMMP and GB possess similar functional groups that interact with the adsorbent through the phosphoryl and/or alkoxide groups; therefore, DMMP is an excellent adsorption simulant.[26-29] However, the decomposition of DMMP compared to GB is predicted to be more difficult to ascertain.[30] Due to the absence of the highly reactive fluorine atom, it was unclear whether DMMP decomposition on any particular surface accurately mimics GB decomposition.[31, 32] However, theoretical studies have shown that GB undergoes similar decomposition pathways proposed for DMMP.[27-29]

1.2 DMMP Adsorption and Decomposition Mechanisms

Current systems remove DMMP from the airstream via two mechanisms, physical (molecular) adsorption and chemical (dissociative) reactions with dry/hydroxylated metal oxide surfaces (Scheme 1.1).[33] The chemisorption between DMMP and the adsorbent surface can occur at two sites, an uncoordinated metal site (Scheme 1a) or a surface hydroxyl site (Scheme 1b).[17, 34] The dissociative reaction with the Lewis acid metal site can result in DMMP

decomposition to form methoxy and methyl methylphosphonate (MMP) surface groups (Scheme 1c).

DMMP decomposition has been observed on many dry and hydroxylated metal oxide surfaces, such as TiO_2,[2, 24, 26, 30] MgO,[8, 16, 35-37] LaO,[16] Al_2O_3,[16, 17, 23, 25, 34, 38, 39] MnO_3,[22, 40] CuO,[31] Fe_2O_3,[14, 16] and Ni, Fe, Cu, and V oxide supported on γ-Al_2O_3, SiO_2, and TiO_2.[25] Under certain conditions, DMMP can breakdown to surface phosphate, alkoxide, and alkyl groups, while subsequently forming gaseous byproducts, such as carbon dioxide (CO_2), carbon monoxide (CO), dimethyl ether (CH_3OCH_3), formaldehyde (CHO), formic acid (CHCOOH), and more commonly, methanol (CH_3OH).[2, 14-17, 23, 24, 26, 30, 34, 37, 38]

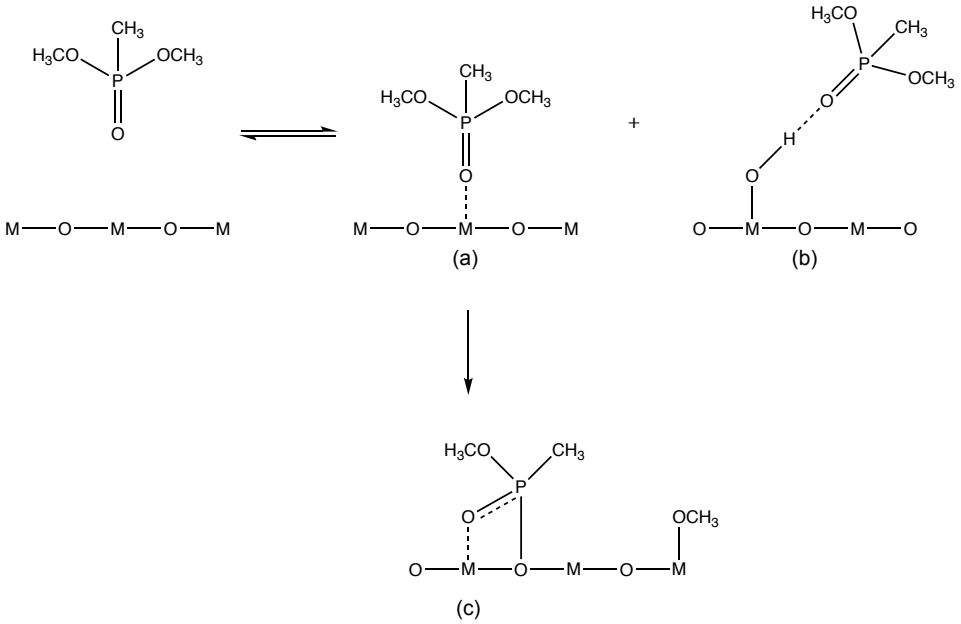

Scheme 1.1. Structures (a) and (b) are two possible molecular chemisorption modes and (c) is the dissociative chemisorption reaction, proposed by Templeton *et al.* The latter surface structure forms through the cleavage of the phosphorus-oxygen bond. Adapted from Reference 17 and 26.

Templeton *et al.* studied DMMP decomposition on Al_2O_3 using inelastic electron tunneling spectroscopy.[16, 17, 34] These investigators reported initial binding of the phosphoryl oxygen at a coordinately unsaturated aluminum atom (Lewis acid site), followed by nucleophilic substitution at phosphorus by a surface hydroxyl group (Brønsted-Lowry acid site). The methoxy group (the better leaving group) was cleaved, which leads to the formation of gaseous CH_3OH, leaving behind a bridging phosphonate byproduct by 200 °C (Scheme 1.2). By 400 °C, a surface oxygen atom performs a second nucleophilic substitution at the remaining methoxy carbon with a simultaneous protonation (from a surface hydroxyl group) to form another molecule of methanol and surface-bound methylphosphonate (MP). This decomposition behavior for DMMP was also observed on MgO and La_2O_3 surfaces.[16, 17, 34]

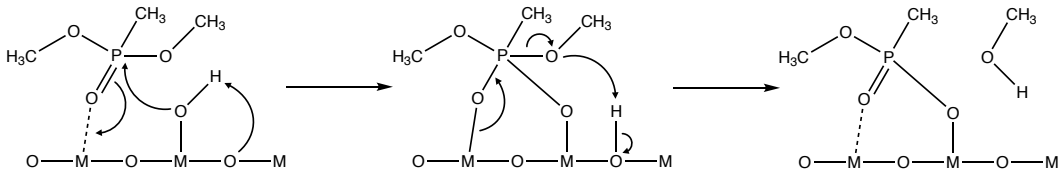

Scheme 1.2. Proposed nucleophilic attack of the Al_2O_3 surface-bound hydroxyl group on the electrophilic phosphoryl group of DMMP. Adapted from Reference 16.

Mitchell *et al.* studied DMMP adsorption on Fe_2O_3 using diffuse reflectance infrared Fourier transform spectroscopy (DRIFTS). These investigators observed DMMP decomposition on Fe_2O_3 through the formation of a different intermediate, when compared to the other metal oxides (Al_2O_3, MgO,

and La_2O_3). By 100 °C under UHV conditions, a surface hydroxyl group attacks the phosphorus atom of the phosphoryl group. Subsequent reformation of the phosphoryl group results in a gaseous CH_3OH byproduct, illustrated in Scheme 1.3.

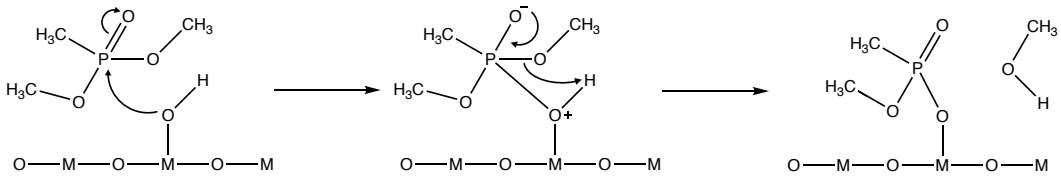

Scheme 1.3. Proposed nucleophilic attack of the Fe_2O_3 surface-bound hydroxyl group on the electrophilic phosphoryl group of DMMP. Adapted from Reference 16.

By 300 °C under UHV conditions, all carbon containing substituents are lost with no selectivity over leaving group ($-OCH_3$ or $-CH_3$) priority. Due to the multiple oxidation states of iron, the lattice oxygen (O_{lat}) from Fe_2O_3 oxidizes the $P-CH_3$ bond through the Mars-Van Krevelen mechanism.[14, 16, 41-44] In this mechanism, the surface is an active part of the reaction to form gaseous CH_3OH, which results in an oxygen vacancy on the Fe_2O_3 surface.[43]

Henderson *et al.* also observed $P-CH_3$ cleavage on $\alpha-Fe_2O_3$ using temperature programmed desorption (TPD) and auger electron spectroscopy (AES), presented in Scheme 1.4. DMMP adsorption began at 170 K and oxidation of the $P-CH_3$ bond was observed upon heating to 250 K. By 600 K, decomposition and desorption of all carbon-containing species (CH_3OH, CO_2,

CO, and HCOOH) were observed, some of which were oxidized by lattice oxygens. The phosphorous byproduct then migrated into the bulk leaving the surface available for additional adsorption and decomposition. Additional cycles showed lower DMMP decomposition (~20% of the original level), most likely a result of some phosphorus species deactivating the surface.[14]

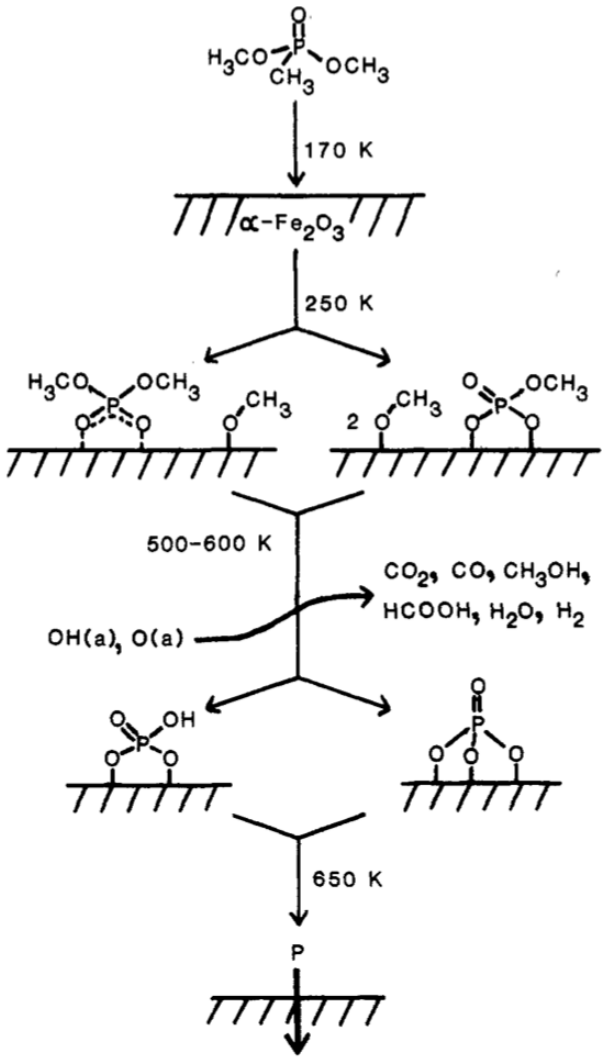

Scheme 1.4. Proposed stepwise decomposition of DMMP on Fe_2O_3 surface. Taken from Reference 14.

Trotochaud *et al.* proposed several pathways for DMMP decomposition on CuO surfaces using *in situ* ambient pressure X-ray photoelectron spectroscopy (APXPS) and DRIFTS, coupled with DFT calculations. These investigators observed DMMP cleavage at the P−CH_3, P−OCH_3, and PO−CH_3 bonds, with the incorporation of lattice oxygens in the successive formation of O_{lat}−CH_3, O_{lat}−P, and Cu−OCH_3 groups, as shown in C_4−C_7 of Figure 1.2.[31] This study revealed several pathways for room temperature DMMP decomposition on CuO, leading to the formation of surface methoxy groups.

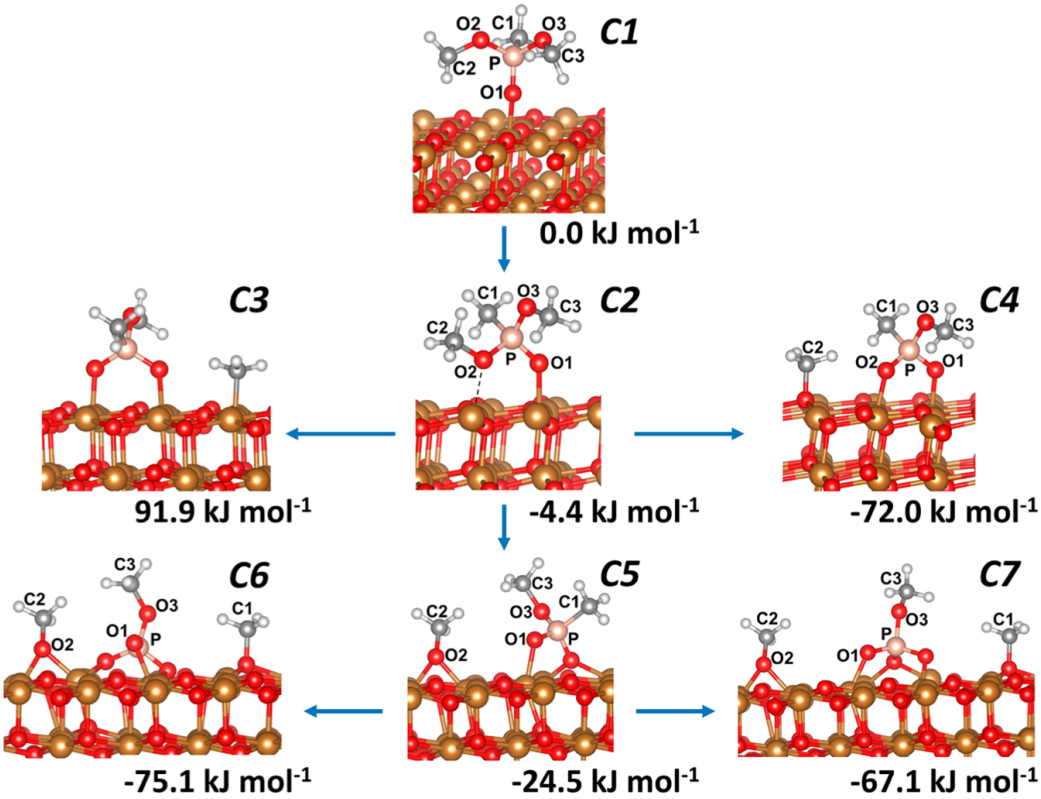

Figure 1.2. Proposed pathways for DMMP decomposition on CuO surface. Taken from Reference 31.

Many prior investigations of DMMP sorption properties on model systems have relied on surface analytical techniques that require UHV conditions, which has proven to be a long-standing problem when translating to commercial filter systems. Specifically, major drawbacks include both material and pressure gaps.[45, 46] Due to the material gap, the mechanistic details for DMMP on model systems such as, bulk single crystal, metal oxide foils, and clusters, will most likely differ from the real filter materials (metal/metal oxide impregnated porous carbons). Additionally, the pressure gap does not provide a realistic understanding of DMMP surface chemistry. Adsorption experiments performed under UHV ($p \approx 10^{-9}\, bar$) have a pressure that is nine orders of magnitude higher than ambient pressure, contributing additional surface energy to each gas molecule. Despite these disadvantages, studies performed on model systems under UHV did contribute to our fundamental understanding of DMMP sorption properties on an atomic level. However, additional studies investigating how the surface behaves under operating conditions are needed to develop a comprehensive understanding of how DMMP adsorbs and decomposes on porous adsorbents.

1.3 Porous Materials and their Characterization

Porous systems are of scientific interest due to their ability to interact with ions and molecules not only on their surface, but also throughout the bulk of the material. Porous materials, such as activated carbons, zeolites, and mesoporous metals, have been used for ion exchange, adsorption, and catalysis.[47]

Constitutionally, a porous system is comprised of a solid skeletal frame that contains voids, also known as pores.[48] Pores are historically categorized into three classes: macropores (pore diameter > 50 nm), mesopores (50 nm > pore diameter > 2 nm), and micropores (pore diameter < 2 nm); however, materials containing different sized pores, defined as multiscale porous networks, have also been demonstrated. Examples of these materials are macroporous polymers, mesoporous carbons, and microporous ceramics. The porosity of these systems is calculated by the volume of the pores divided by the total volume occupied by the solid (eq. 1.1):[49, 50]

$$P = \frac{V_{(pores)}}{V_{(tot)}} \tag{1.1}$$

where P is porosity, V(pores) is the volume of the pores, and V(tot) is the total volume.

A detailed characterization of a porous material is necessary to understand how their pore properties affect their performance as adsorbents. Pore size, volume, and surface area are determined from adsorption-desorption isotherms. These properties are measured after pre-treating the sample (by heat and vacuum) to remove all adsorbed contaminants, such as water or CO_2, while avoiding irreversible changes to the surface or solid structure. Next, adsorption measurements are taken as a gas (N_2, Ar, Kr, CO_2, or H_2) is dosed in controlled increments, with pressure allowed to reach equilibrium after each dose (Figure

1.3a).[51] As the partial pressure (P/P_0, where P = equilibrium pressure and P_0 = saturation pressure) increases, gas molecules generally adsorb in three stages. First, adsorption occurs in the smallest dimension pores and proceeds until the monolayer capacity (n_m^a), which is the amount of adsorbate required to cover the surface layer of an adsorbent, is achieved (Figure 1.3b). Continuous, sequential pore filling of the progressively larger pores results in multilayer adsorption, where multiple layers of adsorbed molecules form, which are not all in direct contact with the adsorbent surface (Figure 1.3c). Then, pressure continues to increase until the saturation pressure ($P/P_0 = 1$), when adsorption ceases because the pores are completely filled, resulting in pore condensation (Figure 1.3d).[52]

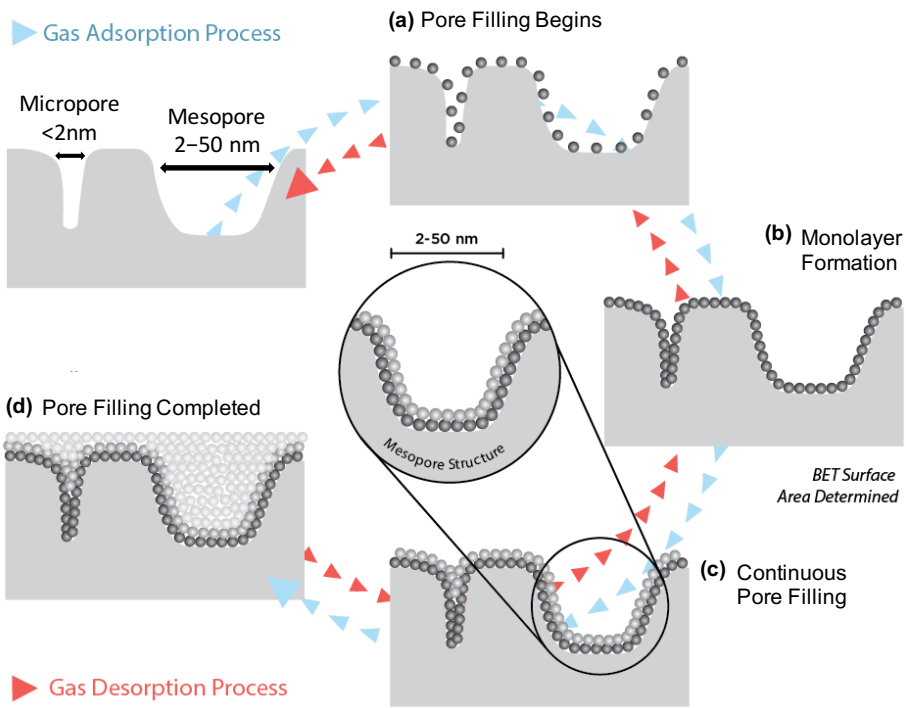

Figure 1.3. Illustration of the gas sorption process. Adapted from the Particle Technology Labs Website.

The relationship between the amount of gas adsorbed and P/P_0, at a constant temperature, is the adsorption isotherm.[49, 52] The Brunauer-Emmett-Teller (BET) method transforms the physisorption isotherm into a plot, which is applied to the BET equation (eq. 1.2):

$$\frac{\frac{p}{p^\circ}}{n\left(1-\frac{p}{p^\circ}\right)} = \frac{1}{n_m C} + \frac{C-1}{n_m C}\left(\frac{p}{p^\circ}\right) \tag{1.2}$$

where n is the amount adsorbed at a relative pressure, $\frac{p}{p^\circ}$, C is the energy of the monolayer adsorption, and n_m is the monolayer capacity. A convenient way to derive n_m, is plotting the linear relationship between $\frac{\frac{p}{p^\circ}}{n\left(1-\frac{p}{p^\circ}\right)}$ and $\frac{p}{p^\circ}$, which is used to calculate the surface area (A_s) in eq. 1.3:

$$A_s = n_m^a \cdot \mathrm{L} \cdot \sigma_m \tag{1.3}$$

where L is Avogadro constant, and σ_m is the area occupied by the adsorbate. [49]

The type of adsorption isotherm can also characterize the pore size and distribution of the material, which can largely be divided into six major classes (Figure 1.4):

- **Type I:** characteristic of microporous solids. The steep uptake at very low P/P_0 is a result of micropore filling. Materials with narrow micropores (< 1 nm) have Type I(a) isotherms, whereas materials with a broad pore size distribution (< 2.5 nm) have Type I(b) isotherms.

- **Type II:** characteristic of nonporous or macroporous adsorbents. If Point B in Figure 1.4 is steep, which occurs when the C parameter in the BET range is ≥80, the extent of adsorption corresponds to monolayer coverage. A more gradual curvature, where B cannot be identified ($C \leq 50$), indicates a mixture of monolayer and multilayer adsorption.
- **Type III:** characteristic of nonporous or macroporous adsorbents. There is no identifiable monolayer formed.
- **Type IV:** characteristic of mesoporous adsorbents. The two plateau regions represent monolayer and multilayer formation, followed by pore condensation. Materials with cylindrical pores (>4 nm) have Type IV(a) isotherms with hysteresis. Adsorbents with smaller conical and cylindrical mesopores have completely reversible Type IV(b) isotherms.
- **Type V:** characteristic of water adsorption on hydrophobic microporous and mesoporous adsorbents. Molecular clustering is followed by pore filling.
- **Type VI:** characteristic of layer-by-layer adsorption for highly uniform nonporous adsorbents. The step height represents the capacity of each adsorbed layer.

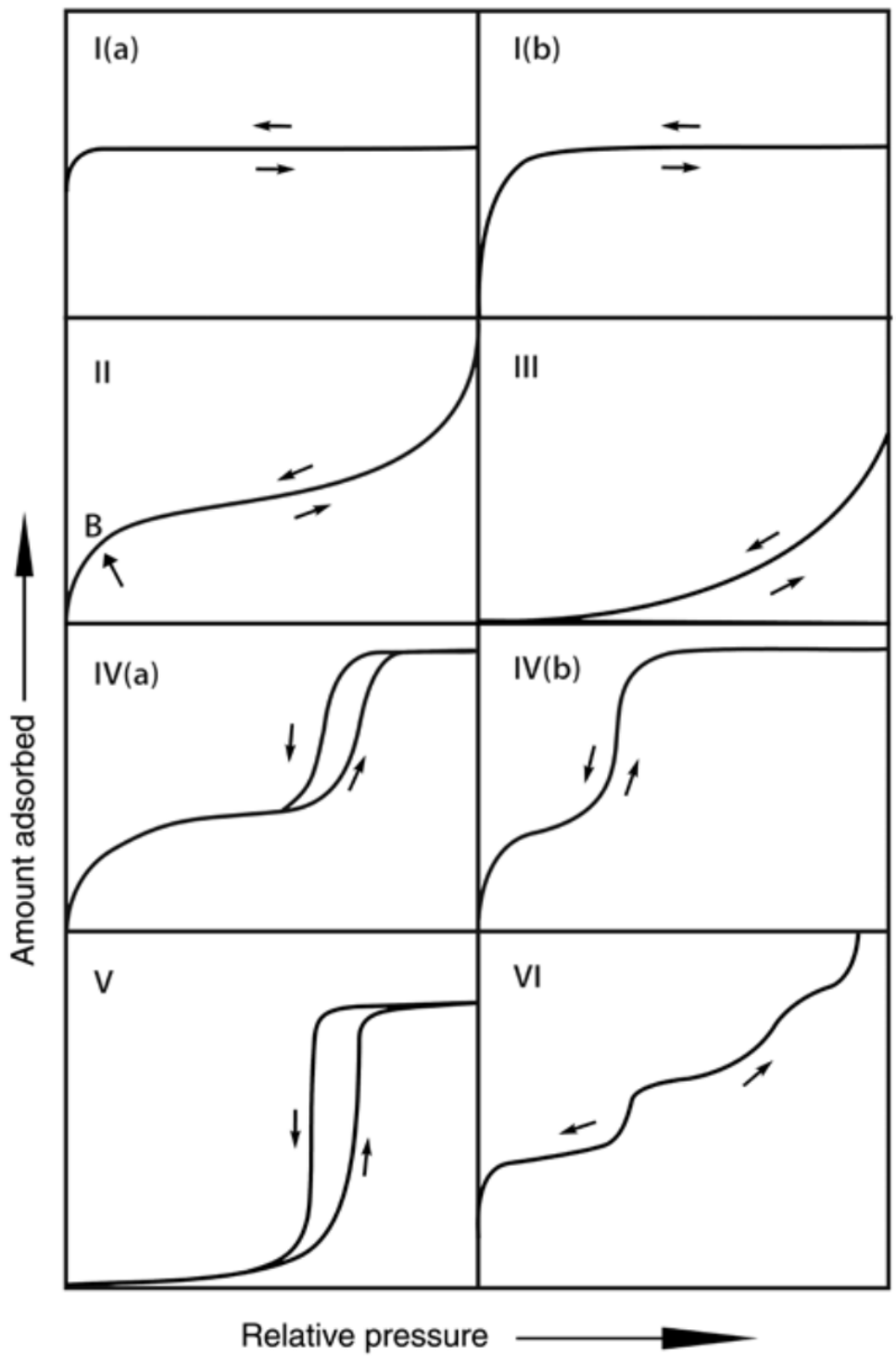

Figure 1.4. Classification of physisorption isotherms. Taken from Reference 49. Isotherm types I-VI are described in the text.

The desorption process begins after the pores are fully saturated. The gas pressure is reduced in increments to desorb the condensed gas from the system. If there is a difference in P/P_0 between the recorded adsorption and desorption isotherms (Figure 1.4 IV(a) and V), hysteresis is observed.[49] Hysteresis arises during the capillary condensation and evaporation process in the mesopores, illustrated in Figure 1.5.[53] As molecules adsorb on a surface, they add layer by layer to fill high energy sites near the pore walls followed by low energy sites farther away (Figure 1.5a-c). When gas molecules accumulate on two opposing walls and area is minimized, the ensuing convex meniscus collapses into a thermodynamically lower energy state, resulting in capillary condensation (Figure 1.5d).[52] During desorption, capillary evaporation occurs through a receding hemispherical (concave) meniscus at a pressure that is lower than the pore condensation pressure, resulting in hysteresis (Figure 1.5e). The delay observed in the vapor liquid transition is due to metastable adsorption layers and hindered nucleation of liquid bridges, which only occurs on the adsorption branch (Figure 1.5c-d).[54-57] When the pore is filled by a condensate, the liquid-vapor interface is already present, and evaporation occurs without nucleation at lower P/P_0 values (Figure 1.5e). The hysteresis ends when the adsorbed multilayer is in equilibrium with the vapor in the pore and the bulk gas phase (Figure 1.5f).

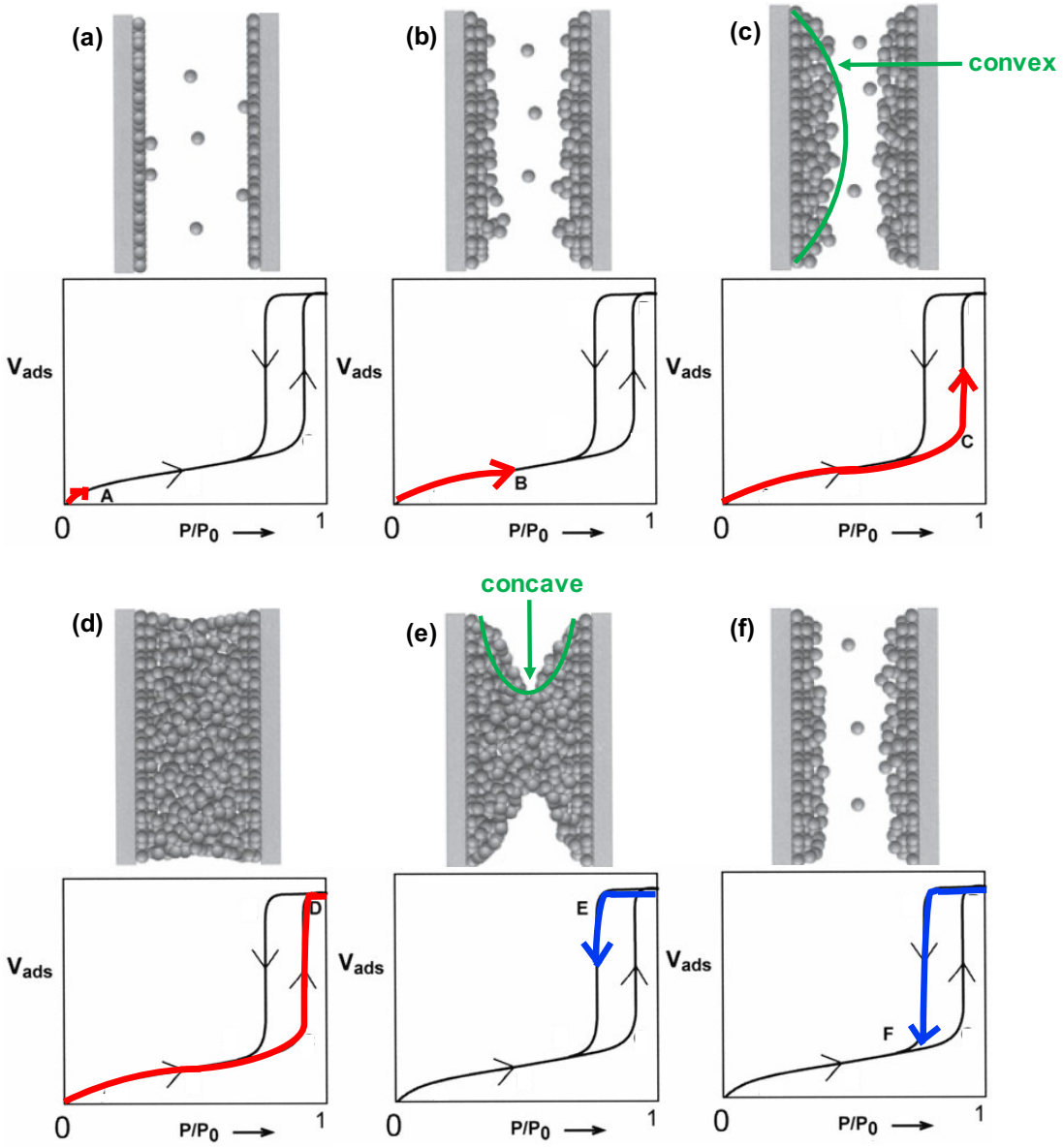

Figure 1.5. Illustration of the capillary condensation and evaporation processes in mesopores.

The type of hysteresis loop can characterize the pore size, shape, and network of the material, resulting in five main types observed in adsorption-desorption isotherms for porous materials (Figure 1.6):[49, 50, 56-63]

- **Type H1:** characteristic of uniform mesopores and non-connected cylindrical pores with narrow pore distribution. Also found in networks of ink-bottle pores.
- **Type H2:** characteristic of complex pore structures with ill-defined shapes and wide pore distribution. The very steep desorption branch in the H2(a) loops can be attributed to pore-blocking/percolation, whereas the H2(b) is associated with pore blocking for a wider neck size.
- **Type H3:** characteristic of plate-like particles giving rise to macropores, which are not completely filled with the adsorbate.
- **Type H4:** characteristic of aggregated crystal zeolites, mesoporous zeolites, and micro-mesoporous carbon.
- **Type H5:** characteristic of both open and partially blocked mesopores, such as plugged hexagonal templated silica.

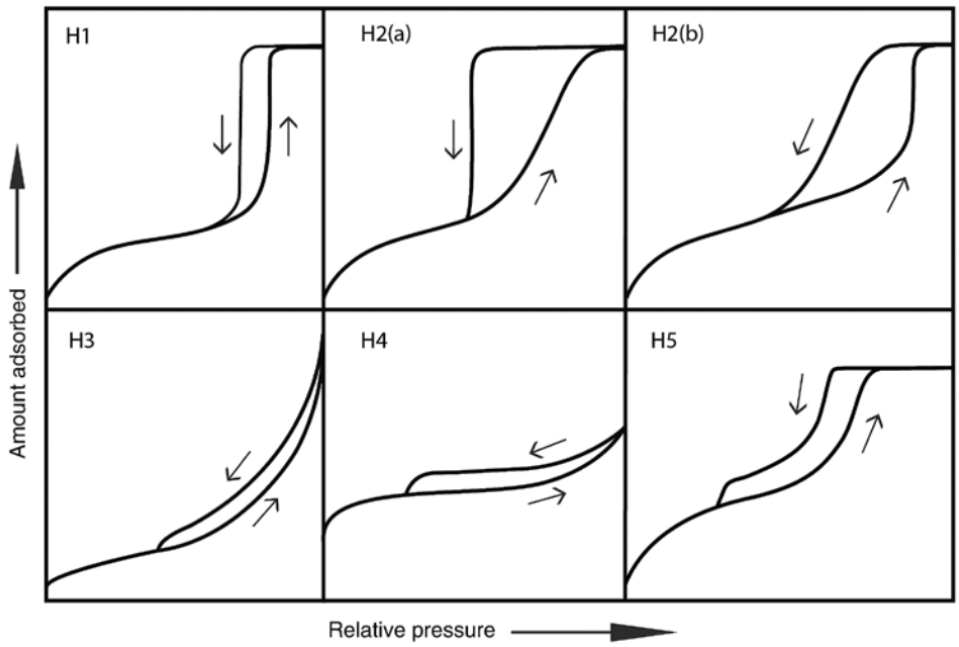

Figure 1.6. Classification of hysteresis loops. Taken from Reference 49. Hysteresis loops (H1-H5) are described in the text.

1.4 Adsorption Properties of Porous Materials

For porous materials, adsorption can occur on the external surface and within the pores. The adsorption behavior in micropores is dominated by interactions between the fluid molecules and the pore walls. The continuous adsorption process results in micropore filling, followed by multilayer adsorption on the small external area.[49, 50, 57] Multilayer adsorption in mesopores depends on fluid-wall attraction and attractive interactions between the fluid molecules of the multilayers. The stability of the adsorbed multilayers is determined by long-range van der Waals interactions, surface tension, and curvature of the liquid-vapor interface.[50, 62]

Adsorption can be characterized as a physical interaction (physisorption) or a chemical reaction (chemisorption).[49] Physisorption has been observed through weak intermolecular forces (*e.g.* van der Waals forces and long-range London dispersion forces)[50] between the adsorbate and the adsorbent. Chemisorption involves the formation of covalent (or polar covalent) bonds, which can result in additional chemical reactions (discussed previously in Section 1.1).

1.5 Historical Attempts at Respirator Development

"There is only one thing, and one thing only, that can save us our present and future health, the health of our descendants, and in many cases, our own lives… Never be without your Soldier's Friend. The Soldier's Friend is his Small Box Respirator."

- Taken from an unsigned document during World War I

Protection against CWAs have been a persistent problem for military personnel since World War I, where chlorine gas (the first CWA used in warfare), killed over 6000 soldiers during the Battle of Gravenstafel Ridge on April 22, 1915.[1, 64] Consequently, the demand for protection gave rise to the development of cost-effective and readily available respirators. Early designs consisted of a cotton pad/cloth soaked in a solution of sodium carbonate, sodium thiosulfate, and water.[5] Unfortunately, these respirators only worked for a few minutes against a normal concentration of chlorine, which would later be improved and serve as inspiration for early gas mask designs.[65]

The first gas mask contained two features, namely a tight seal around the face, and a snout covering the nose and mouth that directed breathing from a singular hole in the face piece, which protected the user from toxic gases.[5] The air flowing through the hole needs to be supplied or filtered. Since it is difficult to supply clean air on the field, the military utilized filters to clean the air before the user inhaled it.[65]

The first gas mask filter was a combination of charcoal carbon and soda lime.[5, 64] Carbon based filters were commonly used because of its sizable network of channels and pores, which can adsorb large quantities of organic gases.[66-70] The different types of charcoal carbons and their protection time against a variety of gases are listed in Table 1.1. Soda lime (hydrated lime, cement, kieselguhr, sodium hydroxide, and water) was added as an additional defense against inorganic contaminants.[64, 65] The combination of charcoal carbon and soda lime was used in a small box respirator, which performed better than each individual component. The mixture decreased the negative effects of high temperature and humidity on the charcoal adsorption capacity, while increasing the soda lime reactivity.[5] However, fine particulates found in toxic smoke/fumes still required additional layers of protection. Consequently, felt was incorporated to remove the fumes, but this was found to increase breathing resistance. To combat this, later efforts included carbon-impregnated/asbestos-impregnated filter paper; however later work demonstrated that prolonged inhalation of asbestos fibers led to fatal

illnesses, such as lung cancer, mesothelioma, and asbestosis, leading to its eventual ban in the 1970s.[65]

Table 1.1. Typical Absorptive Values of Different Charcoals Against Various Gases. Taken from Reference 64.

No.	Charcoal	Nation	H_2O Content, %	Accel. Chloropicrin, Service Time, Min.	Service Time, Minutes Standard Conditions						
					Chloropicrin	Phosgene	Hydrocyanic Acid	Arsine	Cyanogen Chloride	Trichloromethyl-chloroformate	Chlorine
1	Poor cocoanut	U.S.A	0	10	120	175	20	18	55	50	270
2	Medium cocoanut	U.S.A	0	30	350	260	25	25	65	65	370
3	Good cocoanut	U.S.A	0	60	620	310	27	30	75	70	420
4	Wet No. 2	U.S.A	12	18	320	330	35	16	35	95	
5	Impregnated No. 2	U.S.A	0	35	400	700	70	400	70	190	510
6	Wood	French	0	2.5	25	75	9	0	1	20	
7	Wood	British	0	6	70	90	18	4	5	30	
8	Peach stone	British	0	16	190	135	30	25	65	60	
9	Treated wood	German	0	42	230	105	20	20	22	25	
10	Impregnated No. 9	German	30	9	90	320	16	1	110	120	

Standard Conditions of Tests

Mesh of absorbent……..... 8-14
Depth of absorbent layer ……... 10 cm.
Rate of flow per sq. cm. per min……..…. 500 cc.
Concentration of toxic gas …….…… 0.1 percent
Relative humidity ……...……. 50 percent
Temperature ……..…….. 20 °C
Results expressed in minutes to the 99 percent efficiency points.
Results corrected to uniform concentrations and size of particles.

By the end of World War I, J.C. Whetzel and E. W. Fuller invented whetlerite, an activated carbon impregnated with copper, which was investigated as a suitable asbestos alternative. In this system, a process of heat and steam was

used to "activate" the charcoal carbon[5] by eliminating volatile compounds blocking the pores, increasing porosity, and the number of active sites (Figure 1.7).[24, 64, 65] The copper impregnated activated carbon provided twice the protection of regular charcoal against phosgene (CG), triple the protection against hydrogen cyanide (AC), and ten times the protection against arsine (SA).[68, 71-75] By World War II, whetlerite was used in the standard filter material known as whetlerite AS (80% whetlerite and 20% soda-lime). By 1943, whetlerite AS was further improved through the replacement of soda lime with other impregnants to make whetlerite ASC (copper (A), silver (S), and hexavalent chromium (C)), which provided greater protection against SA, AC, and cyanogen chloride (CK).[66, 68, 76-78]

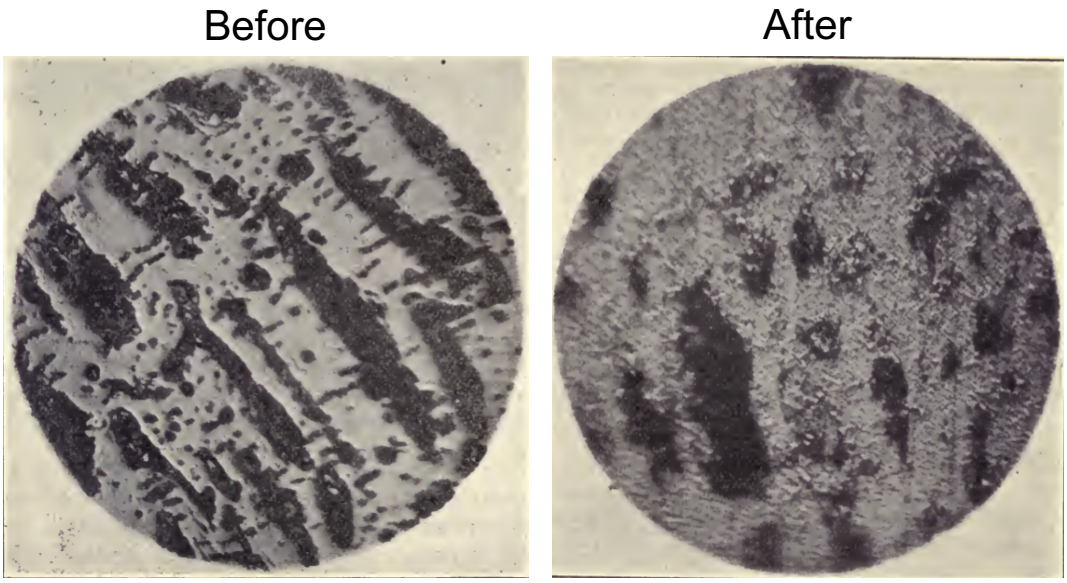

Figure 1.7. Photomicrographs of carbonized charcoal before and after 31 minutes of steam activation. "Magnified 732 Diameters." Taken from Reference 64.

ASC filters were widely used until the 1980s, when they were discontinued due to the cancer-producing effects of the Cr(VI) species, which also made disposal of used carbon fibers difficult and expensive.[71, 77, 79-83] Consequently, chromium was replaced with a combination of zinc, molybdenum, and triethylenediamine (TEDA, also known as 1,4-diazabicyclo-2,2,2-octane),[66, 77, 84] in the development of an upgraded filter.

Calgon Carbon designed ASZM-TEDA (copper (A), silver metal (S), zinc (Z), molybdenum (M), and TEDA) to be a chromium-free replacement of whetlerite ASC. ASZM-TEDA is still widely used in gas mask canisters to remove toxic gases and/or vapors in military, industrial, and other applications (Figure 1.8). However, due to the sensitive nature of the material, there is very little published in academia. While the literature lists concentrations of ASZM-TEDA impregnants, it lacks vital "sensitive" data, such as the properties of the impregnants (oxidation state, size, location, etc.), which is necessary to have a comprehensive understanding of the surface chemistry. While government labs may have access to this sensitive information, their research primarily focuses on performance. Most of the published data on ASZM-TEDA is disclosed in patents and government documents, which discuss design and performance, such as bed height vs. pressure drop, layering and particle size, axial vs. radial flow, gas life challenge/breakthrough, and filter lifetimes.[85-90]

Figure 1.8. Modern-day gas mask with an ASZM-TEDA canister.

1.6 ASZM-TEDA Design and Considerations

The logic behind the design and performance of gas mask filters is important to recognize before considering a replacement. The current military mask composition, ASZM-TEDA, is a compromise, embodying an optimum balance among many requirements listed in Table 1.2.[5] One of the requirements is maximum protection, which is directly related to the amount of material used, and the capacity of the mechanical filter. However, the more material used, the larger and heavier the canister, which impairs the user's vision and not practical for field use.

Higher packing density and deeper bed height can be applied to increase filter protection time. However, this would also increase the pressure drop (breathing resistance). Although this pressure drop can be lowered by increasing the diameter of the bed, this will also increase the size of the canister, restricting the movement and vision for the user.

By 1997, Newton *et al.* designed a frustum layered canister, utilizing different sized ASZM-TEDA granules in a carbon bed. This new design demonstrated a lower pressure drop in comparison to the cylinder canister, and increased performance for CK removal (Figure 1.9).[85] A bed consisting of a 0.4 cm layer of 12x30 mesh carbon followed by a 0.6 cm layer of 30x40 mesh carbon offered a 25% increase in CK protection time and a 14% reduction in airflow resistance, when compared to a 1.0 cm bed depth of 30x40 mesh carbon.[87] The higher protection time was achieved by a greater mass transfer rate, which is the movement of adsorbate (toxic molecule) into the adsorbent. Separation of ASZM-TEDA particles by mesh size decreased the packing density and in turn, increased the mass transfer rate.

Table 1.2. Gas Mask Requirements and ASZM-TEDA Design

Gas Mask Requirements	ASZM-TEDA	Ref.
High-level filtration/protection against a broad spectrum of CWAs	Removes cyanogen chloride (CK), methyl iodide (CH_3I), hydrogen sulfide (H_2S), sulfur dioxide (SO_2), hydrogen cyanide (HCN), chlorine (Cl_2), arsine (AsH_3), phosphine (PH_3), organophosphonate esters, and acid-gas producers	23, 71, 73, 76, 81, 84, 91
Low breathing resistance	Changed canister shape (cylinder to frustrum), decreased packing density, layered different size granules in the carbon bed for a lower pressure drop	85
Does not interfere with vision, small, light-weight, comfortable	Delicate balance of chemicals for the best protection in a reasonable canister size	5
Able to withstand field conditions with a service life for several months, and long shelf-life (several years)	Degrades from prolonged exposure to humid air, even worse with low levels of airborne contaminants, such as, SO_x, NO_x, and fuel vapors, which block active sites	92
Easy to manufacture and cost-effective	Made in Kg quantities, $9/pound	93

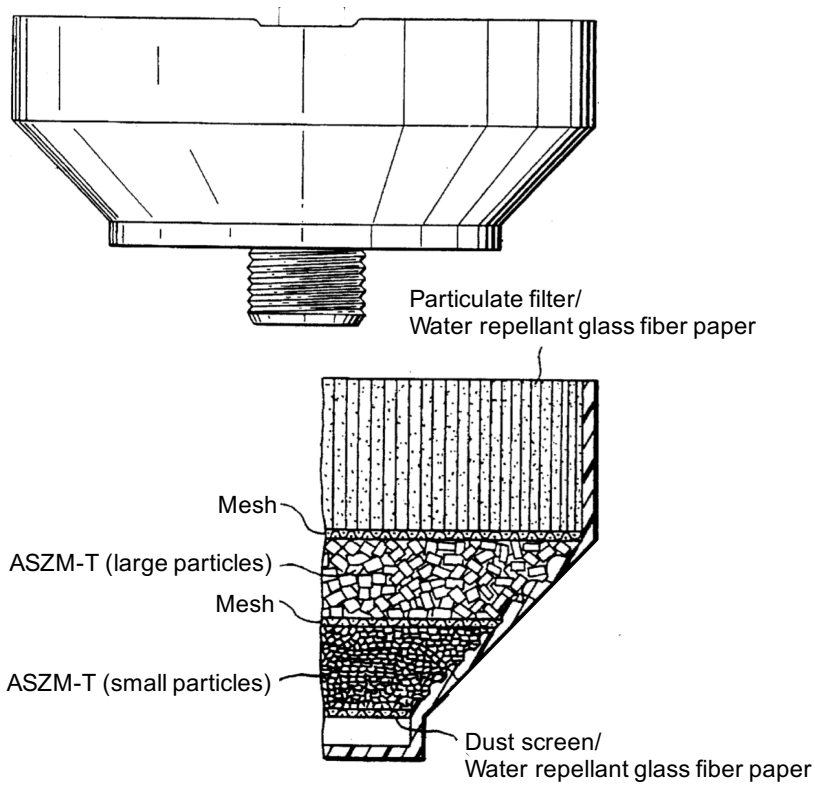

Figure 1.9. Schematic of a frustum layered canister with different sized ASZM-TEDA granules in a carbon bed. Adapted from Reference 85.

When freshly prepared, ASZM-TEDA has a high capacity for the removal of CWAs and selected TICs. However, ASZM-TEDA degrades from prolonged exposure to humid air, and is further hastened when exposed to humid air containing low levels of airborne contaminants, such as, SO_x, NO_x, and fuel vapors. Degradation of ASZM-TEDA results in a decreased protection capability of the filter and costly filter change-outs.[91] Although much work was performed to develop the current filters via an Edisonian approach, a more fundamental approach towards understanding the mechanisms of CWA removal is needed for a rational development of new, more superior filters.

1.7 ASZM-TEDA Literature Background

ASZM-TEDA is a microporous, activated carbon with high surface area (785−850 m^2 g^{-1})[89] and a pore volume of 0.386 cm^3 g^{-1}.[92] ASZM-TEDA contains 4−6 wt% copper (A), 0.03−0.1 wt% silver metal (S), 4−6 wt% zinc (Z), 1−3 wt% molybdenum (M), presumably as oxides, and 2−4 wt% TEDA,[33, 78, 86, 89, 92, 93] to protect against a broad spectrum of toxic gases. These carefully selected metals/metal oxides were impregnated into/onto the carbon support to remove CWAs without forming toxic byproducts or suffering from side reactions with the other components.[76, 94] However, it is still unclear what specific processes are involved and the cooperative effects of the impregnants in the removal of the toxic gases and/or vapors.

The carbon support used in ASZM-TEDA is BPL, a well-studied bituminous coal based, activated carbon, with a high surface area >1000 m^2 g^{-1}. BPL is predominantly microporous and well known for its capacity to remove toxic gases from the airstream and contaminants from water.[69, 95, 96] Many research groups have studied the adsorption of chemical warfare agents/toxic industrial chemicals (sarin, NH_3, SO_2, HCN, Cl_2, C_6H_6, CH_2Cl_2, and/or ethylene oxide),[97-109] air pollutants/small molecules (H_2S, COS, N_2, CH_4, CO, CO_2, and/or H_2O),[110-130] and organic compounds (*n*-alkane, aromatics, alcohols, and/or haloginated hydrocarbons)[101, 102, 131-170] with BPL carbon. The mesopores provide good transport properties within the granule, while the micropores have relatively

strong potential wells in which gases can be adsorbed, making it a sufficient adsorbent for filtration purposes.

Due to the significance of the porous properties of BPL, different gas equilibrium models (N_2, Ar, Kr, CO_2, or H_2) have been used to determine the pore size distribution (PSD). Traditionally, PSD analysis of porous materials are evaluated with N_2 at 77 K because it is simple and inert.[171] However, for predominantly microporous systems like BPL, temperature diffusion of N_2 molecules into the micropores <0.7 nm is very slow, which can influence the adsorption measurements. Therefore, to mitigate these problems, multiple research groups employed different gas adsorbents (CO_2 or H_2) or methods such as, nonlocal density functional theory (NLDFT) and grand canonical Monte Carlo simulations (GCMS), to determine the PSD of BPL. These studies showed pore sizes to be 0.59 – 2.5 nm.[51, 57, 171, 172]

Although BPL is a high ash-loading material (maximum 8 wt%), containing mineral matters primarily of Si (~32%), Al (~26%), S (~24%), Fe (~9%), Ca (~2.9%), Ti (~2.2%), and K (~1.8%),[93] additional impregnants (CuO_x, Ag, ZnO, MoO_x) were added to increase the binding/chemisorption of toxic gases.[70, 76, 94] The success of ASZM-TEDA is a result of the intentional physical distribution and chemical interplay of the multiple metals/metal oxides that are incorporated into/onto BPL. Rossin *et al.* reported a cooperative mechanism between Cu and Zn impregnants for the removal of hydrogen cyanide by forming

$Zn(CN)_2$, as opposed to cyanogen byproducts that are generated with Cu only.[81] Similarly, Nickolov *et al.* described the use of Ag to remove arsine and phosphine by catalytic oxididation,[71] and Smentkowski *et al.* reported the heterogeneous catalytic oxidation of organophosphonate esters on Mo without forming the undesired accumulation of carbonaceous or phosphorus species on the Mo surface.[23]

ASZM-TEDA impregnants can remove a variety of CWAs such as, cyanogen chloride (CK), methyl iodide (CH_3I), hydrogen sulfide (H_2S), sulfur dioxide (SO_2), hydrogen cyanide (HCN), chlorine (Cl_2), arsine (AsH_3), phosphine (PH_3), organophosphonate esters, and acid-gas producers. [23, 71, 73, 76, 81, 84, 173] A summary of the function of each ASZM-TEDA impregnant is listed in Table 1.3. While the high surface area and reactive impregnants of ASZM-TEDA provide initial protection against toxic gases, the adsorption capacity of this filter degrades over time. As toxic gases and/or water condensation adsorb into the pores and onto the surface, the pore properties change. Active sites are poisoned, ultimately leading to the failure of these filters.

Table 1.3. ASZM-TEDA Impregnants and their Function

Impregnant	Function	Reference
CuO_x	Removal of HCN, CK, Cl_2, AsH_3, PH_3, HCl, HF, H_2S, and acid-gas producers such as phosgene	71, 81, 84, 173
Ag	Catalytic oxidation of AsH_3, PH_3	71, 84
ZnO	Removal of HCN, CK, NH_3	71, 81, 173[71, 81, 173]
MoO_x	Catalytic oxidation of organophosphonate esters	23
TEDA	Removal of CK, CH_3Br, CH_3I, HCN, H_2S, and SO_2	73, 76, 173

1.8 Motivation

ASZM-TEDA characterization in the public literature lists metal concentrations, but the nature of the impregnants (oxidation state, size, location, etc.) is unknown. A full understanding of the impregnants and their role in CWA removal can guide us in the strategic development of superior filtration materials. Beginning with a full analytical characterization of ASZM-TEDA, we can identify crucial information to aide us in the synthesis of deconstructed analogs of ASZM-TEDA. Studying these single variable models can identify the functions and limitations of each component (Chapter 2 and 3), so we can tailor our synthesis for new materials (Chapter 4), with catalytic performance, selective adsorption, and higher capacities for CWA defeat (Chapter 5).

Chapter 2: Dimethyl Methylphosphonate Adsorption Behavior and Desorption Energies on Ordered Mesoporous Carbons

The work presented in this chapter was adapted from Huynh, K.; Holdren, S.; Hu, J.; Wang, L.; Zachariah, M. R.; Eichhorn, B. W., Dimethyl Methylphosphonate Adsorption Capacities and Desorption Energies on Ordered Mesoporous Carbons. *ACS Appl. Mater. Interfaces*, **2017**, *9,* 40638-40644.

2.1 INTRODUCTION

ASZM-TEDA is used in nearly all United States nuclear, biological, and chemical filters for the removal of chemical warfare agent (CWA) vapors. The effectiveness of these filters largely depends on the limited space available for physical adsorption in the pores and the amount of reactive metal oxides contained in/on the carbon.[33] While it is accepted that the adsorbent pore properties directly influence filter performance,[174] the significance of the pore parameters (*i.e.* the size, volume, and surface area) remains unknown.

The current carbon support used in ASZM-TEDA is BPL, a bituminous coal based, steam activated, granular carbon, with a high surface area >1000 $m^2 g^{-1}$. While this material is largely microporous, there are significant variations among the pore diameter distributions. Russel *et al.* used five different gas equilibrium models to determine the pore width to be between 0.59−1.8 nm.[172] In

addition, BPL is a high ash-loading material (maximum 8 wt%), containing mineral matters primarily of Si (~32%), Al (~26%), S (~24%), Fe (~9%), Ca (~2.9%), Ti (~2.2%), and K (~1.8%).[93] While BPL has been established as an effective adsorbent for CWAs, very little information is available for the dynamic effects occurring at the molecular level. Further investigations are needed to understand the mechanistic details of where and how CWAs adsorb and desorb from the carbon adsorbent materials.

When evaluating the effectiveness of gas mask filters, studies are performed to test their ability to remove CWA vapors, determine their adsorption capacities, and filter lifetimes. For safety reasons, the CWA simulant, DMMP is commonly used to investigate the sorption properties of G-series nerve agents, such as Sarin (GB) and Soman (GD), which possesses similar functional groups as illustrated in Figure 2.1.[175] DMMP is used primarily as an adsorption simulant because it lacks the highly reactive P−F group common to all G-agents, which is a highly reactive functionality.[69] Many theoretical and experimental studies show that DMMP adsorption occurs through the phosphoryl group or O−P−O moieties, onto carbon nanotubes, active carbons, and metal oxides.[23, 92, 176, 15]

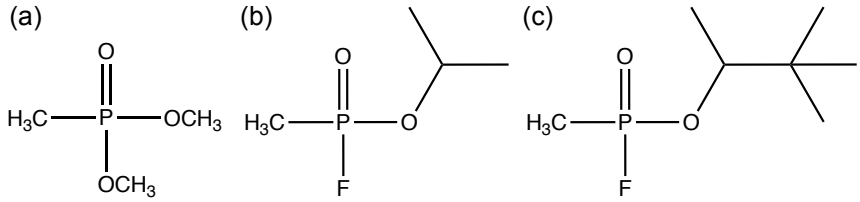

Figure 2.1. (a) Dimethyl methylphosphonate (DMMP), (b) Sarin (GB), and (c) Soman (GD).

Harris *et al*. monitored DMMP adsorption to BPL and ASZM using ^{31}P magic angle spinning NMR. DMMP adsorbs into adsorbent micropores at low loadings, then ultimately forming multilayers of weakly bound DMMP molecules on the surface.[92] However, desorption energies and pore structure effects were not investigated.

Desorption energies of organic compounds from various carbon substrates have been investigated with TPD experiments using techniques such as thermogravimetric analysis (TGA) and mass spectrometry.[177-181] For example, Li. *et al.* performed numerous studies of naphthalene, acenaphthene, and phenanthrene desorption from various carbon supports and mesoporous silicas.[177, 179, 180] However, to the best of our knowledge, the determination of DMMP desorption energies from various carbon supports have not been thoroughly investigated.

In this study, we compared the micropore (pore diameter <2 nm) and mesopore (2< pore diameter <50 nm) structural effects by investigating DMMP adsorption in three different ordered mesoporous carbons (OMCs), a zeolite-templated ordered microporous carbon (ZY), a disordered microporous carbon (SMC), and the microporous ASZM support, BPL. DMMP adsorption was evaluated using quantitative ^{1}H-NMR to measure monolayer/low surface coverage (1 h exposure), multilayer coverage (5 and 70 h exposure), and liquefaction/total pore filling (800 h exposure) for BPL and the OMCs. TGA was

employed to determine desorption energies of DMMP pre-saturated on all the carbon materials. These studies show that the surface area and pore volume dictate total adsorption loading with differences in the desorption energies as a direct result of the carbon pore networks.

2.2 EXPERIMENTAL SECTION

2.2.1 Materials

AR grade dimethyl methylphosphonate (≥97.0%) (DMMP) was purchased from Sigma Aldrich (USA) and used without further purification. Sucrose and Zeolite Y were purchased from Fischer Chemical and Alfa Aesar, respectively. The commercial activated carbon, BPL (12x30 mesh), was supplied by the U.S. Army Edgewood Chemical and Biological Center.

2.2.2 Microporous Carbons

The microporous carbons, sucrose based microporous carbon (SMC) and zeolite Y-template microporous carbon (ZY), were prepared by Mr. Luning Wang using slight modifications of methods as described elsewhere. [182, 183]

2.2.2.1 Synthesis of a Sucrose Based Microporous Carbon (SMC)

The microporous carbon was synthesized using sucrose as the carbon source described in Reference 182. In a typical reaction, 20 g sucrose was dissolved in 6 M sulfuric acid to form 5% sucrose solution, which was refluxed in

a 1 L round bottom flask at 120 °C overnight. The resulting black suspension was filtered and washed with distilled water several times. The product was dried at 100 °C in an oven for 24 h, and underwent carbonization at 1000 °C for 3 h with a heating rate of 5 °C min^{-1} under argon/5% H_2 atmosphere.

2.2.2.2 Synthesis of a Zeolite Y-template Microporous Carbon (ZY)

The synthesis of this microporous carbon using zeolite Y as a template was described in Reference 183. In a typical synthesis, 1 g zeolite Y (Hydrogen, 80:1 molar ratio of SiO_2:Al_2O_3) was exchanged with ~ 50 ml 1 M NH_4Cl for three days. The ammonium ions were decomposed at 500 °C for 1 h in air to produce Brønsted-Lowry acid sites in the zeolite. The obtained zeolite Y powder was heated at ~150 °C under vacuum for 5 h in a round bottle flask on a Schlenk line to fully activate the pores. Then the zeolite Y was transferred into a drybox and 0.26 g phenol was added. Afterwards, the mixture was incubated at 65 °C under reduced pressure overnight. Excess paraformaldehyde, ~0.4 g was heated to 120 °C to liberate monomeric formaldehyde, which was transferred as a gas to the phenol/zeolite composite to react at room temperature. The white zeolite/phenol composite turned into a pink/red color, which confirmed the polymerization process. The product was calcined in N_2 for 5 h at 125 °C (ramp rate 1 °C min^{-1}) to cross-link the polymer, followed by a further pyrolysis process at 900 °C for 14 h (ramp rate 5 °C min^{-1}). After the carbonization process, the dark sample was added to excess concentrated hydrofluoric acid (50%) and stirred overnight. Then

the sample was filtered and washed by deionized water thoroughly and dried at 105 °C under vacuum overnight.

2.2.3 Ordered Mesoporous Carbons (OMCs)

The OMCs, FDU-15, CMK-3, and CMK-8, were prepared by Dr. Junkai Hu using slight modifications of methods as described elsewhere. [184-186] A general schematic of these synthetic processes are described in Figure 2.2.

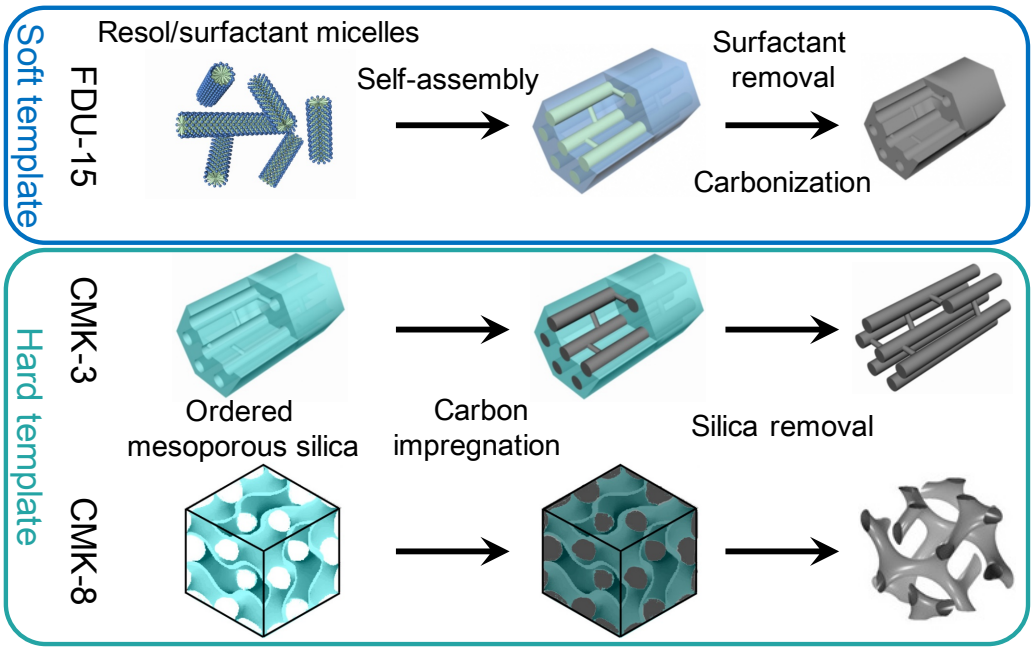

Figure 2.2. Schematic of the synthetic processes for the OMCs.

2.2.3.1 Synthesis of 1D Cylindrical Ordered Mesoporous Carbon FDU-15

FDU-15 was synthesized by a soft template method described in Reference 184. Briefly, a resol precursor was prepared from a low-molecular-weight polymer derived from phenol and formaldehyde using a polymerization

method. A triblock copolymer Pluronic F127 ($EO_{106}PO_{70}EO_{106}$, where EO = ethylene oxide, PO = propylene oxide) was used as a structure directing reagent, while urea and formaldehyde were used as the carbon source. In a typical reaction, 1 g F127 was dissolved in 8.0 g ethanol. Then 5 g of the 20% resol precursor was added to the solution and the mixture was stirred for 1 h. The mixture was transferred to a petri dish for 5−8 h at room temperature and then 24 h at 100 °C to evaporate ethanol. Then the gel was thermopolymerized for 12 h in an oven at 180 °C. The product was then ground to a fine powder, calcined under Ar for 3 h at 600 °C, and another 2 h at 900 °C. The heating rates were 1 °C min^{-1} to 600 °C and 5 °C min^{-1} to 900 °C.

2.2.3.2 Synthesis of 3D Hexagonal Ordered Mesoporous Carbon CMK-3

CMK-3 was synthesized by a hard template method described in Reference 185. In a typical reaction, 1.2 g SBA-15 was added to a solution of 1.5 g sucrose, 0.17 g sulfuric acid, and 6 g H_2O. The mixture was dried for 6 h in an oven at 100 °C, followed by another 6 h at 160 °C. The silica sample was treated again with a mixture of 0.96 g sucrose, 0.11 g sulfuric acid, and 6 g H_2O, followed by the same drying process for 6 h in an oven at 100 °C, then another 6 h at 160 °C. The sample was then carbonized at 600 °C in flowing Ar for 3 h in a tube furnace, followed by another 2 h in flowing Ar at 900 °C. The heating rates were 1 °C min^{-1} to 600 °C and 5 °C min^{-1} to 900 °C. The silica was removed by dissolution with 3M NaOH solution at 50 °C. The carbon was collected by

centrifugation and washed with deionized water. The extraction/washing process was done in repetition three times. Two batches of CMK-3 were synthesized for our investigation. They will be referred to as CMK-3 and CMK-3*, due to their slight differences in pore properties, which are described in Table 2.1.

2.2.3.3 Synthesis of 3D Bicontinuous Ordered Mesoporous Carbon CMK-8

CMK-8 was synthesized by a hard template method described in Reference 186. KIT-6 was used as a template, with the molar ratio of 0.017 P123/1.67 tetraethyl orthosilicate (TEOS)/1.67 n-butanol/1.83 hydrochloric acid (HCl)/195 H_2O, while sucrose was used as the carbon source. The carbon nanocasting process was similar to CMK-3, with adjustments to the sucrose and sulfuric acid amounts to match the pore volume of KIT-6. In a typical reaction, 1.2 g KIT-6 was added to a solution of 1.17 g sucrose, 0.13 g sulfuric acid, and 4.7 g H_2O. The mixture was dried for 6 h in an oven at 100 °C, then another 6 h at 160 °C. The sample was treated again with a mixture of 0.62 g sucrose, 0.07 g sulfuric acid, and 3.85 g H_2O, followed by the same drying process for 6 h in an oven at 100 °C, then another 6 h at 160 °C. Annealing and silica removal were as described for CMK-3.

2.2.4 Characterization of Carbon Materials

Pore size, volume, and surface area were determined from nitrogen (N_2) adsorption-desorption isotherms recorded with a Micromeritics ASAP 2020

Porosimeter Test Station. Samples were degassed in vacuum at 100 °C for 12 h prior to characterization. The specific surface areas were calculated using the Brunauer-Emmett-Teller (BET) method from the N_2 adsorption data in the relative pressure range (P/P_0) of 0.05−0.20. The general porosity distribution was calculated from the adsorption branch using the Barrett-Joyner-Halenda (BJH) equation. The micropore size distribution was calculated from the adsorption branch based on nonlocal density functional theory (NLDFT),[151, 187, 188] with a relative pressure beginning at 0.001.

Samples were imaged with a JEM 2100 Field Emission transmission electron microscope operating at 200 kV. The carbons were dispersed in methanol and a 10 μL aliquot of the resulting dispersion was drop cast on the TEM grids. The TEM grids used were carbon-coated Cu grids (CF200-Cu, Electron Microscopy Sciences).

2.2.5 Exposure of Carbon Samples to DMMP

2.2.5.1 Sample Preparation for ^{1}H-NMR Study

Carbons were pre-treated at 100 °C for ≥6 h under static vacuum to remove any adsorbed contaminants before exposure to DMMP using the vial-in-vial method, modified from the literature.[189] Approximately 25 mg of carbon was transferred to small glass vials. Each small glass vial was placed inside a larger vial that contained a sufficient amount of liquid DMMP (200 μL) to saturate the head space of the vial assembly. The larger vial was then capped, and stored in a

desiccator. Typically, room temperature vapor pressure of DMMP (~1.0 Torr) is enough to accomplish adsorption of the vapor into/onto the carbon samples,[16] however, due to detection limits with ^{1}H-NMR for the 1 h exposure tests, the carbon and small glass vials were taken directly from the oven and placed inside larger vials with liquid DMMP, then capped, before stored in a desiccator. For all samples, the exposure process was conducted under atmospheric pressure at room temperature (24−26 °C). The samples were then removed after the desired exposure time (800, 70, 5, or 1 h) and analyzed using a fixed-bed reactor, which is described in Section 2.2.6.

2.2.5.2 Sample Preparation for Thermogravimetric Analysis

Samples used for TGA measurements were prepared by mixing approximately 25−50 mg of carbon with 70−90 uL of liquid DMMP and subsequently sonicated for 5 min to ensure that DMMP penetrated the pores. This impregnation method completely saturates the internal pore structures with liquid DMMP. The samples were then subjected to flowing Ar for sufficient time (>24 h) to remove excess liquid DMMP and desorb the weakly bound DMMP from the carbon. This exposure method allowed us to separate the differences between weakly bound DMMP and strongly bound DMMP (*i.e.* DMMP that remains adsorbed on the carbons and needs to be removed by heating) in a fast, reproducible fashion. After the 24 h purge, TGA experiments showed minimal

weight loss after flowing 100 mL min^{-1} of Ar over the sample for 60 min at room temperature.

2.2.6 Fixed-Bed Reactor Setup

TPD studies on the carbon samples were conducted using a temperature controlled fixed-bed reactor system. Each carbon sample (25 mg) was loaded into a 10 mm ID quartz reactor. The reactor was composed of a quartz frit with ~10 mg quartz wool layered atop the frit. The sample was placed on top of the wool. After loading the sample into the reactor, the system was sealed with Swagelok fittings, and Ar (Standard, Airgas) was flowed at a constant flow rate of 50 SCCM (standard cubic centimeters per minute). The mass flow was controlled with a Brooks 5850 series mass flow controller. A Eurotherm 91 P PID controller and K-type thermocouple controlled the sample temperature. All lines downstream of the reactor were maintained at a constant 150 °C before and during testing to minimize DMMP adsorption in effluent lines. Heating was initiated after 10 min of Ar purging at 30 °C to remove weakly physisorbed molecules, which was not collected for analysis. Then the effective adsorption capacity measurements were programmed to include the following temperature regimes:

(1) A linear temperature increase of 10 °C min^{-1}, from 30 °C to 450 °C

(2) Hold at 450 °C for 2 min

(3) A fast cooling to 30 °C

The reactor effluent was directed through a bubbler filled with a mixed solution of deuterated acetonitrile (CD_3CN) and ethylene carbonate (EC) that sufficiently submerged the bubbler stem. The CD_3CN/EC solution was maintained at 0 °C via an ice-water bath. The sample was analyzed using ^{1}H-NMR, which is described in Section 2.2.7.1.

2.2.7 Methods

2.2.7.1 ^{1}H-NMR Study

NMR spectra were recorded with a Bruker AV-400 MHz Spectrometer. For each spectrum, 128 transients were collected at 298 K with an acquisition time of 2.6 s, d1 relaxation time of 4 s. The DMMP-acetonitrile-d^3 solutions were spiked with precise amounts of EC to quantify the amount of DMMP desorbed.

2.2.7.2 Thermogravimetric Analysis (TGA)

All TGA related studies were performed by Mr. Scott Holdren in the Zachariah Lab. TGA at various heating rates (5, 10, 25, and 50 °C min^{-1}) was used to determine the effective desorption energy of DMMP from the OMCs and microporous carbons using a modified Flynn-Wall-Ozawa isoconversional method (eq. 2.1).[190]

$$ln\frac{\beta}{T_f^{1.92}} = -1.0008\frac{E}{RT_f} + C_6 \qquad \text{(eq. 2.1)}$$

where β is the heating rate, T_f is the temperature at a fixed conversion of the reaction (*i.e.* in this work it is defined as percent of DMMP desorbed), R is the

ideal gas constant, and E is the activation energy (desorption energy) for the process. An isoconversional method was chosen to analyze the DMMP desorption energies because these methods can be easily applied to a variety of reaction systems simply by knowing the T_f for various heating rates at a fixed point in the reaction process. An isoconversional method was chosen to analyze the DMMP desorption energies because these methods can be easily applied to a variety of reaction systems simply by knowing the T_f for various heating rates at a fixed point in the reaction process. These isoconversional methods (*e.g.* Kissinger, Ozawa) apply approximations to the temperature integral and a wide variety of approximations exist, which leads to numerous types of isoconversional methods available. The modified method was chosen because the Flynn-Wall-Ozawa isoconversional model can be inaccurate and lead to deviations in activation energy more than 10%.[191, 192]

TGA measurements were made using a TA Instruments SDT-Q600. For these experiments, pre-exposed DMMP carbons were purged with Ar >24 h, then placed in the TGA, purged for an additional 60 min under 100 ml min^{-1} of Ar, then heated to 450 °C at different heating rates. The desorption energy of DMMP was calculated at different DMMP coverages, where 0% DMMP desorbed was defined as the point at which heating begins for the kinetic analysis.

2.3 RESULTS AND DISCUSSION

2.3.1 Characterization of Ordered Mesoporous Carbons

In this investigation, we studied three different mesoporous carbons; the 1D cylindrical FDU-15, 3D hexagonal CMK-3, and 3D bicontinuous CMK-8, with well-defined pore size, volume, and surface area. Three microporous carbons were also investigated, disordered microporous BPL carbon, the zeolite-Y templated ordered microporous carbon (ZY), and sucrose derived disordered microporous carbon (SMC). The structures of the mesoporous and microporous carbons were first investigated using TEM. Figure 2.3 compares the TEM images of the 1D cylindrical mesoporous FDU-15, 3D hexagonal mesoporous CMK-3, 3D bicontinuous mesoporous CMK-8, and disordered microporous BPL carbon. The mesoporous carbons show uniform pore structure and pore size distributions of approximately 3 nm, in comparison to BPL, which shows disordered pores with pore sizes less than 2 nm.

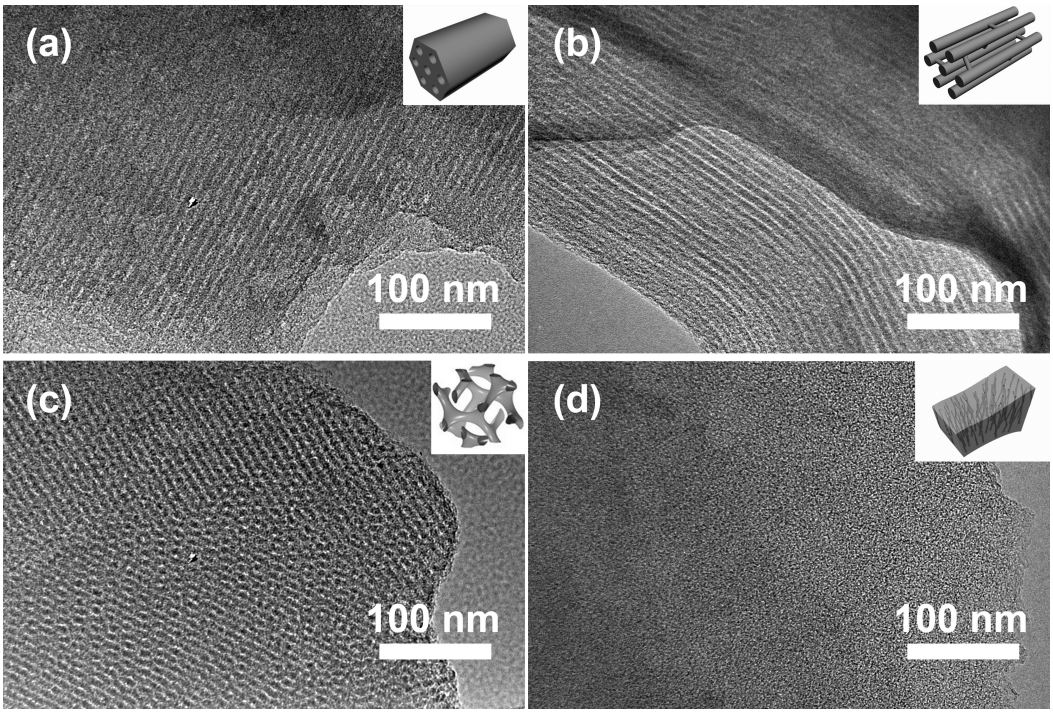

Figure 2.3. TEM images of (a) ordered mesoporous FDU-15, (b) ordered mesoporous CMK-3, (c) ordered mesoporous CMK-8 and (d) disordered microporous BPL. The inset cartoons show their general framework structures.

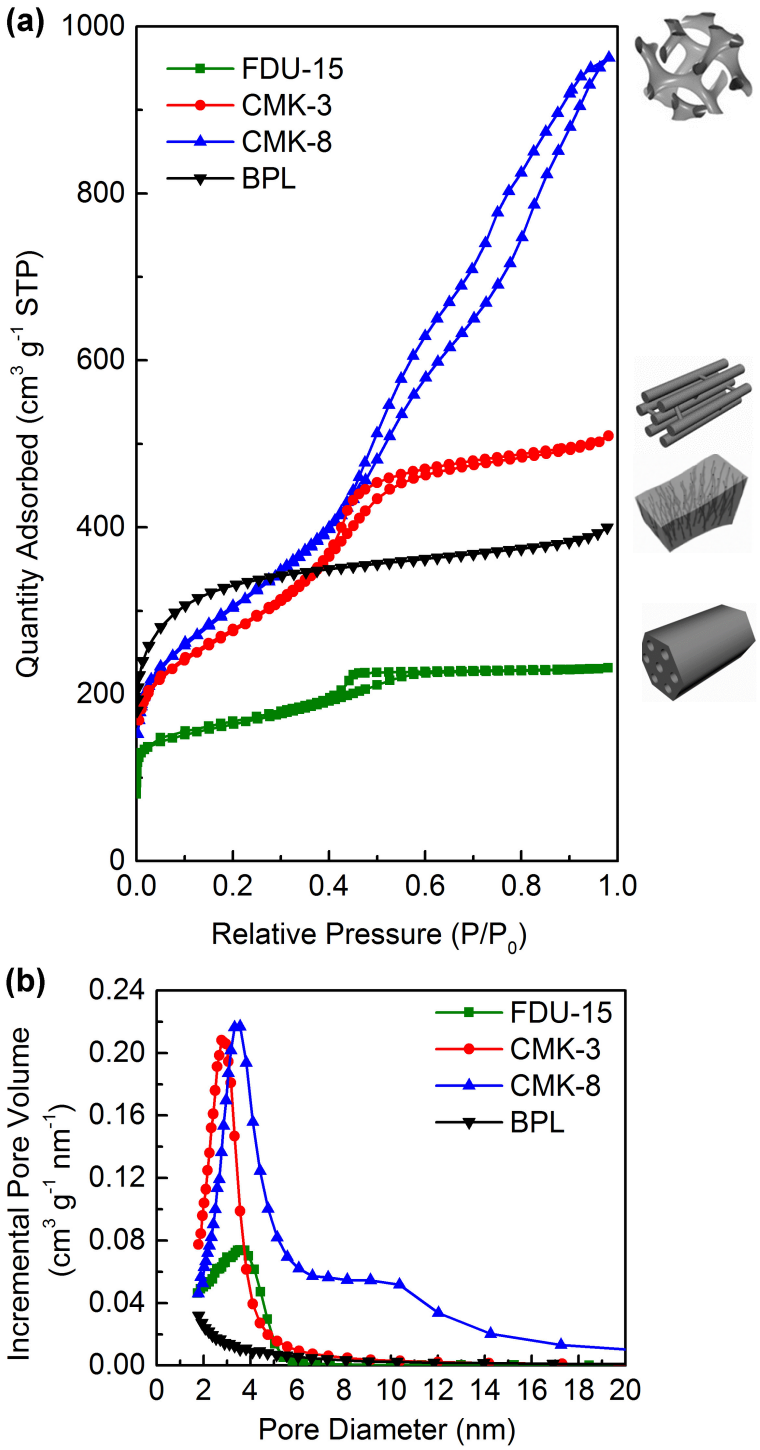

Figure 2.4. (a) N_2 adsorption-desorption isotherms and (b) BJH pore size distributions for the different carbon architectures, FDU-15, CMK-3, CMK-8, and BPL carbon.

The pore size and volume of the different carbons were compared by N_2 adsorption-isotherms. The detailed structure parameters are presented in Table 2.1. Based on the isotherms in Figure 2.4a, all three OMCs show typical Type-IV isotherms with hysteresis, in good agreement with their mesoporosity.[50] The different pore structure, network, and size distributions are evident by the type of hysteresis loops in Figure 2.5a and further illustrated in Figure 2.4b. FDU-15 and CMK-3 have Type H1 hysteresis loops, indicating cylindrical pore geometry and a narrow pore distribution with peak maxima at 3.5 and 2.8 nm, respectively. CMK-8 has Type H4 hysteresis, which is associated with a wide pore distribution represented by the bimodal porosity in Figure 2.4b, with a clear maximum at 3.6 nm. In contrast, BPL shows a Type-I isotherm with relative P/P_0 change below 0.2, which indicates its microporosity with relatively small mesopore/external surfaces.[193] The OMCs, FDU-15, CMK-3, and CMK-8, have similar mesopore sizes of 2.8−3.6 nm, in comparison with microporous BPL with pore sizes less than 1.7 nm. These data are in good agreement with the pore sizes measured from the TEM studies and previous studies in the literature.[19-21]

Table 2.1 also compares the surface area and pore volume of the different carbons. In general, FDU-15 shows the smallest surface area of 600 $m^2\ g^{-1}$, while the surface area of CMK-3 (976 $m^2\ g^{-1}$), CMK-8 (1075 $m^2\ g^{-1}$), and BPL (1229 $m^2\ g^{-1}$) are similar. The total pore volume of the carbons follows FDU-15 < BPL < CMK-3 < CMK-8. The pore volume of CMK-8 is 1.136 $cm^3\ g^{-1}$, which is more

than double that of the other carbons. The different pore properties will influence the adsorption and desorption properties of DMMP, which will be discussed in detail below.

Table 2.1. N_2 Adsorption –Desorption Properties of OMCs and BPL Carbon

Carbon Sample	Pore Diameter (nm)[a]	Total Pore Volume (cm^3 g^{-1})[b]	Total Surface Area (m^2 g^{-1})[c]	Mesopore Surface Area (m^2 g^{-1})[a]
FDU-15	3.6	0.325	600	223
CMK-3	2.8	0.454	976	462
CMK-3*	2.7	0.669	1280	728
CMK-8	3.5	1.136	1075	774
BPL	<1.7	0.391	1229	72

[a]Calculated using the Barrett-Joyner-Halenda (BJH) model.

[b]The total pore volume is based on the sum of the mesopore and macropore volume from the BJH model and the micropore volume from the t-plot method.

[c]Calculated using the multipoint Brunauer-Emmett-Teller (BET) method.

2.3.2 DMMP Adsorption on Different Carbon Architectures

Plots of DMMP uptake versus time (t) up to 800 h are shown in Figure 2.5. The adsorption curves are similar for all carbons, with an initial rapid increase in the first 80 h, followed by a saturation region, typical of adsorption processes. After 50 h, the 3D bicontinuous CMK-8 has the highest DMMP uptake, followed by CMK-3, FDU-15, and BPL, respectively. The slower adsorption rates for the other carbons may be due to slower diffusion of DMMP

into the less accessible interior channels after the surface sites become saturated with adsorbed DMMP. A similar saturation curve seen in Figure 2.5 was observed by Khanday *et al.*[194] and Saxena *et al.*[69] in their studies of DMMP adsorption in different zeolites from 2−18 h and activated carbons from 0−600 h, respectively. The adsorption of DMMP in FDU-15 saturates at approximately 0.3 g DMMP/m^2 carbon at 400 h, which represents filling of the total pore volume of the material. While the time-to-saturation was not measured for the other the three samples, their 800 h capacities represent filling of the total pore volumes and can be considered the saturation limit, as discussed below.

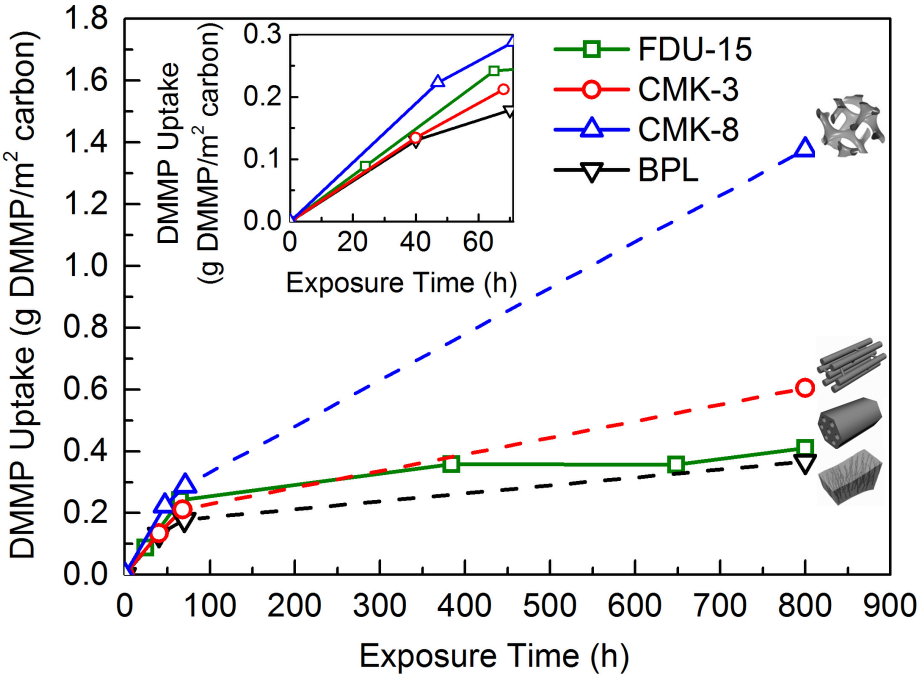

Figure 2.5. Plot of DMMP uptake as a function of time for the ordered mesoporous carbons and microporous BPL carbon. The inset shows initial uptake of DMMP in the first 60 h before the plateau region. The dotted lines represent extrapolations from the 60 h data to the fully saturated systems. The time-to-saturation was not measured in these systems.

2.3.3 TPD Studies of DMMP from Different Carbon Architectures

TPD experiments were conducted to determine the adsorption capacity and kinetics of DMMP desorption. After 800 h of DMMP exposure, the pores are fully saturated with liquid DMMP,[174] as evidenced by the linear relationship between adsorption capacity and total pore volume, shown in Figure 2.6.

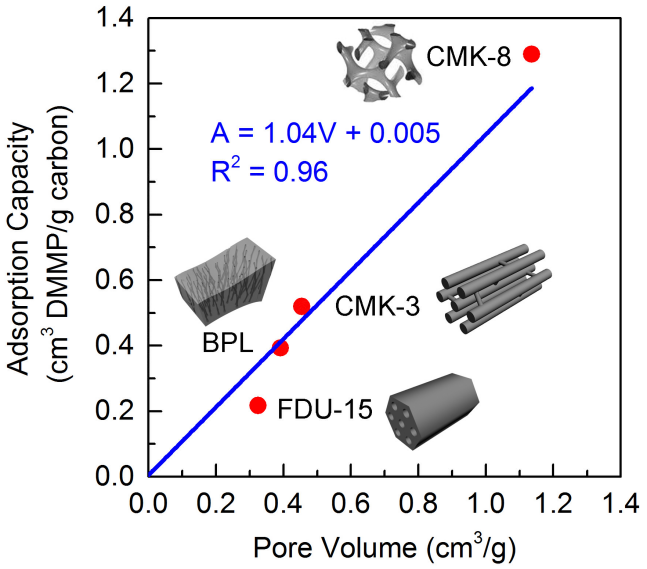

Figure 2.6. The adsorption capacity after 800 h of DMMP exposure for all carbons (red dots) with different total pore volumes. A fitted linear curve of adsorption capacity versus pore volume (blue line) was added.

To probe the adsorption regime between full surface coverage and liquid saturation, we evaluated samples after 70 h and 5 h of DMMP exposure. Excluding BPL, there is a general linear correlation between DMMP uptake and the total surface area of the OMCs (Figure 2.7a and b). This relationship between DMMP adsorption and the surface area is similar to that observed by Khanday *et al.* when comparing DMMP adsorption in four different zeolite samples (Zeolite

X, Erionite, MCM-22, and Zeolite-A),[6] where liquefaction has not occurred. BPL presumably does not follow this trend since the majority of its porosity originates from micropores and competing processes, such as the onset of liquefaction and diffusion through micropores versus mesopores, which may be confounding effects. After longer exposure times (70 h), the BPL mass adsorption deviates less from the linear trend (Figure 2.7a), which we believe is a result of micropore filling and less competing processes.

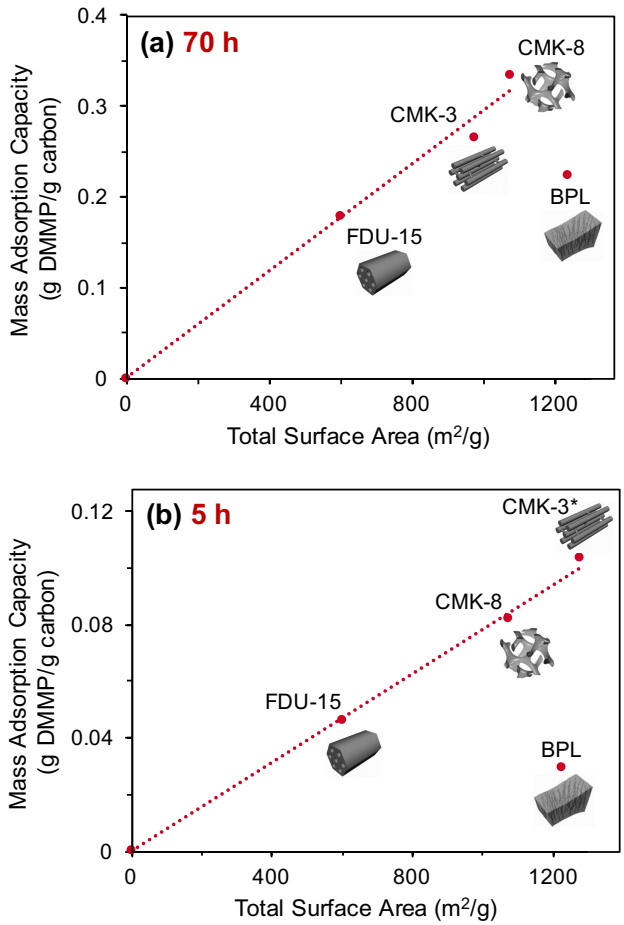

Figure 2.7. Adsorption capacity after (a) 70 h and (b) 5 h of DMMP exposure in relationship to the total surface area of the different carbon structures.

To further investigate DMMP adsorption properties before liquefaction, we evaluated samples after 1 h of DMMP exposure. Previous studies state that initial adsorption occurs in the micropores, which is more thermodynamically stable.[50, 92] It was experimentally difficult to prove the adsorption process within the micropores as discrete steps (for example, first surface coverage then micropore filling) for a few reasons. First, pore sizes <0.6 nm are inaccessible to DMMP due to sterical reasons (which will further be described in Section 2.4.4); therefore, those pores will remain vacant during DMMP exposure. Second, it is uncommon to use terms like "surface area" and "pore volume" separately to describe a measurement of available adsorption sites for pore diameters <2 nm, since the entire pore represents a space where adsorption may occur. For instance, given the size of DMMP (~0.6 nm),[195] monolayer adsorption on the opposite walls of the micropore could be close enough that it leads to pore filling.[50, 174, 193] Therefore, after 1 h of DMMP exposure, we speculate that the accessible micropores (0.6–2 nm) are filled and the continuous adsorption of DMMP occurs as a monolayer across the surface of the mesopores. This notion is supported by a linear correlation between DMMP mass adsorption and the mesopore surface area for all four carbons, as shown in Figure 2.8.

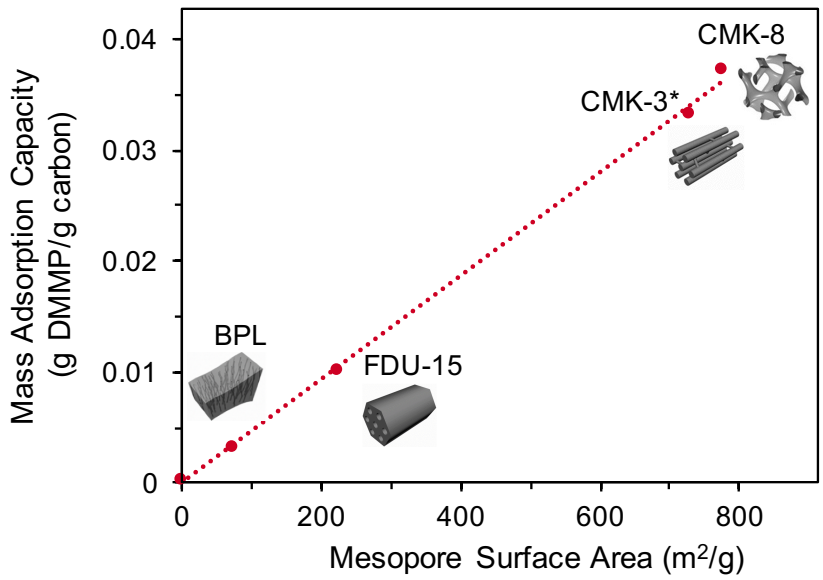

Figure 2.8. Adsorption capacity after 1 h of DMMP exposure in relationship to the mesopore surface area of the different carbon structures.

2.3.4 Desorption Energies of DMMP

DMMP desorption energies for the microporous carbons and the OMCs were determined at various surface coverages using the modified Flynn-Wall-Ozawa isoconversional method, described in the experimental section 2.6.2. For these experiments, the carbons were saturated with liquid DMMP and purged with Ar for >24 h before the analysis to remove loosely-bound DMMP on the surface, and in the majority of the mesopores. After the purge, the remaining DMMP for all carbons resides predominately in the pores that are ≤2.4 nm in diameter, as evidenced by the linear relationship between DMMP content and cumulative pore volume shown in Figure 2.9. This relationship was empirically derived from the TGA DMMP weight loss and NLDFT N_2 adsorption pore volume measurements

(Figures 2.10a and b). Based on Figures 2.10a and b, cumulative pore volumes of other pore sizes were investigated (1.8 to 2.6 nm) and fitted to the observed TGA DMMP weight loss (Table 2.2). We found that 2.0−2.4 nm range provided the best linear fit of the data. Although the remaining strongly bound DMMP resides in pores ≤2.4 nm for all the carbons tested, the cumulative volume for these pores are all different due to the carbons unique internal structures. As such, the desorption energies measured in the study represent DMMP desorption from carbon pores ≤2.4 nm in diameter.

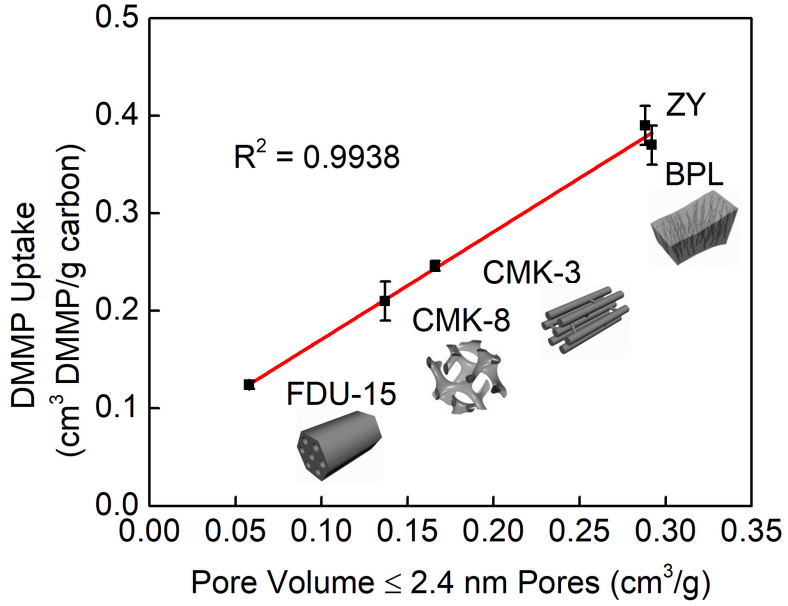

Figure 2.9. DMMP uptake versus cumulative pore volume ≤ 2.4 nm.

Table 2.2. R^2 Coefficients Measured Based on the Linear Fit of DMMP Remaining on the Different Carbons

NLDFT Pore Size Range (nm)[a]	R^2 [b]
0−2.6	0.9577
0−2.4	0.9938
0−2.2	0.9933
0−2.0	0.9954
0−1.8	0.9549

[a]Calculated from the adsorption branch based on NLDFT, with a relative pressure beginning at 0.001.

[b]Calculated from the linear fit of DMMP uptake with respect to the pore volume from different pore size ranges.

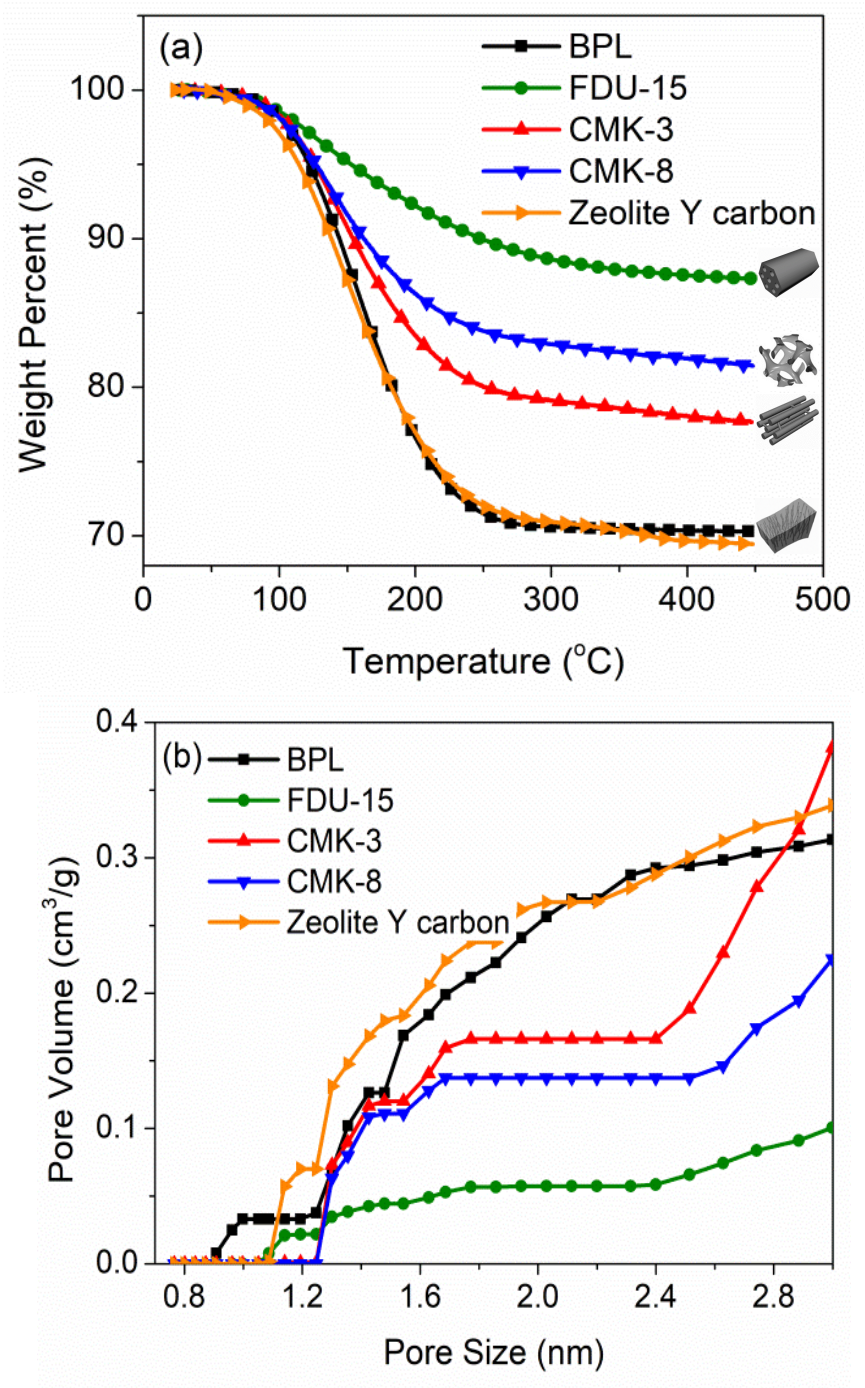

Figure 2.10. (a) TGA curves of DMMP exposed carbon samples at 10 °C min^{-1}. TGA curves were normalized to 100 wt% after a 60 min Ar purge. The amount of DMMP desorbed follows the same trend as the cumulative pore volume of pores ≤2.4 nm (b) NLDFT N_2 adsorption pore volume measurements for different carbons tested.

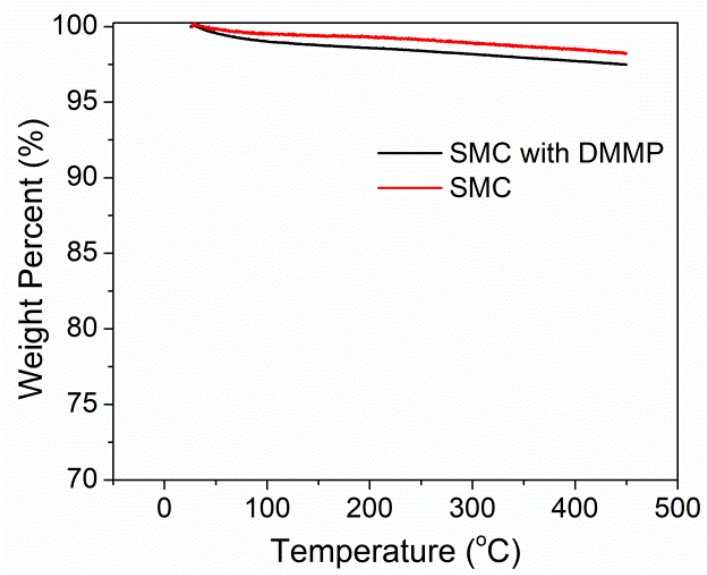

Figure 2.11. TGA of SMC (red) and DMMP exposed SMC (black). There is a slightly larger weight loss for the DMMP exposed SMC sample.

In addition to the four carbons described previously, two microporous carbons were also tested to obtain a better understanding of how the structure and porosity affects the experimentally determined DMMP desorption energies. One of these carbons is a sucrose derived microporous carbon (SMC) detailed in Xu *et al.* and the other is a microporous zeolite Y template (ZY) derived carbon described by Johnson *et al.*[182, 183] All six of these carbons were exposed to liquid DMMP, as described in the previous Section 2.2.5.2. When SMC was exposed to DMMP, TGA showed that very little to no DMMP was absorbed (Figure 2.11). According to Xu *et al.*, the average pore size of SMC is 0.5 nm, which is too small for DMMP to penetrate the pores.[17] This aligns well with previous estimates of the size of a DMMP molecule, which is ~0.6 nm.[195] Therefore, no DMMP

desorption energies could be determined for SMC. TGA curves of DMMP desorption from BPL carbon at different heating rates are presented in Figure 2.12a.

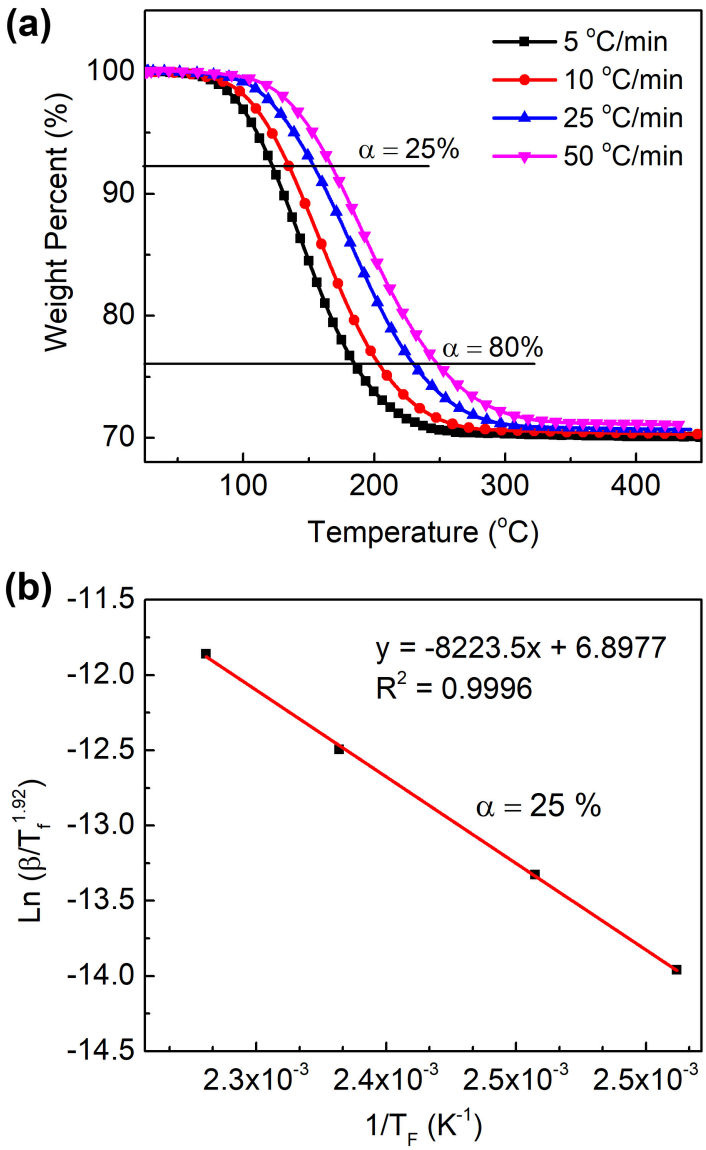

Figure 2.12. (a) TGA curves of DMMP desorption from BPL carbon at different heating rates. The TGA curves were normalized to 100 wt% after the second purge (60 min under 100 ml min^{-1} of Ar). (b) Representative desorption energy determination of DMMP desorption from BPL carbon at 25% DMMP desorbed. The error bars in plot (b) are smaller than the symbols.

The temperature at various DMMP desorption percentages (α) for each TGA curve were fitted to the Flynn-Wall-Ozawa isoconversional method, shown in Figure 2.12b, to extract a DMMP desorption energy. These DMMP desorption energies for the different carbons were calculated as a function of % DMMP desorbed (α), and shown in Figure 2.13.

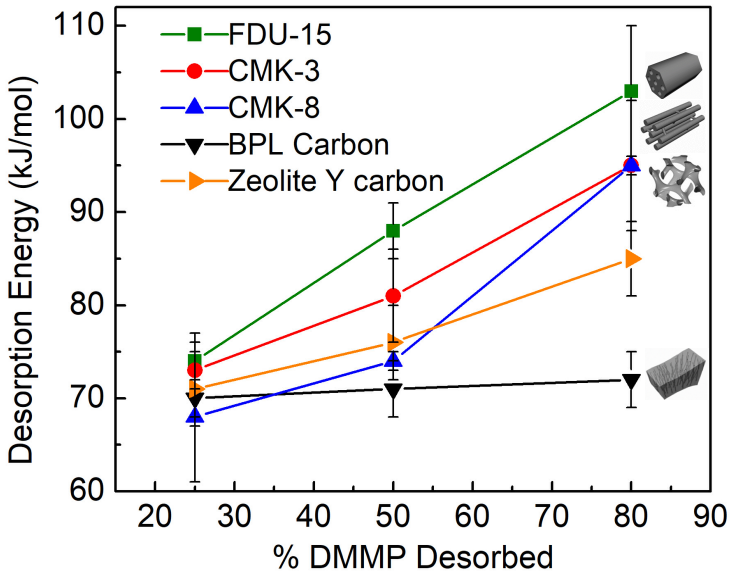

Figure 2.13. DMMP desorption energies from carbon samples.

The DMMP desorption energies from the five different carbon samples are shown in Figure 2.13 as a function of the % DMMP desorbed (α). At α = 25%, the desorption energies for all carbon structures are similar, ranging from 68−74 kJ mol^{-1}. With an increase in fraction desorbed, the apparent activation energy also increases, with the exception of BPL, which is relatively constant. At α = 80%, the desorption energies for the synthetic OMCs are 95−103 kJ mol^{-1}, a

30−40% increased. All of these desorption energies are above the DMMP heat of vaporization (ΔH_{vap}), which is 52 kJ mol^{-1}, but are significantly lower than covalent bonds,[196] implying that DMMP-carbon interactions are best characterized as physisorption.

The origin of the increase in desorption energy in our systems relative to the ΔH_{vap} is not entirely clear but we propose two possible explanations. At α = 25%, most of the DMMP presumably resides on the pore walls, which could facilitate weak Van der Waals type interactions (*i.e.* weak physisorption) that could increase the desorption energy relative to ΔH_{vap}. This scenario is similar to the hydrogen bonding interactions of DMMP to silica proposed by Wilmsmeyer *et al.* and Henderson.[14, 197] Alternatively, the increase from the ΔH_{vap} value may arise from the DMMP vapor pressure suppression due to capillary condensation.[50, 193] The carbon porosity allows liquid DMMP to become entrapped in the micropores, which suppresses the vapor pressure of DMMP requiring additional energy (16−22 kJ mol^{-1}). This proposal is reminiscent of the entrapment model advanced by Ferguson-McPherson *et al.*[30]

The origin of the 30−40% increase in OMCs when α = 80% desorption energies relative to the α = 25% values is also unclear. Since the BPL sample did not show the same increase, we evaluated ZY, given that both BPL and ZY have large microporosity, and similar DMMP adsorption capacities (Figure 2.10a). However, ZY has an ordered microstructure imparted by the zeolite template,

whereas BPL has a random, disordered microporous network. As shown in Figure 2.13, the desorption energy at $\alpha = 80\%$ for ZY increases by 15% relative to the $\alpha = 25\%$, in contrast to the behavior of BPL. While the increase is less than that of the OMCs, the data suggests that the increases at lower coverage of the templated carbons originates from their ordered network structures. Li *et al.* has reported similar trends in the desorption of naphthalene and acenaphthene from a bituminous coal activated carbon (similar to BPL). These investigators measured desorption energies of approximately 60 kJ mol^{-1}, which remained constant throughout the entire desorption process.[151] In a subsequent study, Li *et al.* measured a naphthalene desorption energy of 74 kJ mol^{-1} from the mesoporous carbon CMK-3.[181] These investigators observed a 23% increase in desorption energy for naphthalene and CMK-3, relative to BPL, which is similar to our findings, and further suggests that the ordered nature of the carbon networks increases desorption energies at low surface coverages.

2.4 CONCLUSIONS

We have demonstrated from various DMMP exposure times: 1, 5, 70, and 800 h, that adsorption of DMMP is initially influenced by the mesopore surface area, then total surface area, and the pore volume after liquefaction in each OMC. In addition, the amount of energy required to desorb low coverage DMMP from the OMCs is dependent on the pore properties of each carbon, and the weakly bound DMMP on the carbon surface or in pores >2.4 nm will readily desorb at

room temperature, and no DMMP will absorb in pores smaller than 0.5 nm. The desorption energies of the remaining physisorbed DMMP are primarily a measurement of the heat of vaporization and excess energy due to either weak Van der Waals interactions or vapor pressure suppression from capillary condensed DMMP in pores ≤2.4 nm. At lower surface coverages (α = 80), the DMMP desorption energies are 20−30 kJ mol^{-1} higher for the ordered micro- and mesoporous carbons but remains relatively constant for BPL. These data suggest that diffusion barriers and transport through an ordered network increases the effective desorption energies.

A few important generalizations can be made for designing new adsorption materials. First is that maximizing the mesopore volume of a carbon leads to a larger adsorption capacity. Second, the most tightly-bound DMMP molecules reside in the pores between 0.6−2.4 nm. Third, ordered architectures give rise to higher apparent desorption energies that may be associated with transport barriers.

Chapter 3: Endo-pore and Exo-pore Copper Oxide Deposition in Ordered Mesoporous Carbons: Synthesis, Structures, and Adsorption/Decomposition Properties

3.1 INTRODUCTION

The adsorption process is commonly used for purification purposes with gas mask filters employing two types of adsorption, physisorption and chemisorption, to remove chemical warfare agents (CWAs) from the airstream.[24, 33, 49, 50] Dimethyl methylphosphonate (DMMP), a CWA simulant, is widely studied to investigate the adsorption process involved in CWA removal. In Chapter 2, our studies revealed that DMMP binding to unimpregnated carbons can be characterized as physisorption, a product of Van der Waal's interactions. The desorption energy calculated for the tightly bound DMMP molecules at low surface coverages (80% DMMP desorbed relative to capacity), ranged from 68−103 kJ mol^{-1} for microporous (BPL, ZY) and mesoporous (FDU-15, CMK-3, and CMK-8) carbons, which is similar to the heat of vaporization (52 kJ mol^{-1}). Given that DMMP is not strongly bound to carbon, the adsorptive properties are enhanced by metal oxide impregnation. It is well-known that DMMP chemisorbs to metal oxides (consequently increasing the enthalpy of adsorption), and/or alternatively decomposes DMMP into nontoxic byproducts.[70, 76, 198] Additional reasons to incorporate metal oxide nanoparticles include, gas adsorption of

molecules that do not bind to carbon (broader target spectrum), increased adsorption capacity and reactive sites, and reduction of the amount of adsorbent needed in a canister by optimizing the surface-to-volume ratio. Specifically, this will result in smaller, lighter, and more portable gas-masks for field use.

Previous studies have shown that the impregnation of activated carbons with metals such as, Mn, Co, Ni, Fe, Cu, Zn, Ag, Cr, Mo, and V, can increase the removal of toxic gases not typically removed by carbon.[76, 93, 199, 200] Particularly, Cu/CuO has proven to be promising due to an increased efficiency in adsorbing and decomposing CWA simulants and TICs, such as DMMP and ammonia, as demonstrated by Ji *et al*.,[201] Petit *et al*.,[100] and our collaborators at the University of Maryland (Dr. Maija Kuklja, Dr. Michael Zachariah), Naval Research Lab (Dr. Jeffrey Owrutsky, Dr. Jeffrey Long), and Lawrence Berkley National Lab (Dr. Hendrik Bluhm).[31] The carbon support and the CuO properties are expected to influence the DMMP adsorption and decomposition properties, based on our observations in Chapter 2.

In this chapter, we investigated CuO impregnated carbon systems, which represents one of the deconstructed analogs of ASZM-TEDA. A diverse group of model systems with strategically placed impregnants inside (endo) and outside the porous network (exo-pore) were synthesized. The model compounds include, BPL with exo-pore CuO, OMCs (FDU-15, CMK-3, and CMK-8) with endo-pore CuO, and FDU-15 with endo and exo-pore CuO. Our studies with these synthetic

CuO endo and/or exo-pore carbons further our understanding of CuO functionality within the adsorbent and investigate the sources of ASZM-TEDA deactivation, such as impregnant migration and poisoning of the surface with phosphorus species[202] (previously discussed in Chapter 1). Additionally, it was discovered that CuO impregnation increases adsorption capacity and reactivity, in comparison to carbon adsorbents. The extent of DMMP decomposition is higher for nano sized endo-pore CuO, relative to larger exo-pore CuO particles. The DMMP decomposition product observed is gaseous methanol, which presumably creates a methyl methylphosphonate (MMP) byproduct on the surface, and consequently, deactivates the adsorbent.

3.2 EXPERIMENTAL SECTION

3.2.1 Materials

AR grade dimethyl methylphosphonate (≥97.0%) (DMMP) was purchased from Sigma Aldrich (USA) and used without further purification. The commercial activated carbon, BPL (12x30 mesh), was supplied by the U.S. Army Edgewood Chemical and Biological Center.

3.2.2 CuO Deposition on BPL

In a typical reaction, 0.1 g BPL was washed with deionized water (2 mL), and collected by vacuum filtration to remove any impurities. Then, BPL was fully saturated with a $Cu(NO_3)_2$ aqueous solution (8 wt%) for 4 h. The BPL filled with

$Cu(NO_3)_2$ aqueous solution was collected by centrifugation (14000 rpm, 1 min). The saturation/collection process was repeated three times. Next, the excess solution was removed by vacuum filtration. The BPL/$Cu(NO_3)_2$ solid was dried in a box furnace at 90 °C for 6 h. The final product was annealed at 380 °C for 5 h under Ar flow, with a heating rate of 1 °C min^{-1}. The resulting solid was annealed a second time to 250 °C in air, with a heating rate of 1 °C min^{-1} (Figure 3.1). The CuO impregnated BPL was collected and characterized.

3.2.3 CuO Impregnation for OMCs

The OMCs, FDU-15, CMK-3, and CMK-8, were prepared using slight modifications of methods as described in Chapter 2, Section 2.2.3.1−2.2.3.3, and in the literature.[184-186] These OMCs were later impregnated with CuO nanoparticles by Dr. Junkai Hu.

3.2.3.1 CuO Endo-pore and/or Exo-pore Impregnation

In a typical reaction, 0.1 g OMC (FDU-15, CMK-3, CMK-8) was washed with deionized water (2 mL), and collected by vacuum filtration to remove any impurities. Then, OMC was fully saturated with a $Cu(NO_3)_2$ aqueous solution (8 wt% for FDU-15, 3.5 wt% for CMK-3 and CMK-8) for 4 h. The OMC filled with $Cu(NO_3)_2$ aqueous solution was collected by centrifugation (14000 rpm, 1 min). The saturation/collection process was repeated three times. Next, the excess solution was removed by vacuum filtration. The OMC/$Cu(NO_3)_2$ solid was dried

in a box furnace at 100 °C for 6 h. The final product was annealed at 380 °C for 5 h under Ar flow, with a heating rate of 1 °C min^{-1}. The resulting solid was annealed a second time to 250 °C in air, with a heating rate of 1 °C min^{-1} (Figure 3.1). The CuO impregnated carbons were collected and characterized.

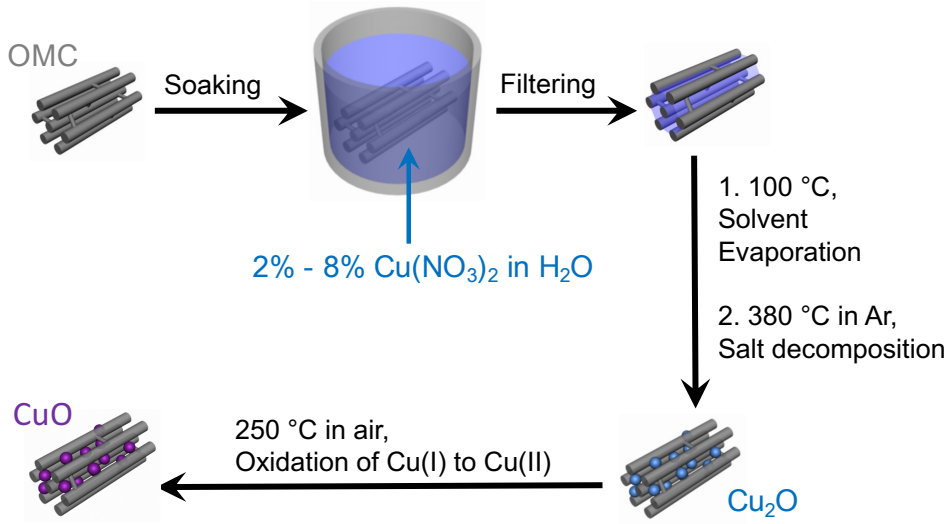

Figure 3.1. Schematic of the impregnation process for copper oxide into and/or onto the OMC pores.

3.2.3.2 Selective Removal of Exo-pore CuO

FDU-15 was impregnated with CuO as described in Section 3.2.3.1, except FDU-15 was fully saturated with a higher concentration $Cu(NO_3)_2$ aqueous solution (40 wt%). In a typical reaction, 0.1 g FDU-15/CuO (11.7 CuO wt%) was fully saturated by nonane (2 mL) for 1 h to protect the endo-pore CuO nanoparticles. The FDU-15/CuO filled with nonane was collected by centrifugation (14000 rpm, 1 min). Next, 1M H_2SO_4 (2 mL) was added, stirred for 0.5 min, then immediately washed with deionized water (2 mL), and collected by

centrifugation (14000 rpm, 1 min). The endo-pore CuO impregnated FDU-15 was dried in a box furnace at 160 ºC overnight (Figure 3.2).

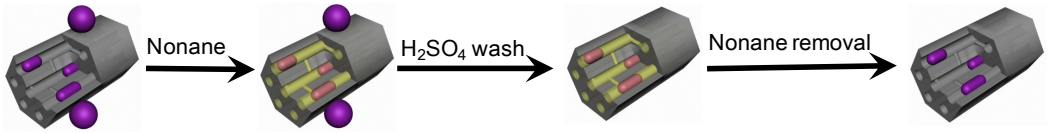

Figure 3.2. Schematic of the selective removal of exo-pre CuO from FDU-15 originally with endo and exo-pore CuO nanoparticles.

3.2.4 Characterization of Adsorbents

Pore size, volume, and surface area were determined from N_2 adsorption-desorption isotherms recorded with a Micromeritics ASAP 2020 Porosimeter Test Station. Samples were degassed in vacuum at 100 °C for 12 h prior to characterization. The specific surface areas were calculated using the BET method from the N_2 adsorption data in the relative pressure range (P/P_0) of 0.05−0.20. The general porosity distribution was calculated from the adsorption branch using the Barrett-Joyner-Halenda (BJH) equation.

Structural morphologies of the samples were imaged with a scanning electron microscope (Hitachi SU-70 SEM, operated at an acceleration voltage of 10 kV) and a transmission electron microscope (JEM 2100 Field Emission operated at 200 kV). The samples were dispersed in methanol and a 10 μL aliquot of the resulting dispersion was drop cast on the TEM grids. The TEM grids used were carbon-coated Cu grids (CF200-Cu, Electron Microscopy Sciences). X-ray diffraction (XRD) patterns were recorded by a Bruker Smart1000 (Bruker AXS

Inc., USA) using CuKα radiation.

The copper content of the carbon/CuO composites was determined using inductively coupled plasma-atomic emission spectroscopy (ICP-AES) characterization performed on a Perkin Elmer ICP Optima 4700. The samples were dissolved in pure trace-metal grade nitric acid (Sigma-Aldrich) and diluted with milli-Q water to a known volume (100 mL) with a final concentration of 2 wt% nitric acid (HNO_3), before administered to the plasma. Intensities were measured at 327.396 nm for Cu. A linear calibration curve (R^2 = 0.9999) was collected with five standards, a blank (2 wt% HNO_3), 0.1, 0.2, 0.5, and 1.0 ppm Cu (High Purity Standard, 1000 μg/g Cu in 2 wt% HNO_3).

3.2.5 Exposure of Adsorbents to DMMP

Adsorbent materials were pre-treated at 100 °C for ≥6 h under static vacuum to remove any adsorbed contaminants before exposure to DMMP using the vial-in-vial method, modified from the literature.[189] Approximately 35−100 mg of material was transferred to small glass vials. Each small glass vial was placed inside a larger vial that contained a sufficient amount of liquid DMMP (200 μL) to saturate the head space of the vial assembly. The larger vial was then capped, and stored in a desiccator. The exposure process was conducted under ambient pressure at room temperature (24−26 °C). The samples were then

removed after the desired exposure time (5 or 70 h) and analyzed using a fixed-bed reactor, which is described in Section 3.2.6.

3.2.6 Fixed-Bed Reactor Setup

TPD studies were conducted using a temperature controlled fixed-bed reactor system. Each sample was loaded into a 10 mm ID quartz reactor. The reactor was composed of a quartz frit with ~10 mg quartz wool layered atop the frit. The sample was placed on top of the wool. The system was sealed with Swagelok fittings, and Ar (Standard, Airgas) was flowed at a constant flow rate of 50 SCCM (standard cubic centimeters per minute). The mass flow was controlled with a Brooks 5850 series mass flow controller. A Eurotherm 91 P PID controller and K-type thermocouple controlled the sample temperature. All lines downstream of the reactor were maintained at a constant 150 °C before and during testing to minimize DMMP adsorption in effluent lines. Heating was initiated after 10 min of Ar purging at 30 °C to remove weakly physisorbed molecules, which was not collected for analysis. Then the effective adsorption capacity measurements were programmed to include the following temperature regimes:

(4) A linear temperature increase of 10 °C min^{-1}, from 30 °C to 450 °C

(5) Hold at 450 °C for 2 min

(6) A fast cooling to 30 °C

The reactor effluent was directed through a bubbler filled with a mixed solution of deuterated acetonitrile (CD_3CN) and ethylene carbonate (EC) that sufficiently submerged the bubbler stem. The CD_3CN/EC solution was maintained at 0 °C via an ice-water bath. The sample was analyzed using ^{1}H-NMR, which is described in Section 3.2.7.1.

3.2.7 Methods

3.2.7.1 Quantitative ^{1}H-NMR

NMR spectra were recorded using a Bruker AV-400 MHz Spectrometer. For each spectrum, 128 transients were collected at 298 K with an acquisition time of 2.6 s, d1 relaxation time of 4 s. The DMMP-acetonitrile-d^3 solutions were spiked with precise amounts of EC that was added as a quantitative calibrant to measure the amount of DMMP and byproducts desorbed.

3.2.7.2 ICP-AES Analysis

The phosphorus content of the cycled adsorbent materials were determined using ICP-AES characterization performed on a Perkin Elmer ICP Optima 4700. The samples were dissolved in pure trace-metal grade nitric acid (Sigma-Aldrich) and diluted with milli-Q water to a known volume (100 mL) with a final concentration of 2 wt% nitric acid (HNO_3), before administered to the plasma. Intensities were measured at 177.5 and 178.3 nm for P. A linear calibration curve (R^2 = 0.9999) was collected with five standards, a blank (2 wt%

HNO_3), 0.1, 0.2, 0.5, and 1.0 ppm P (High Purity Standard, 1000 μg/g P in 2 wt% HNO_3).

3.3 RESULTS AND DISCUSSION

3.3.1 Characterization of CuO Impregnated Carbons

Five samples of carbon/CuO composites: BPL with exo-pore CuO, OMCs (FDU-15, CMK-3, and CMK-8) with endo-pore CuO, and FDU-15 with CuO endo and exo-pore, were prepared and characterized. The diverse group of model systems are used to probe the influence of CuO on DMMP adsorption and decomposition, which will further be discussed in Section 3.3.2−3.3.3.

3.3.1.1 CuO Particle Size, Distribution, and Morphology

The particle size, distribution, and morphology of the CuO impregnants were characterized using electron microscopy, TEM and SEM. TEM images of the spherical CuO impregnants revealed 2−4 nm particles evenly distributed inside the pores and 30−50 nm exo-pore particles/large aggregates on the surface, which was further confirmed with SEM (Figure 3.3).

Aggregates of CuO particles were formed on the external surface of BPL after CuO impregnation process. We speculate that this aggregation process is caused by the inability of the $Cu(NO_3)_2$ precursor solution to enter the pores of the activated carbon.[199] In Figure 3.4a-d, a micron-sized CuO aggregate on the BPL

surface was confirmed using SEM/EDX, which appears similar in size and morphology to unsupported commercial CuO mixed with BPL (Figure 3.4e).

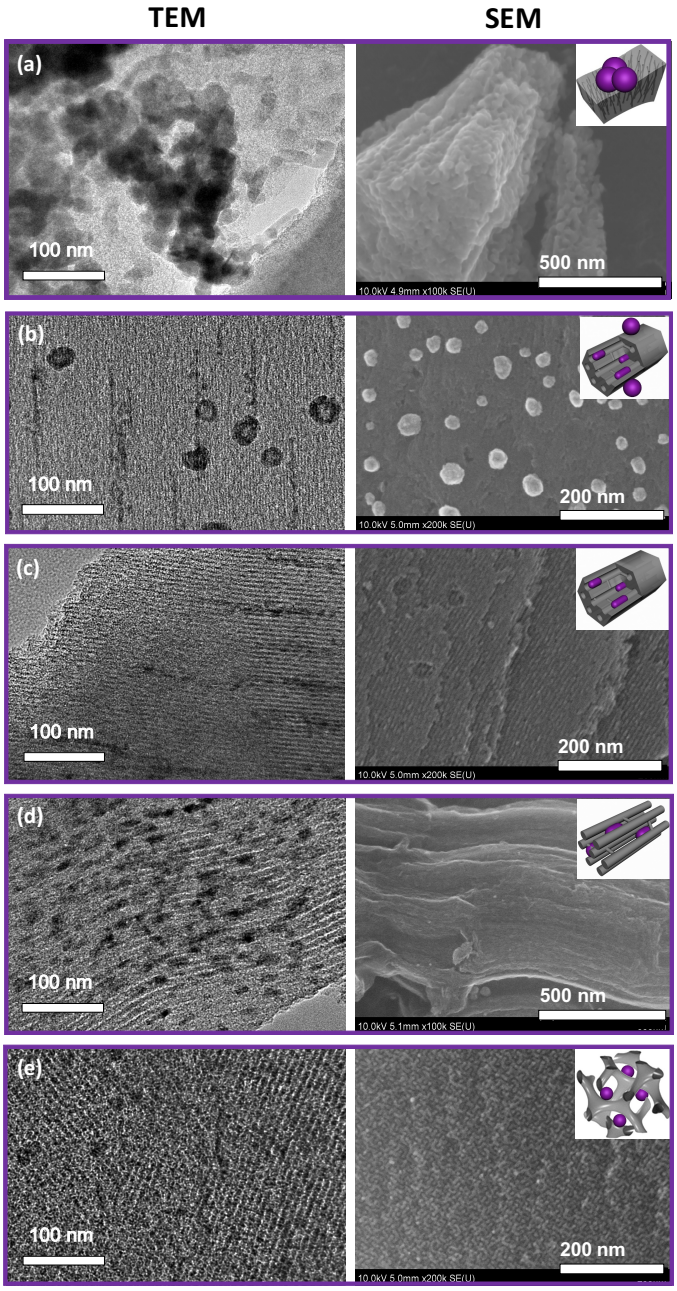

Figure 3.3. TEM and SEM images of the carbon/CuO composites: (a) BPL/CuO (exo-pore), (b) FDU-15/CuO (endo and exo-pore), (c) FDU-15/CuO (endo-pore), (d) CMK-3/CuO (endo-pore), and (e) CMK-8/CuO (endo-pore).

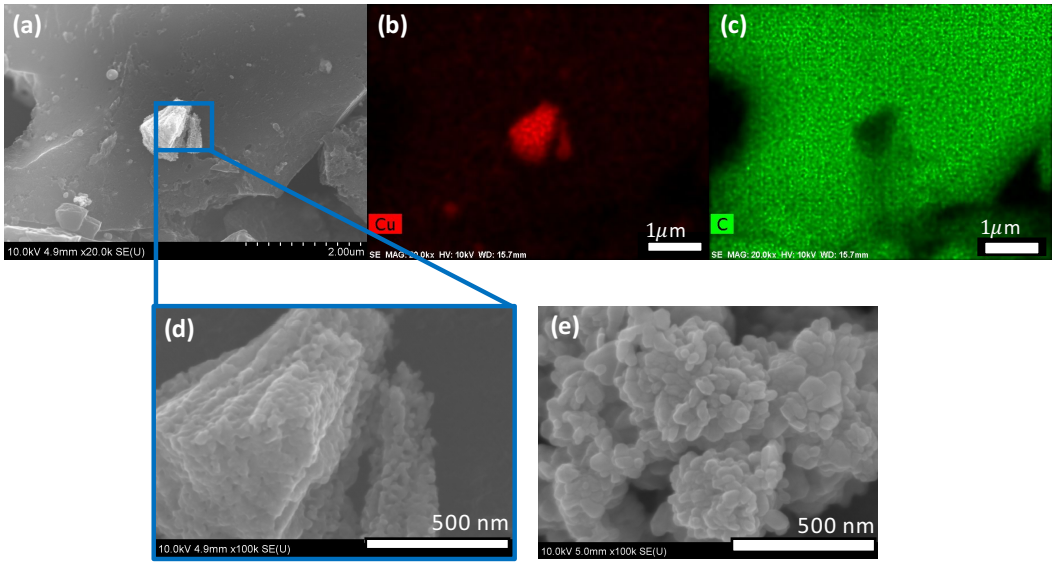

Figure 3.4. SEM image of (a) BPL/CuO with (b) Cu (red) and C (light green) phase maps. (d) is a zoomed in SEM image of (a) to compare to (e) mixed BPL and commercial CuO nanoparticles.

The OMCs (1D cylindrical FDU-15, 3D hexagonal CMK-3, and 3D bicontinuous CMK-8) were impregnated with CuO (Figure 3.3b-e). The $Cu(NO_3)_2$ precursor solution was able to access the mesopores and form endo-pore CuO nanoparticles since the OMCs have uniform pore size distributions of ~ 3 nm (Table 3.1). CuO impregnation is evidenced by the 2−4 nm particles in alignment with the ordered pore structure, and the absence of CuO particles on the OMC surface (Figure 3.3b-e). The absence of exo-pore particles and the co-alignment of the CuO particles with the carbon pore structure provide strong evidence that the metal oxide is exclusively in the endo-pore. Furthermore, FDU-15 with endo and exo-pore CuO has 2−4 nm endo-pore nanoparticles and 30−50 nm particles on the surface, as shown in the SEM images in Figure 3.3b.

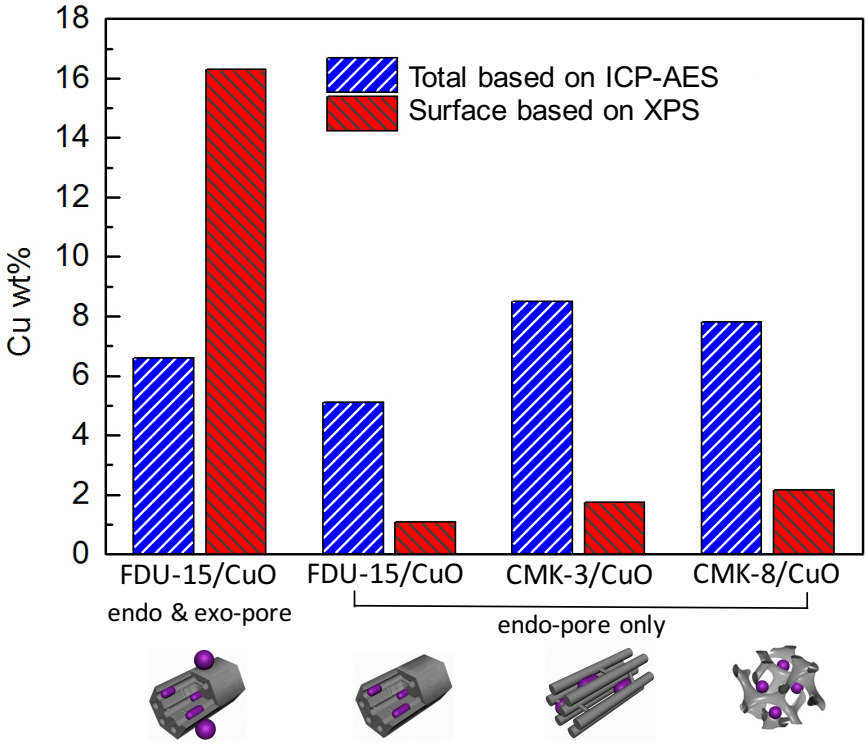

Figure 3.5. Cu wt% calculated using ICP-AES and XPS measurements for OMC/CuO composites.

The CuO location for the OMC/CuO composites was further investigated using XPS to compare with the bulk concentration determined using ICP-AES. Total Cu concentration measured using ICP-AES was 5.2–8.5 wt% for all OMC/CuO composites (Figure 3.5, blue bars). Discrepancies between Cu wt% using XPS and ICP-AES, arises from the surface sensitivity of XPS, which only probes ~10 nm of the sample surface. FDU-15 with endo and exo-pore CuO has 16.2 Cu wt%, which is significantly higher (more than 2x greater) than the bulk analysis (6.6%). The higher Cu wt% is a result of a larger Cu to carbon ratio for XPS measurements (which only measures the carbon surface up to 10 nm depth).

The Cu metal detected (0.5–2.5 wt%) using XPS for carbons with endo-pore CuO (FDU-15/CuO, CMK-3/CuO, and CMK-8/CuO) is significantly lower than the bulk analysis (5.2–8.7 Cu wt%), indicating that the Cu concentration is more localized in the center of the carbon support beyond the XPS range. The Cu wt% reported using XPS (0.5–2.5) is presumably located in the pores within 10 nm of the surface (Figure 3.5, red bars). These results are in good agreement with the TEM/SEM/SEX studies.

3.3.1.2 Structural Properties of Carbon/CuO Composites

The pore volume and surface area of the carbons were affected by CuO impregnation, however the pore sizes remained unchanged, apart from FDU-15 (Figure 3.6 and 3.7b). In general, the pore volume decreased due to CuO endo-pore impregnation, while the surface area increased from exo-pore deposition (Table 3.1).

The measured OMCs, FDU-15, CMK-3, and CMK-8, have similar mesopore sizes of 2.8–3.6 nm, in comparison to microporous BPL with pore sizes less than 1.7 nm. The detailed porosity parameters for CuO impregnated BPL, FDU-15, CMK-3, CMK-8, and their respective unimpregnated counterparts, are presented in Table 3.1. These data are in good agreement with the pore sizes observed from the TEM images in Chapter 2, and previous studies in the literature.[19-21] TEM and BET analysis showed that the pore sizes remained unchanged with CuO impregnation (apart from FDU-15), which is consistent with

the BJH pore size distribution curves shown in Figure 3.6 and 3.7b. The pore volume either remained the same or decreased after impregnation, which agrees with the literature.[70, 94, 199] The pore volume decreased by 16% for 1D cylindrical FDU-15 with endo-pore CuO, most likely due to decreased access to the internal pores after impregnation. The pore volume remained unchanged for the more accessible 3D bicontinuous CMK-8 architecture after CuO loading. The pore volume of BPL/CuO also did not change relative to native BPL, which we attribute to the absence of CuO impregnants within the micropores. However, the BPL/CuO surface area increases by 8%, from 1229 $m^2 g^{-1}$ to 1300 $m^2 g^{-1}$, after the addition of exo-pore CuO particles.

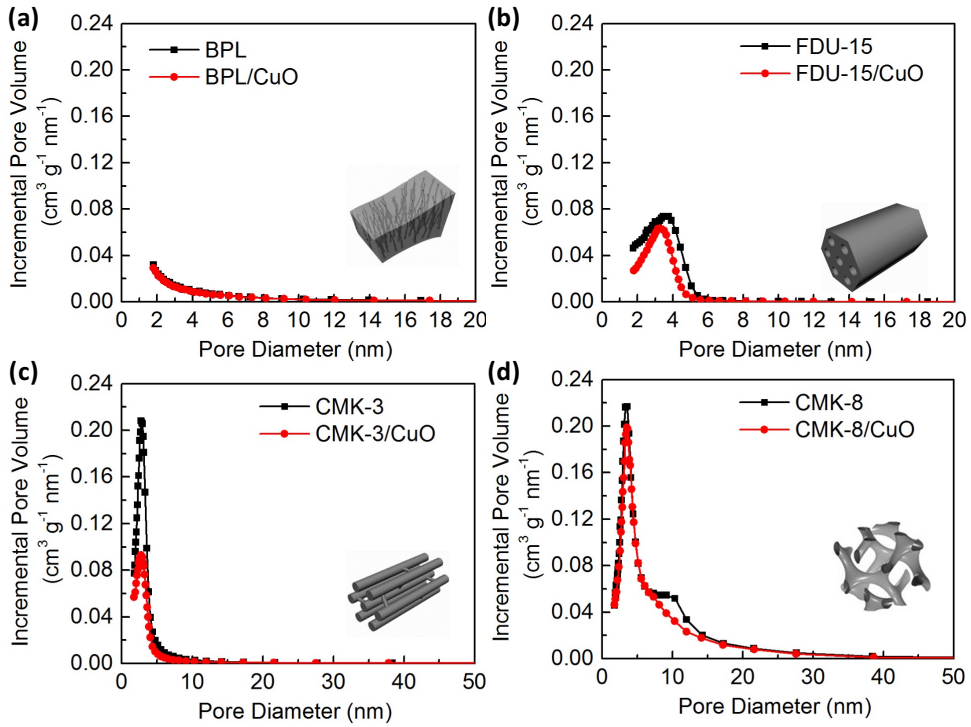

Figure 3.6. BJH pore size distributions to compare the bare carbons and the carbon/CuO composites: (a) BPL, BPL/CuO, (b) FDU-15, FDU-15/CuO, (c) CMK-3, CMK-3/CuO, and (d) CMK-8, CMK-8/CuO.

Table 3.1. N_2 Adsorption–Desorption Properties of Unimpregnated and CuO Loaded Carbons

Carbon Sample	Pore Diameter (nm)[a]	Total pore volume ($cm^3\ g^{-1}$)[b]	Total Surface Area ($m^2\ g^{-1}$)[c]
BPL	<1.7	0.39	1229
BPL/CuO (exo-pore)	<1.7	0.39	1330[d]
FDU-15	3.6	0.32	600
FDU-15/CuO (endo and exo-pore)	3.3	0.32[d]	760[d]
FDU-15/CuO (endo-pore)	3.3	0.27[d]	591[d]
CMK-3	2.8	0.45	976
CMK-3/CuO (endo-pore)	2.8	0.38[d]	935[d]
CMK-8	3.5	1.14	1075
CMK-8/CuO (endo-pore)	3.5	1.15[d]	1246[d]
CuO nanoparticles			82

[a]Calculated using the Barrett-Joyner-Halenda (BJH) model.

[b]The total pore volume is based on the sum of the mesopore and macropore volume from the BJH model and the micropore volume from the t-plot method.

[c]Calculated using the multipoint Brunauer-Emmett-Teller (BET) method.

[d]Values were corrected for the additional weight due to CuO loading (wt% listed in Table 4.2) by normalizing measurements to carbon weight only.

3.3.1.3 Determination of Cu Oxidation State and CuO Loading

ICP-AES and XRD indicate a 6.4−10 wt% loading of Cu(II) oxide on the carbon/CuO samples. For endo and exo-pore impregnated CuO on FDU-15, 55% of the CuO nanoparticles are located endo-pore, while 45% is formed exo-pore (listed in Table 3.2). ICP-AES measurements were taken before and after the selective removal of exo-pore CuO, previously described in Section 3.2.3.2. Quantitative elemental analysis for all carbon/CuO composites were determined using ICP-AES, and presented in Table 3.2. X-ray diffraction showed that the CuO is crystalline and adopts a monoclinic structure (Figure 3.8 and 3.9). In addition, the wider diffraction peaks observed in the XRD spectra are consistent with 2−4 nm CuO nanoparticles observed in the TEM studies.

Table 3.2. Weight % Loading of CuO Impregnated Carbons

	CuO Weight %
BPL/CuO (exo-pore)	10.0
FDU-15/CuO (endo and exo-pore)	8.3 (total) 4.6 (endo-pore) 3.7 (exo-pore)
FDU-15/CuO (endo-pore)	6.4
CMK-3/CuO (endo-pore)	10.6
CMK-8/CuO (endo-pore)	9.8

Intensities were measured using ICP-AES at 327.396 nm for Cu.

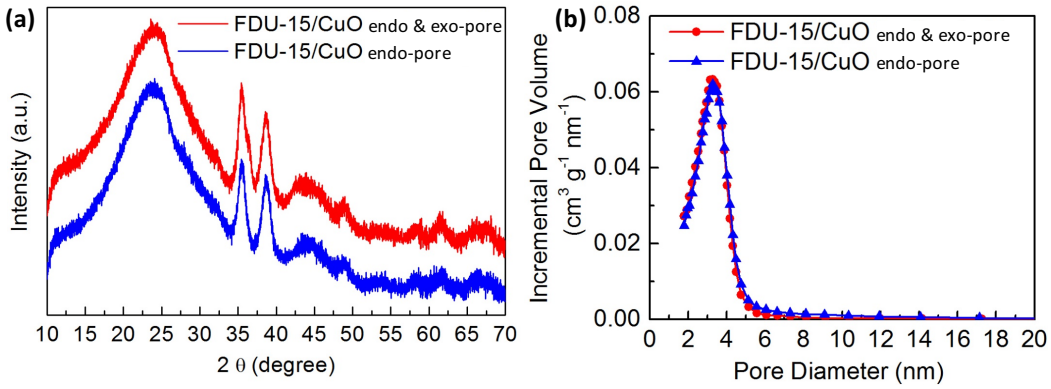

Figure 3.7. (a) XRD diffraction patterns and (b) BJH pore size distributions of endo and exo-pore (red) and endo-pore only CuO impregnated FDU-15 (blue).

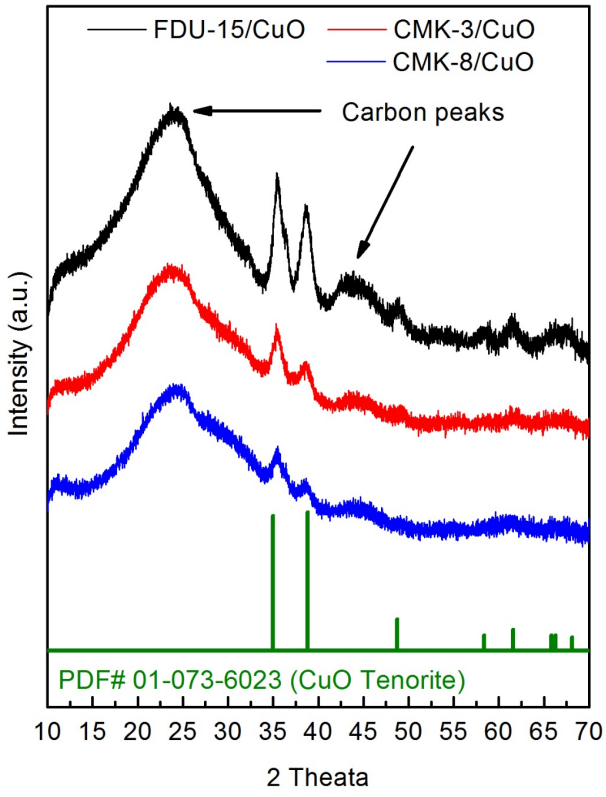

Figure 3.8. C2-XRD diffraction pattern of FDU-15/CuO (black), CMK-3/CuO (red), and CMK-8/CuO (blue) composites. The peaks correspond to carbon and CuO Tenorite (PDF 01-073-6023).

3.3.2 DMMP Adsorption Properties

TPD experiments were conducted to determine the DMMP adsorption and decomposition activity on carbon/CuO composites. Samples were evaluated after 70 h of DMMP exposure to probe the adsorption regime between full surface coverage and liquid saturation. It is well-known that a linear relationship exists between effective adsorption capacities and total surface area for unimpregnated cabons[6] in the absence of chemisorption processes.[203, 204] DMMP adsorption on carbon/CuO composites deviate from strictly surface area dependence, due to the additional effects of CuO located endo and/or exo-pore. Our studies suggest that CuO nanoparticles provide additional active sites for chemisorption, which results in greater DMMP adsorption capacity and decomposition. Generally, the carbon/CuO composites have higher (up to 64%) decomposed and desorbed DMMP capacity, in comparison to their unimpregnated carbon counterparts (Figure 3.9 and Table 3.3). Multiple factors contribute to this observation and will be discussed in depth in the subsequent sections.

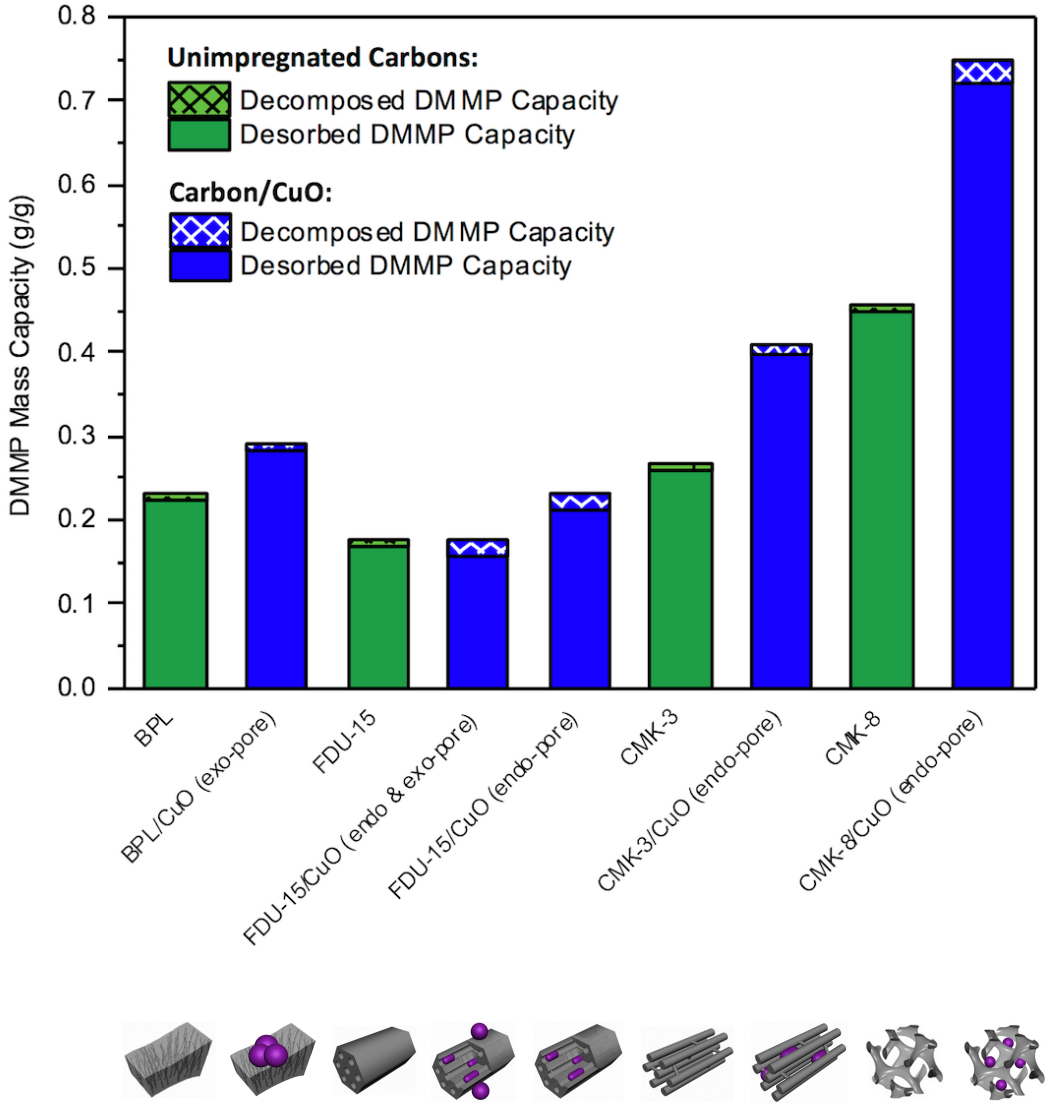

Figure 3.9. Graphical representation of desorbed DMMP (solid bars) and decomposed DMMP (crisscross bars) after TPD experiments with the unimpregnated carbons (green) and carbon/CuO composites (blue) after 70 h of DMMP exposure.

Table 3.3. 70 h Mass Capacity of Decomposed DMMP, Desorbed DMMP, and Total Mass Capacity for Unimpregnated Carbons and Carbon/CuO Composites

Carbon Sample	Decomposed DMMP (g/g)[a,b]	Desorbed DMMP (g/g)[b]	Total Mass Capacity (g/g)[b]
BPL	0.0067	0.2237	0.2304
BPL/CuO (exo-pore)	0.0079	0.2838	0.2917
FDU-15	0.0079	0.1697	0.1776
FDU-15/CuO (endo & exo-pore)	0.0188	0.1572	0.1760
FDU-15/CuO (endo-pore)	0.0180	0.2134	0.2314
CMK-3	0.0051	0.2607	0.2658
CMK-3/CuO (endo-pore)	0.0133	0.3977	0.4110
CMK-8	0.0065	0.4489	0.4554
CMK-8/CuO (endo-pore)	0.0279	0.7201	0.7480
CuO Nanoparticles	0.0005	0.0078	0.0083

[a]Decomposed DMMP was calculated by applying a conversion factor for the mole ratio of DMMP to methanol from Table 3.4.

[b]Measurements reported for the carbon/CuO composites were calculated after disregarding the CuO weight for a more accurate comparison to the unimpregnated carbon samples.

3.3.3 DMMP Decomposition Activity

A few research groups have observed extensive decomposition of DMMP on copper surfaces.[31, 205] Trotochaud *et al.* used *in situ* ambient pressure X-ray photoelectron (APXPS) and infrared spectroscopies, to observe DMMP bond cleavages of PO-CH_3, P-OCH_3, and P-CH_3 at room temperature, consequently forming methoxy groups on the CuO surface (Figure 4.10).[31] Ma *et al*. used mass spectrometry and XPS to observe gaseous H_2, methane, methyl, formaldehyde, methanol, and molecular DMMP, as well as, atomic carbon, phosphorus, and PO_x, on Cu films and clusters surfaces, after DMMP thermal decomposition.[205] These studies and additional investigations of DMMP decomposition on other metal oxide surfaces (TiO_2,[2, 24, 26, 30] MgO,[8, 16, 35-37] LaO,[16] Al_2O_3,[16, 17, 23, 25, 34, 38, 39] Fe_2O_3,[14, 16]), suggest that DMMP decomposes to surface phosphate, alkoxide, and alkyl groups, while forming gaseous byproducts, such as carbon dioxide, carbon monoxide, dimethyl ether, formaldehyde, formic acid, and more commonly, methanol.

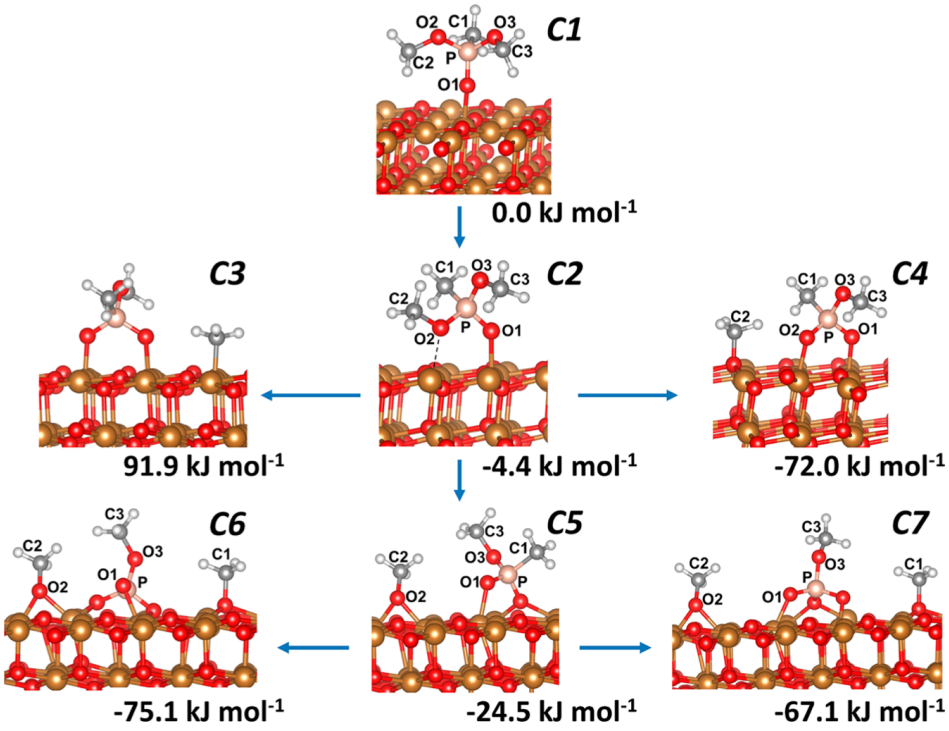

Figure 3.10. Proposed pathways for DMMP decomposition on CuO surface. Taken from Reference 31.

3.3.3.1 Determination of DMMP Conversion to Methanol (MeOH)

Decomposition of DMMP on carbon/CuO substrates generates one mole of MeOH for each mole of DMMP that decomposes. This conclusion was determined from a combination of quantitative ^{1}H-NMR and ICP-AES measurements. The evolution of gas-phase products, predominantly methanol with trace amounts of formaldehyde, was measured using a method described in Section 3.2.6−3.2.7. No phosphorus-containing products other than molecular DMMP were detected, which agrees with previous observations in the literature.[24] The phosphorus content remaining on the carbon/CuO adsorbents after DMMP

decomposition were quantitatively evaluated using ICP-AES after the TPD experiments. These experiments indicate that the amount of phosphorus (mg P/g material) observed agrees with the expected amount of phosphorus, which was calculated with the assumption that each mole of DMMP produces a mole of gaseous MeOH (Table 3.4).

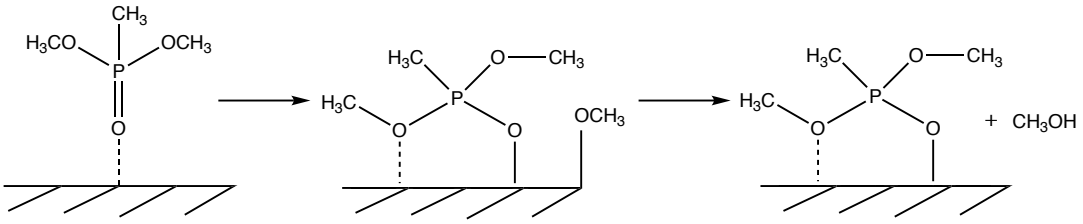

Figure 3.11. Illustration of DMMP decomposition to produce gaseous methanol (CH_3OH) and surface-bound methyl methylphosphonate (MMP).

Table 3.4. Phosphorus Concentration of Cycled Samples

	FDU-15	**FDU-15/CuO (endo & exo-pore)**
Observed[a,b] mg P/g material	2.22	3.13
Equivalent Amount of DMMP	1.02	0.98

[a]Observed value for FDU-15 was measured using ICP-AES at 177.5 nm for P.

[a]Observed value for FDU-15/CuO (endo & exo-pore) was measured using ICP-AES at 178.2 nm for P.

3.3.3.2 Thermal Decomposition of DMMP

As described above, the methanol liberated in the TPD experiments can be used as a quantitative indicator of DMMP decomposition capacity. We speculate that the methanol produced on the inert carbon surface is caused by thermal decomposition, due to high operating temperatures (up to 450 °C) in our TPD experiments. Methanol production from unimpregnated FDU-15 was measured at multiple exposure times, and compared to FDU/CuO composites to differentiate between the amount of methanol produced from thermal decomposition or reactive decomposition with the CuO surface. The results showed that the decomposed DMMP capacity for bare FDU-15 was consistently between 0.007−0.008 g DMMP/g FDU-15, regardless of the length of DMMP exposure (Figure 3.12). Specifically, the extent of decomposition (*i.e.* decomposed DMMP capacity) for the bare FDU-15 after 70 h of DMMP exposure is 0.008 g DMMP/g FDU-15, whereas both FDU-15/CuO composites have a decomposed DMMP capacity over 125% higher (0.018−0.019 g DMMP/g FDU-15). We speculate that the 0.010−0.011 g DMMP/g FDU-15 difference is due to the DMMP decomposition activity on the CuO surface. The decomposed DMMP capacities listed in Table 3.5 neglect the methanol produced from thermal decomposition to more accurately assess CuO effects on DMMP adsorption and decomposition, in comparison to the other samples shown graphically in Figure 3.13.

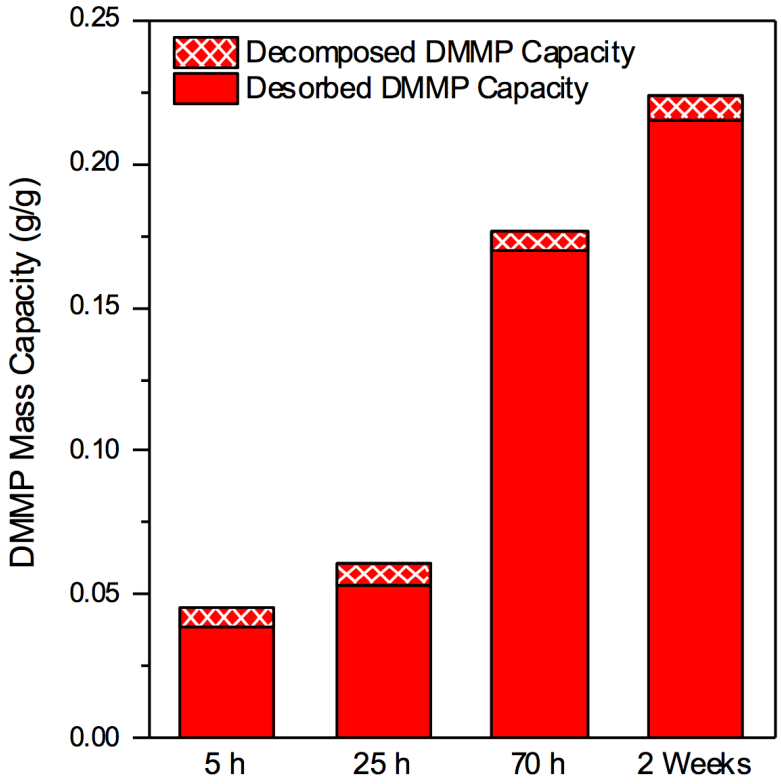

Figure 3.12. Graphical representation of desorbed DMMP (solid bars) and decomposed DMMP (crisscross bars) after multiple TPD experiments with FDU-15 after 5 h, 25 h, 70 h, and 2 weeks of DMMP exposure.

Table 3.5. 70 h Mass Capacity of Decomposed DMMP Not Including Methanol Production from Thermal Decomposition, Desorbed DMMP, and Total Mass Capacity for Unimpregnated Carbons and Carbon/CuO Composites

Carbon/CuO	Decomposed DMMP (g/g)[a,b]	Desorbed DMMP (g/g)[b]	Total Mass Capacity (g/g)[b]
BPL/CuO (exo-pore)	0.0012	0.2838	0.2850
FDU-15/CuO (endo & exo-pore)	0.0109	0.1572	0.1681
FDU-15/CuO (endo-pore)	0.0101	0.2134	0.2235
CMK-3/CuO (endo-pore)	0.0082	0.3977	0.4059
CMK-8/CuO (endo-pore)	0.0214	0.7201	0.7415

[a]Decomposed DMMP was calculated by applying a conversion factor for the mole ratio of DMMP to methanol from Table 3.4.

[b]Measurements reported for the carbon/CuO composites were calculated after disregarding the CuO weight for a more accurate comparison to the unimpregnated carbon samples.

Figure 3.13 summarizes the DMMP desorbed and decomposed capacity for OMCs and the CuO impregnated OMCs. In general, the carbon/CuO composites (blue bars) achieve higher desorbed and decomposed capacity than their unimpregnated carbon counterparts (green bars), as shown in Figure 3.12. While

their pore properties are relatively similar (Table 3.1), the CuO impregnants improve DMMP adsorption and decomposition due to stronger binding and higher surface reactivity.

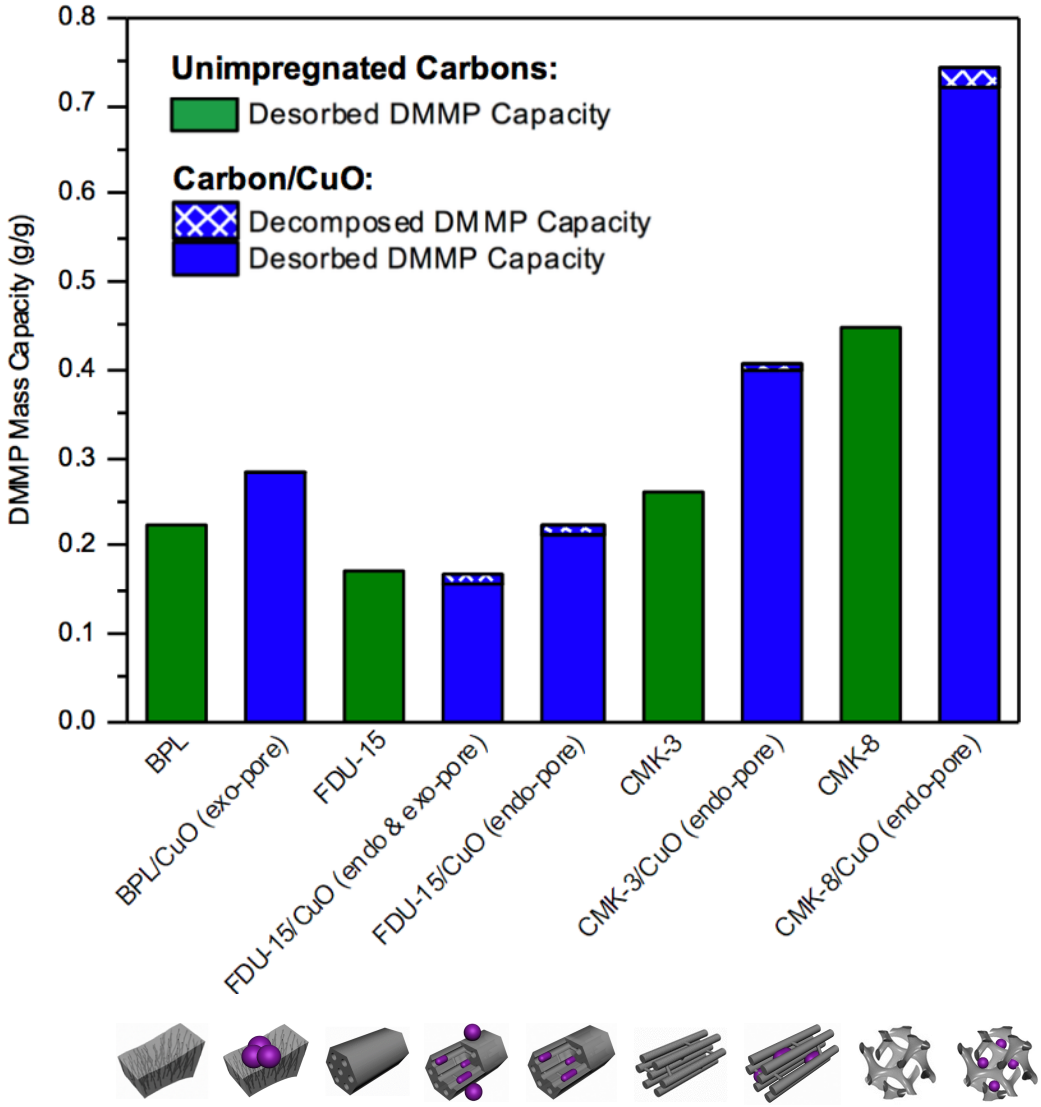

Figure 3.13. Graphical representation of desorbed DMMP (solid bars) and decomposed DMMP (crisscross bars) after a TPD experiment with the different unimpregnated (green) and CuO loaded carbons (blue) after approximately 70 h of DMMP exposure.

3.3.3.3 Surface Reactivity Comparison for CuO and Carbon

The experiments above show that the CuO surface reactivity is significantly higher in comparison to the carbons, resulting in greater DMMP adsorption and decomposition. The adsorption properties of CuO nanoparticles, BPL, FDU-15, CMK-3, and CMK-8, were studied at low surface coverages (*i.e.* after 5 h of DMMP exposure) to reveal the differences in surface reactivity. Desorbed and decomposed DMMP capacities were measured after 5 h of DMMP exposure, and normalized by their surface area (Figure 3.13, Table 3.6). The CuO surface activity (total DMMP area capacity) was over 3.5 times higher in comparison to the OMCs (0.075−0.078 m^2 g^{-1}), and 17 times higher than BPL (0.016 m^2 g^{-1}). The significantly higher CuO reactivity observed could explain the increase in decomposed and desorbed capacities for the carbon/CuO composites, in comparison to their unimpregnated counterparts. The chemisorbed DMMP molecules can react with the CuO impregnants, ultimately resulting in the observed increase in adsorption potential and decomposition, which agrees with previous observations made by Saxena *et al*.[69]

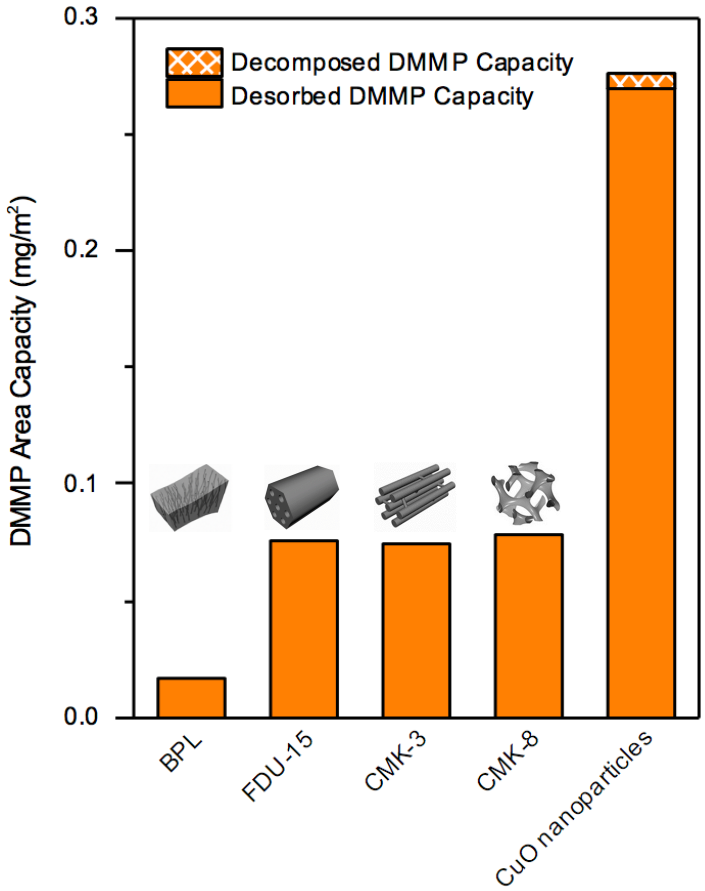

Figure 3.14. Graphical representation of desorbed DMMP (solid bars) and decomposed DMMP (crisscross bars) after a TPD experiment with BPL, FDU-15, CMK-3, CMK-8, and CuO nanoparticles after 5 h of DMMP exposure.

Table 3.6. 5 h Area Capacity of Decomposed DMMP, Desorbed DMMP, and Total Area Capacity for the Carbons and CuO Nanoparticles

Carbon Sample	Decomposed DMMP (g m^{-2})[a]	Desorbed DMMP (g m^{-2})	Total Area Capacity (mg m^{-2})
BPL		0.016	
FDU-15		0.076	
CMK-3		0.074	
CMK-8		0.078	
CuO nanoparticles	0.007	0.269	0.276

3.3.3.4 Effect of CuO Size and Location on DMMP Decomposition

The size and location of CuO nanoparticles affect the adsorption and decomposition of DMMP on carbon/CuO composites with similar loading levels. The highest decomposition activity was observed for the smaller endo-pore CuO nanoparticles with larger surface area, and more reactive sites. During the impregnation process, pore constrictions resulted in smaller CuO nanoparticles formed inside the pores. The DMMP decomposition capacity per g CuO (wt%) for endo-pore and exo-pore CuO were compared to probe the effects of CuO size and location on DMMP decomposition.

The smaller CuO nanoparticles (2−4 nm) located within the endo-pores showed the highest DMMP decomposition capacity per g CuO (1.58 mg DMMP/g material). The DMMP decomposition capacity for the exo-pore CuO nanoparticles (30−50 nm) supported on FDU-15, per CuO wt% decreases by 38% (0.98 mg DMMP/g material). For the larger CuO particles, such as the aggregates on the BPL surface, the DMMP decomposition capacity was significantly lower, 0.12 mg DMMP/g material per g CuO (Table 3.7). These results suggest that the smaller endo-pore CuO nanoparticles are more reactive, resulting in higher DMMP decomposition in comparison to larger exo-pore CuO particles.

Table 3.7. DMMP Decomposition Capacity (mg g^{-1}) per g CuO (wt%)

	Endo-pore CuO Decomposition Activity (mg g^{-1})	Exo-pore CuO Decomposition Activity (mg g^{-1})
FDU-15/CuO (endo-pore)	1.58	0.00
FDU-15/CuO (endo & exo-pore)	1.58	0.98
BPL/CuO (exo-pore)	0.00	0.12

3.3.3.5 Significance of Structural Effects

The 3D architecture of CMK-3 and CMK-8 allows for higher DMMP decomposition and adsorption into the more accessible structure in comparison to 1D FDU-15, after CuO impregnation. The higher DMMP decomposition is a result of the more accessible CuO reactive sites in CMK-3 and CMK-8. These studies suggest that all the carbon/CuO samples show higher DMMP adsorption, apart from the CuO endo and exo-pore impregnated FDU-15 (Figure 3.13). The CuO exo-pore impregnants blocked access into the internal pores (Figure 3.15). This blockage limits DMMP diffusion through the 1D architecture of the FDU-15 pores, resulting in lower DMMP adsorption after 70 h of DMMP exposure.

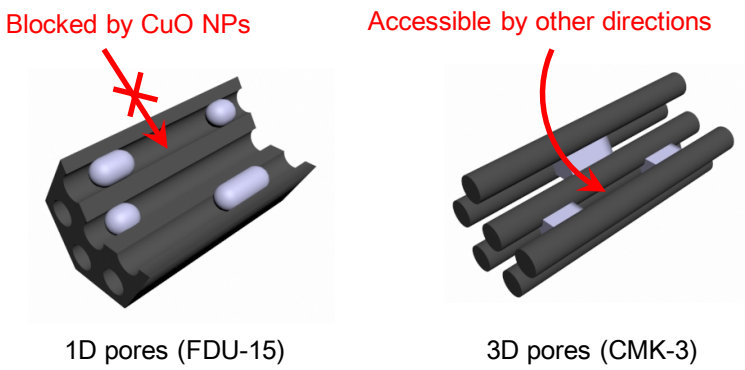

Figure 3.15. Representation of the limited diffusion of DMMP into the CuO loaded 1D pores of FDU-15, in comparison to the more accessible 3D pores of CMK-3 and CMK-8.

CMK-8/CuO achieved the highest DMMP adsorption and decomposition in comparison to the other carbon/CuO samples (Table 3.5). Given that the CuO loading amount and impregnation process was similar for all the samples, the difference in adsorption/decomposition activity is linked to the differences in the CuO size, location, and 3D architecture of CMK-8. The more reactive, smaller, endo-pore CuO nanoparticles are more accessible within CMK-8, in comparison to the other carbon/CuO systems. While CMK-3 also possesses 3D pores, its CuO impregnants are larger than the CuO nanoparticles that reside in CMK-8 (Figure 3.4). The smaller CuO nanoparticles in CMK-8 have higher surface area for greater reactivity. In addition to the advantages of a 3D pore architecture and nano-sized CuO impregnants, CMK-8/CuO has the largest pore volume, allowing for higher DMMP uptake after extended periods of exposure time (Table 3.5). These factors result in an increase in the performance of CMK-8/CuO for DMMP removal relative to the other systems.

3.4 CONCLUSIONS

At 70 h of DMMP exposure, our studies show that CMK-8/CuO is the best system for DMMP removal. The nano sized endo-pore CuO in CMK-8 was the most reactive material for DMMP decomposition, in comparison to the other carbon/CuO composites with similar CuO loading. The 3D pore architecture and large pore volume also allowed for easy accessibility and higher DMMP adsorption capacity. These findings are important factors that influence the effectiveness of DMMP removal from the airstream.

During our investigation, we observed multiple limitations to the inferior performing carbon/CuO composite, FDU-15 with endo and exo-pore CuO. Our studies suggest that FDU-15/CuO exo-pore impregnants occupy the mesopores and block internal surface sites, consequently decreasing the adsorption potential. Due to these complications, there is a need for a new, more effective absorbents with high surface area, and abundant reactive surfaces. In our next chapter, we will explore mesoporous metal oxides as more effective adsorbents for CWA defeat.

Chapter 4: Dimethyl Methylphosphonate Adsorption Properties and Decomposition Activity on Mesoporous Metal Oxides

4.1 INTRODUCTION

Advancements in gas mask filtration devices heavily rely on our understanding of CWA adsorption and decomposition mechanisms (described in Chapter 1), and how adsorbent properties affect their performance (revealed in Chapter 2 and 3). The investigation of ASZM-TEDA revealed the advantages of key design features and the disadvantages that hinder their functionality. These findings can guide us in the synthesis of new, superior filters.

Our research efforts have revealed the significance of the carbon adsorbents in Chapter 2. The large surface area (600−1300 m^2 g^{-1}) and pore volumes (0.2−1.2 cm^3 g^{-1}) allow for high DMMP adsorption capacities (up to 1.2 cm^3 DMMP/g carbon). After increasing the pore uniformity from the disordered BPL carbon to the ordered mesoporous carbon, stronger binding to the carbon surface is achieved, as demonstrated by the higher DMMP desorption energies (30−40% increase). However, this binding is still characterized as physisorption and is relatively weak in comparison to interactions with metal oxide impregnants. Therefore, due to the weak bonding and inert carbon surface, there is little to no DMMP decomposition observed.

For carbon/CuO composites investigated in Chapter 3, the DMMP mass adsorption capacity was increased up to 64% in comparison to their unimpregnated counterparts, apart from 1D cylindrical FDU-15 with CuO endo and exo-pore. The exo-pore CuO is believed to decrease the adsorbent performance by blocking internal adsorption sites after metal oxide deposition. In addition, the endo-pore CuO decreased the pore volume up to 18%, which consequently, lowers the adsorption capacity for extended periods of DMMP exposure. Due to these disadvantages and additional shortcomings, such as low breathability and deactivation from surface poisoning on the carbon-based adsorbents,[88, 206, 207] there is a need for more effective, catalytic adsorbents with high surface areas, and more reactive adsorption sites.[203, 208, 209]

In this chapter, ordered mesoporous metal oxides (OMM) are synthesized with 1D cylindrical and 3D hexagonal architectures with more reactive sites, and designed to presumably have better mass transfer into the pores in comparison to impregnated carbons. Additionally, the OMMs have a higher surface area and pore volume in comparison to metal oxide nanoparticles, for greater adsorption and decomposition of DMMP. We describe the extent of DMMP removal for the OMMs: alumina (Al_2O_3), titania (TiO_2), ceria (CeO_2), iron oxide (Fe_2O_3), and aerogel-Fe_2O_3 in comparison to FDU-15/CuO (endo and exo-pore), FDU-15, and BPL, using TPD/quantitative ^{1}H-NMR and ICP-AES bulk analysis. Additional

surface chemistry insight was provided by our collaborators using infrared spectroscopy and a theoretical approach.

4.2 EXPERIMENTAL SECTION

4.2.1 Materials

AR grade DMMP (≥97.0%) and metal precursors ($Al(NO_3)_3 \cdot 9H_2O$, $Ti(OBu)_4$, $Ce(NO_3)_2$, $Fe(NO_3)_3$) were purchased from Sigma Aldrich (USA) and used without further purification.

4.2.2 Mesoporous Metal Oxides

The mesoporous metal oxides, Al_2O_3, TiO_2, CeO_2, Fe_2O_3, and aerogel Fe_2O_3 were successfully synthesized by a soft template (Figure 4.1), hard template (Figure 4.2), and sol-gel method (Figure 4.3). The OMMs, Al_2O_3 and TiO_2, were prepared by myself and Dr. Junkai Hu, respectively, using slight modifications of methods described in the literature.[210-212] The OMMs, CeO_2 and Fe_2O_3, were synthesized by a different method developed by Dr. Junkai Hu. Fe_2O_3 aerogels were prepared by our collaborators at the Naval Research Laboratory (NRL), Dr. Jeffrey Long, using slight modifications of methods previously published in the literature.[213-215]

4.2.2.1 Synthesis of Mesoporous Alumina (meso-Al_2O_3)

Meso-Al_2O_3 was synthesized by a soft template method described by Wang *et al.*[210] In a typical reaction, 5.6 g of $Al(NO_3)_3 \cdot 9H_2O$ was dissolved in a solution of anhydrous ethanol and deionized water (15 mL), with the ratio of $\frac{V_{EtOH}}{V_{Water}} = \frac{4}{1}$. Then the mixture was transferred to a petri dish without cover for the solvothermal pre-hydrolysis treatment, where the sample was dried at 80 °C for 5 h. The Al-OH solid was slowly added to a solution containing 1.8 g of P123 (diblock copolymer, $EO_{20}PO_{70}EO_{20}$, where EO = ethylene oxide, PO = propylene oxide) and 0.6 g of citric acid, dissolved in anhydrous ethanol (30 mL). After vigorous stirring for 24 h at 30 °C, the resultant mixture was transferred to a petri dish, and dried at 45 °C for 48 h. The resulting solid was then dried at 100 °C for 24 h in a box furnace. The final product was calcined at 400 °C under O_2 for 5 h to remove the template and the citric acid.

4.2.2.2 Synthesis of Mesoporous Titania (meso-TiO_2)

Meso-TiO_2 was synthesized by a soft template method described by Fan *et al.*[211] and Brinker *et al.*[212] In a typical reaction, 10 mmol of $Ti(OBu)_4$, 40 mmol of acetic acid, 24 mmol of HCl, and 1.6 g of F127 (triblock copolymer, $EO_{96}PO_{70}EO_{96}$, where EO = ethylene oxide, PO = propylene oxide) were dissolved in ethanol (30 mL). After vigorous stirring for 1 h at 30 °C, the resultant mixture was transferred to a petri dish, and dried at 40 °C for 12 h. The resulting

solid was then heated at 65 °C for 24 h in a box furnace. The final product was calcined at 350 °C under O_2 for 5 h to remove the template.

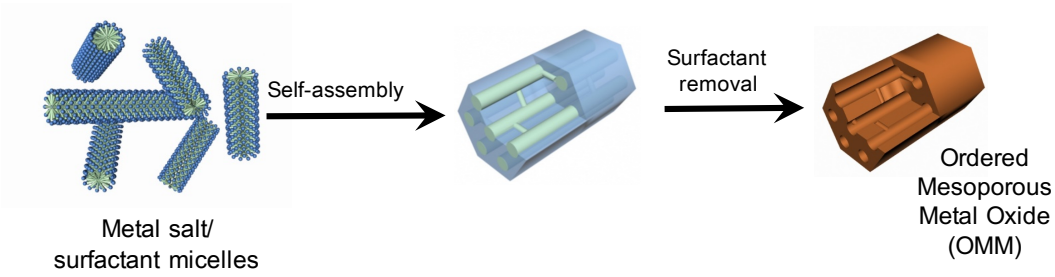

Figure 4.1. Schematic of ordered meso-Al_2O_3/meso-TiO_2 synthesis using a soft template method.

4.2.2.3 Synthesis of Mesoporous Ceria (meso-CeO_2) and Iron Oxide (meso-Fe_2O_3)

Meso-CeO_2 and meso-Fe_2O_3 were synthesized by a hard template method developed by Dr. Junkai Hu. In a typical reaction, 0.2 g of SBA-15 was fully saturated with a metal nitrate solution (50 wt% for $Ce(NO_3)_2$ and 45 wt% for $Fe(NO_3)_3$). Then the excess solution was removed by vacuum filtration. The SBA-15 filled with metal nitrate solution was collected, and dried at 90 ^{o}C overnight, then annealed at 170 °C or 350 °C for Fe_2O_3 and CeO_2, respectively. Next, samples were annealed for 3 h under Ar flow with a heating rate of 1°C min^{-1}. The impregnation process was repeated again, except the 2nd annealing step is 400 °C for 3 h for both Fe_2O_3 and CeO_2. The silica was removed by dissolution with 3M NaOH solution at 50 °C for 1 h, and this process was repeated twice

until the SiO_2 was removed, and confirmed by SEM/EDX. The meso-CeO_2 or meso-Fe_2O_3 was collected by centrifugation and washed with deionized water. The extraction/washing process was repeated three times.

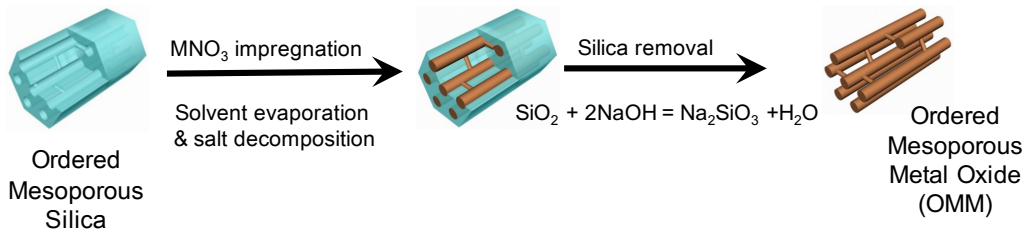

Figure 4.2. Schematic of ordered meso-CeO_2/ meso-Fe_2O_3 synthesis using an ordered mesoporous silica template, SBA-15.

4.2.2.4 Mesoporous Iron Oxide Aerogel (aerogel-Fe_2O_3)

The Fe_2O_3 aerogel was synthesized by Dr. Jeff Long (NRL) according to a published sol-gel method described by Long *et al.*[213] and Gash *et al.*[214, 215]

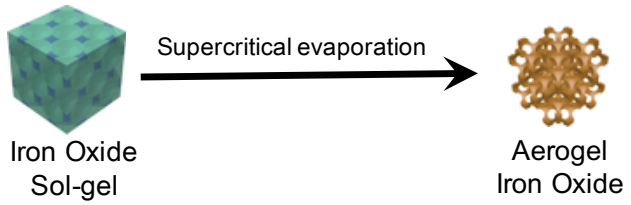

Figure 4.3. Schematic of aerogel-Fe_2O_3 synthesis using a sol-gel method.

4.2.3 Characterization of Mesoporous Metal Oxides

Pore size, volume, and surface area of the mesoporous metal oxides were determined from N_2 adsorption-desorption isotherms recorded with a Micromeritics ASAP 2020 Porosimeter Test Station. Samples were degassed in vacuum at 100 °C for 12 h prior to characterization. The specific surface areas were calculated using the Brunauer-Emmett-Teller (BET) method from the N_2 adsorption data in the relative pressure range (P/P_0) of 0.05−0.20. The general porosity distribution was calculated from the adsorption branch using the Barrett-Joyner-Halenda (BJH) equation.

Structural morphologies of the samples were imaged with a scanning electron microscope (Hitachi SU-70 SEM, operated at an acceleration voltage of 10 kV), and a transmission electron microscope (JEM 2100 Field Emission operated at 200 kV). The samples were dispersed in methanol and a 10 μL aliquot of the resulting dispersion was drop cast on the TEM grids. The TEM grids used were carbon-coated Cu grids (CF200-Cu, Electron Microscopy Sciences). X-ray diffraction (XRD) patterns were recorded by a Bruker Smart1000 (Bruker AXS Inc., USA) using CuKα radiation.

4.2.4 Exposure of Mesoporous Metal Oxides to DMMP

Mesoporous metal oxides were pre-treated at 100 °C for ≥ 6 h under static vacuum to remove any adsorbed contaminants before exposure to DMMP using the vial-in-vial method, modified from the literature.[189] Approximately 75 mg of

material was transferred to small glass vials. Each small glass vial was placed inside a larger vial that contained a sufficient amount of liquid DMMP (200 μL), to saturate the head space of the vial assembly. The larger vial was then capped, and stored in a desiccator. The exposure process was conducted under ambient pressure at room temperature (24−26 °C). The samples were removed after 5 h, and analyzed using a fixed-bed reactor, which is described in Section 4.2.5.

4.2.5 Fixed-Bed Reactor Setup

TPD studies on the samples were conducted using a temperature controlled fixed-bed reactor system. Each sample (75 mg) was loaded into a 10 mm ID quartz reactor. The reactor was composed of a quartz frit with ~10 mg quartz wool layered atop the frit. The sample was placed on top of the wool. After loading the sample into the reactor, the system was sealed with Swagelok fittings, and Ar (Standard, Airgas) was flowed at a constant flow rate of 50 SCCM (standard cubic centimeters per minute). The mass flow was controlled with a Brooks 5850 series mass flow controller. A Eurotherm 91 P PID controller and K-type thermocouple controlled the sample temperature. All lines downstream of the reactor were maintained at a constant 150 °C before and during testing to minimize DMMP adsorption in effluent lines. The effective adsorption capacity measurements were programmed to include the following temperature regimes:

(7) A linear temperature increase of 10 °C min^{-1}, from 30 °C to 450 °C

(8) Hold at 450 °C for 2 min

(9) A fast cooling to 30 °C

The reactor effluent was directed through a bubbler filled with a mixed solution of deuterated acetonitrile (CD_3CN) and ethylene carbonate (EC) that sufficiently submerged the bubbler stem. The CD_3CN/EC solution was maintained at -42 °C via a dry ice/acetonitrile bath. The sample was analyzed using ^{1}H-NMR, which is described in Section 4.2.6.1.

4.2.6 Methods

4.2.6.1 ^{1}H-NMR Study

NMR spectra were recorded using a Bruker AV-400 MHz Spectrometer. For each spectrum, 128 transients were collected at 298 K with an acquisition time of 2.6 s, d1 relaxation time of 4 s. The DMMP-acetonitrile-d^3 solutions were spiked with precise amounts of EC that was added as a quantitative calibrant to measure the amount of DMMP and byproducts desorbed.

4.2.6.2 ICP-AES Study

The phosphorus content of the cycled adsorbent materials were determined using ICP-AES characterization performed on a Perkin Elmer ICP Optima 4700. The samples were dissolved in pure trace-metal grade nitric acid (Sigma-Aldrich) and diluted with milli-Q water to a known volume (100 mL) with a final concentration of 2 wt% nitric acid (HNO_3), before administered to the plasma. Intensities were measured at 178.3 nm for P. A linear calibration curve (R^2 = 0.9999) was collected with five standards, a blank (2 wt% HNO_3), 0.1, 0.2, 0.5, and 1.0 ppm P (High Purity Standard, 1000 μg/g P in 2 wt% HNO_3).

4.2.7.3. FTIR Spectroscopy

Mr. Scott Holdren collected FTIR spectra on a Nicolet cooled MCT-A detectors. A Harrick Scientific Praying Mantis DRA optical accessory was used with an associated Harrick Scientific high temperature reaction chamber HVCDRP-5 for the DRIFTS measurements.

4.2.7.4. DFT Calculations

Dr. Roman Tsyshevsky calculated the adsorption of DMMP on metal oxide surfaces by means of DFT-based modeling. Solid state periodic calculations were performed using hybrid functionals, which include corrections for weak van der Waals interactions and projector augmented-wave (PAW) pseudo-potentials, as implemented in the VASP code as described elsewhere.[216-218]

4.3 RESULTS AND DISCUSSION

4.3.1 Characterization of Mesoporous Metal Oxides

In this investigation, we studied five mesoporous metal oxides, which include four OMMs: Al_2O_3, TiO_2, CeO_2, and Fe_2O_3 with well-defined pore size, volume, and surface area. Disordered mesoporous aerogel Fe_2O_3 was also investigated for comparison. The structures of the OMMs were first investigated by electron microscopy (TEM and SEM) and X-ray diffraction. These characterization techniques verified the ordered pore structure, size, and

crystallinity (or lack thereof) for the OMMs. Figure 4.4 and 4.5, reveals the 1D cylindrical structure of amorphous meso-Al_2O_3 and crystalline rutile/anatase phase meso-TiO_2, respectively. Figure 4.6 and 4.7 shows the 3D hexagonal structure of crystalline cerianite phase meso-CeO_2 and hematite phase meso-Fe_2O_3, respectively. Aerogel-Fe_2O_3 is also hematite phase, however the structure is more disordered with varying pore sizes that are difficult to distinguish (Figure 4.8).

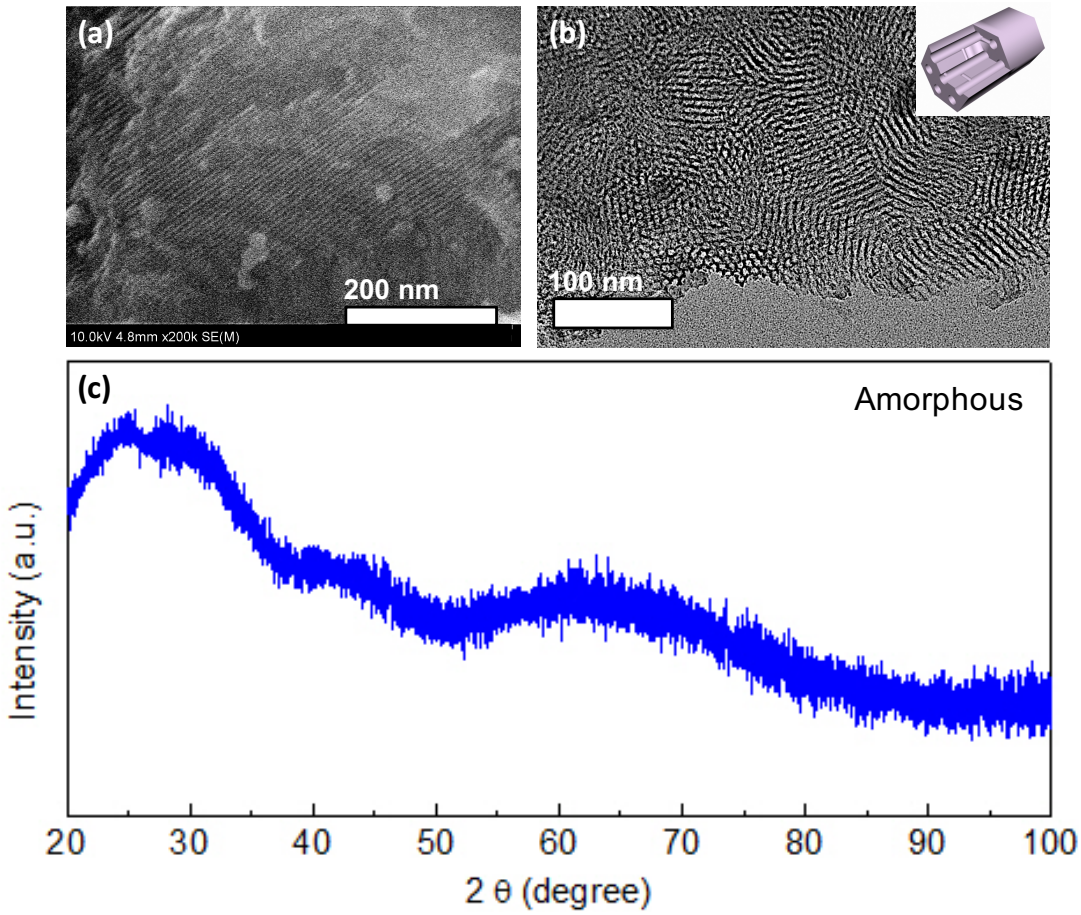

Figure 4.4. (a) SEM image, (b) TEM image, and (c) X-ray diffraction pattern of amorphous meso-Al_2O_3.

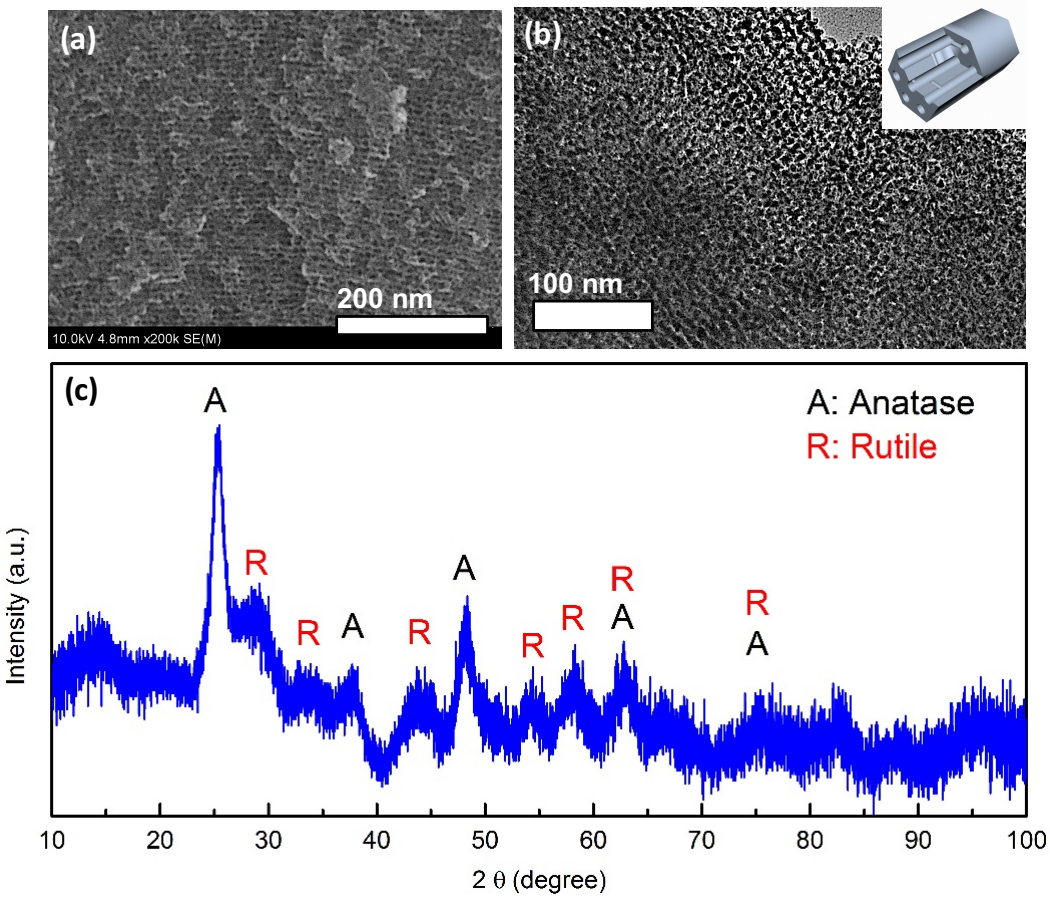

Figure 4.5. (a) SEM image, (b) TEM image, and (c) X-ray diffraction pattern of crystalline anatase and rutile phase meso-TiO_2.

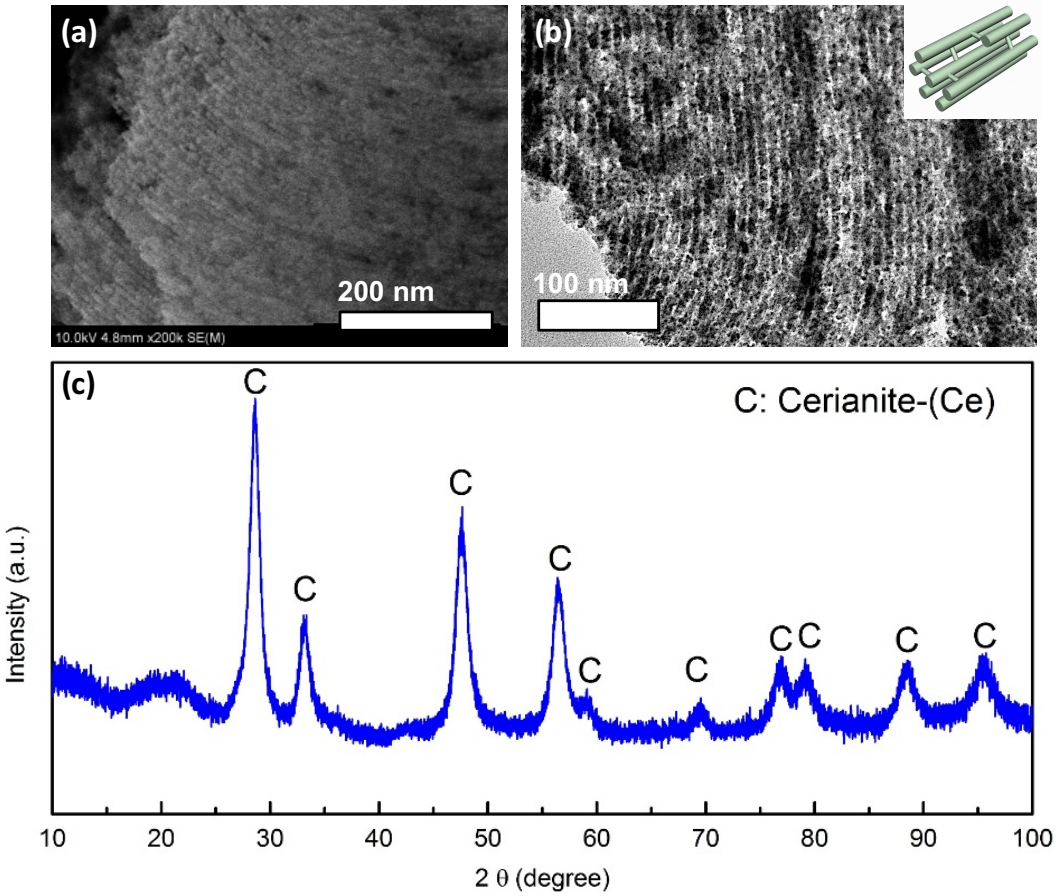

Figure 4.6. (a) SEM image, (b) TEM image, and (c) X-ray diffraction pattern of crystalline cerianite phase meso-CeO_2.

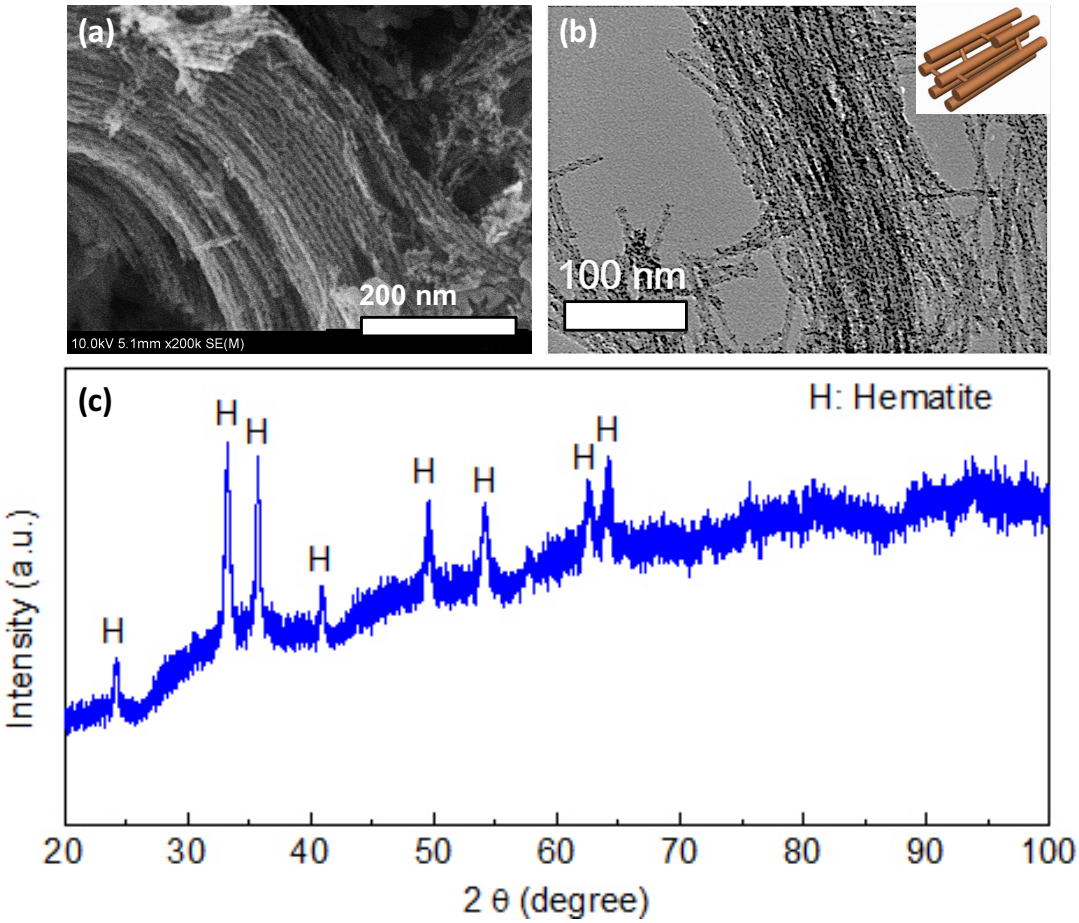

Figure 4.7. (a) SEM image, (b) TEM image, and (c) X-ray diffraction pattern of crystalline hematite phase meso-Fe_2O_3.

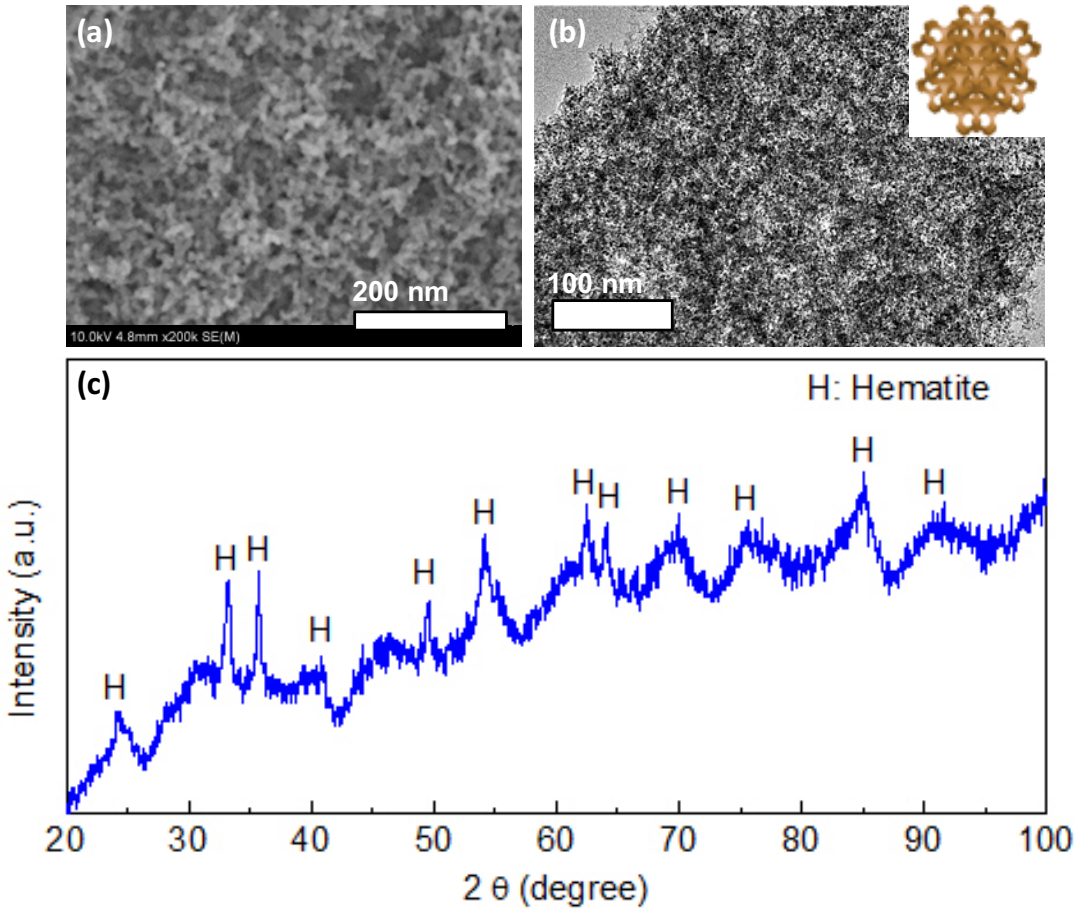

Figure 4.8. (a) SEM image, (b) TEM image, and (c) X-ray diffraction pattern of crystalline hematite phase aerogel-Fe_2O_3.

The OMMs and OMCs with similar architectures have different pore properties, such as the surface area, pore size, and volume, which are compared in Figure 4.9. Meso-Al_2O_3 and meso-TiO_2 were synthesized by a soft template method, similar to the 1-D cylindrical FDU-15. The comparisons between meso-Al_2O_3, meso-TiO_2, and FDU-15, reveal larger pore sizes (7.2 and 5.1 nm, respectively) in comparison to FDU-15 (3.6 nm) (Figure 4.9a). Meso-CeO_2 and meso-Fe_2O_3 were synthesized by a hard template method, similar to 3D hexagonal

CMK-3. The comparisons between their pore size distributions are shown in Figure 4.9b, revealing a larger average pore size of 4.4 nm for meso-Fe_2O_3, but similar sizes for meso-CeO_2 and CMK-3 (2.5 and 2.7 nm, respectively). On the other hand, aerogel-Fe_2O_3 has a wide range of pore sizes, which are much larger than any of the OMMs (Figure 4.10). The detailed structure parameters are listed in Table 4.1. These data are in good agreement with our TEM results and previous studies in the literature.[184-186, 210-215]

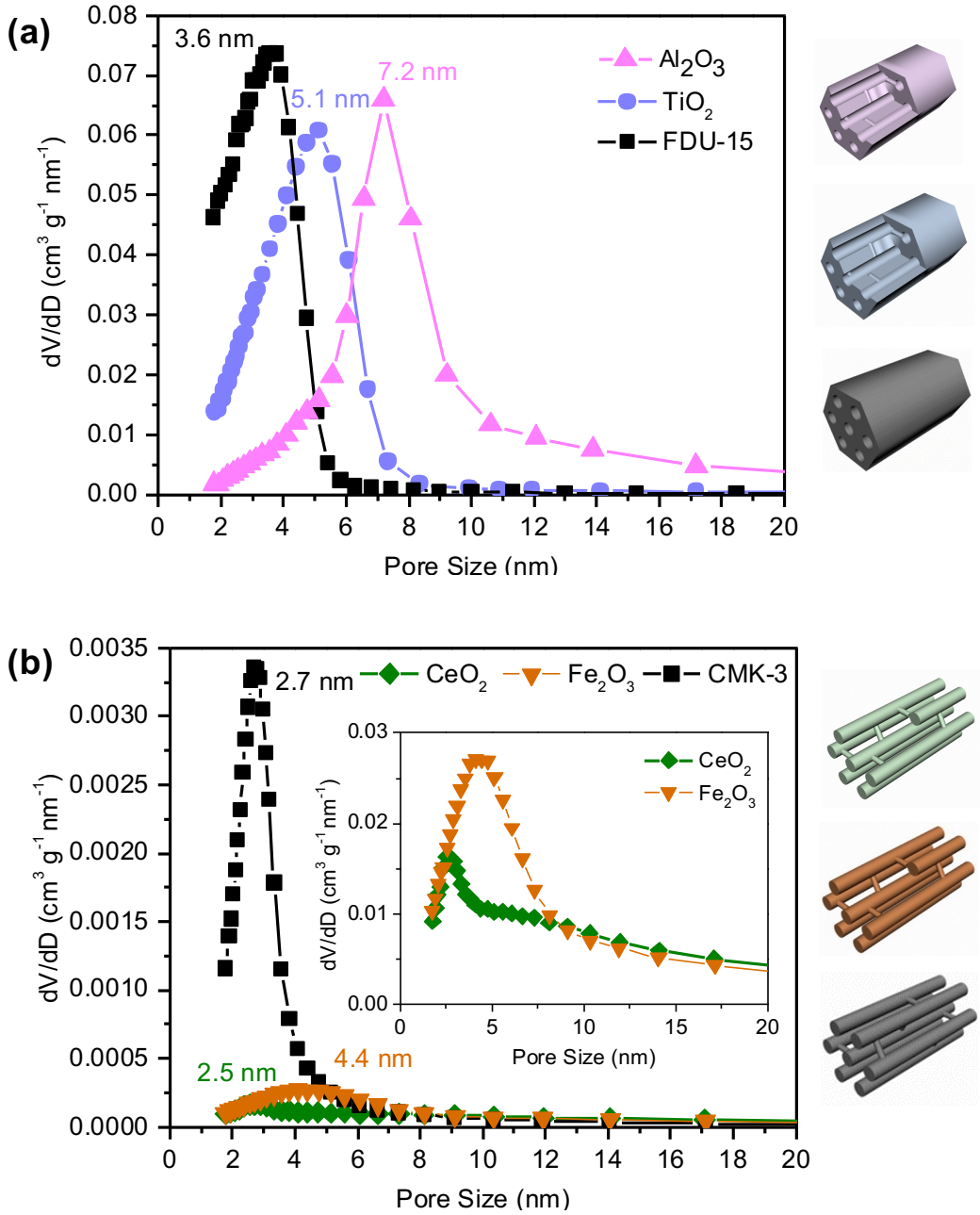

Figure 4.9. BJH pore size distributions for (a) meso-Al_2O_3 (pink), meso-TiO_2 (blue), and FDU-15 (gray), as well as (b) meso-CeO_2 (green), meso-Fe_2O_3 (brown), and CMK-3 (gray).

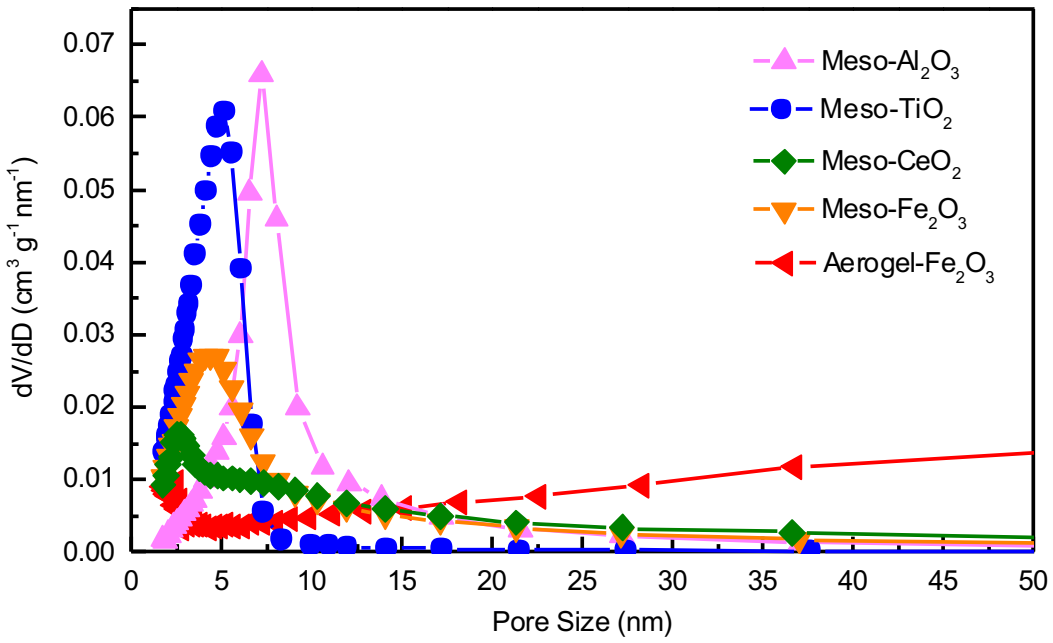

Figure 4.10. BJH pore size distributions for the diverse mesoporous metal oxides, meso-Al_2O_3 (pink), meso-TiO_2 (blue), meso-CeO_2 (green), meso-Fe_2O_3 (orange), and aerogel-Fe_2O_3 (red).

Table 4.1 lists the surface area, pore size, and volume of the all the mesoporous metal oxides, as well as FDU-15/CuO (endo and exo-pore), FDU-15, and BPL, for comparison. Of all the mesoporous metal oxides, TiO_2 has the highest surface area of 239 m^2 g^{-1}, while Al_2O_3 (175 m^2 g^{-1}), CeO_2 (123 m^2 g^{-1}), Fe_2O_3 (188 m^2 g^{-1}), and aerogel-Fe_2O_3 (131 m^2 g^{-1}) are relatively similar. Aerogel-Fe_2O_3 has the highest pore volume (0.87 cm^3 g^{-1}), over two times greater than Al_2O_3 (0.36 cm^3 g^{-1}), CeO_2 (0.28 cm^3 g^{-1}), Fe_2O_3 (0.30 cm^3 g^{-1}), and TiO_2 (0.23 cm^3 g^{-1}). These differences in pore properties (represented graphically in Figure 4.11) are significant, as we have seen from our previous studies how they influence DMMP adsorption and decomposition.

Table 4.1. N_2 Adsorption –Desorption Properties of Adsorbents

Samples	Pore Diameter (nm)[a]	Total Pore Volume ($cm^3\ g^{-1}$)[b]	Total Surface Area ($m^2\ g^{-1}$)[c]
Meso-Al_2O_3	7.2	0.36	175
Meso-TiO_2	5.1	0.23	239
Meso-CeO_2	2.5	0.28	123
Meso-Fe_2O_3	4.4	0.30	188
Fe_2O_3 aerogel	wide range	0.87	131
FDU-15/CuO endo and exo-pore	3.3	0.32	760
FDU-15	3.6	0.32	600
BPL	<1.7	0.39	1229

[a]Calculated using the Barrett-Joyner-Halenda (BJH) model.

[b]The total pore volume is based on the sum of the mesopore and macropore volume from the BJH model and the micropore volume from the t-plot method.

[c]Calculated using the multipoint Brunauer-Emmett-Teller (BET) method.

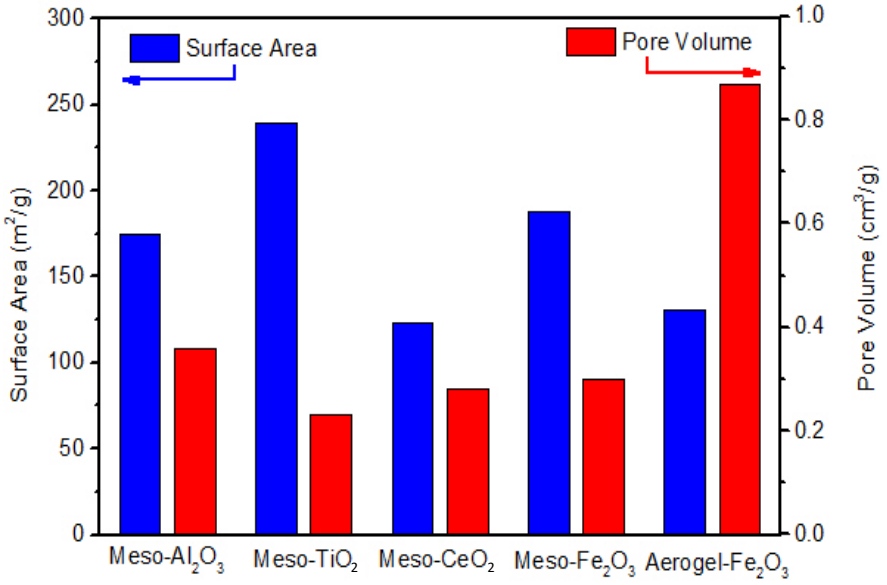

Figure 4.11. Graphical representation of the surface area and pore volume of the OMMs, meso-Al_2O_3, meso-TiO_2, meso-CeO_2, meso-Fe_2O_3, and aerogel-Fe_2O_3.

4.3.2 DMMP Decomposition Activity

DMMP decomposition has been observed on many dry and hydroxylated metal oxide surfaces, such as CuO,[31] MoO_3,[22, 40] TiO_2,[2, 24, 26, 30] MgO,[8, 16, 35-37] LaO,[16] Al_2O_3,[16, 17, 23, 25, 34, 38, 39] Fe_2O_3,[14, 16] and Ni, Fe, Cu, and V oxide supported on γ-Al_2O_3, SiO_2, TiO_2.[25] These studies revealed that DMMP decomposition results in the formation of surface phosphate, alkoxide, and alkyl groups, while subsequently forming gaseous byproducts, such as carbon dioxide, carbon monoxide, dimethyl ether, formaldehyde, formic acid, and most commonly, methanol (Figure 4.12).[2, 14-17, 23, 24, 26, 30, 34, 37, 38] The different mechanistic pathways were previously discussed in Chapter 1, Section 1.2.

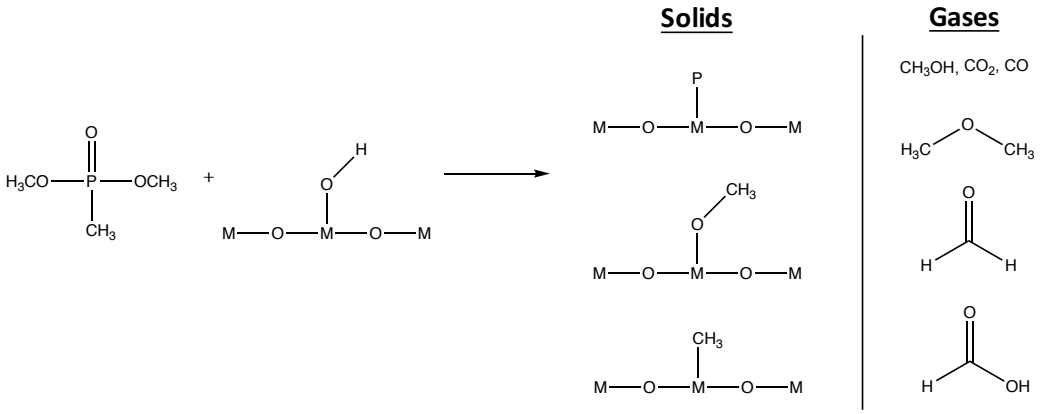

Figure 4.12. General schematic of DMMP decomposition on hydroxylated metal oxides, and the possible surface and gaseous byproducts.

DRIFTS studies were performed to monitor DMMP adsorption and decomposition on meso-TiO_2 and meso-CeO_2. The DRIFTS spectrum of DMMP

shows vibrational modes in good agreement with gas phase DMMP vibrational frequencies and modes in the literature.[26] The spectra shows that DMMP adsorbs and decomposes on meso-TiO_2 and meso-CeO_2 surfaces from the presence of the peak at 1098 cm^{-1}, which corresponds to a surface methoxy group, denoted as M-OCH_3 in Figure 4.13. This identification is based on prior work that investigated methanol adsorption on ThO_2, CeO_2, TiO_2, and CuO.[26, 219, 220] In addition, the peak corresponding to the phosphoryl (P=O) bond of adsorbed DMMP is shifted to a lower frequency with respect to the DMMP gas phase spectrum (1276 to 1242 cm^{-1}), which is a common feature for adsorbed DMMP on metal oxides.[26, 221] The lower frequency observed from the shift of the P=O is most likely due to a strong interaction of the phosphoryl's oxygen with a metal Lewis acid site or surface hydroxyl. The decrease in absorbance of the surface OH groups further supports DMMP interaction with the hydroxyls on the surface of these metal oxides. These hydroxyl groups can promote binding and decomposition, which leads to methanol formation at low temperatures.

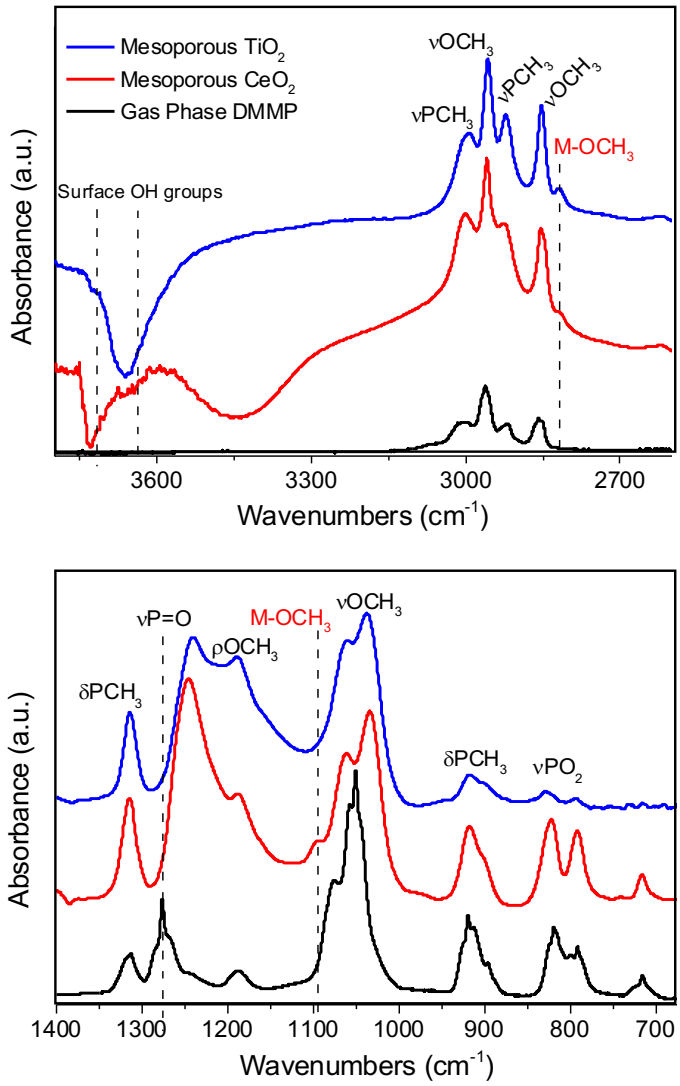

Figure 4.13. DRIFTS spectrum of gas phase DMMP (black line) in comparison to commercial DMMP adsorbed on meso-TiO_2 (blue line) and meso-CeO_2 (red line).

4.3.2.1 Determination of DMMP Conversion to Methanol

The extent of DMMP decomposition on the mesoporous metal oxides was measured by monitoring the evolution of gas-phase products by quantitative ^{1}H-NMR. The products were predominantly methanol with trace amounts of

formaldehyde. However, no phosphorus-containing products other than DMMP were detected in the volatile decomposition products, which agrees with literature results.[24] The phosphorus concentration of the potential surface-bound phosphate byproduct(s) was measured using ICP-AES after the TPD experiments. We observed three scenarios for DMMP conversion to methanol (Table 4.2):

1) 1-to-1 conversion on meso-Fe_2O_3 suggesting that each mole of DMMP produces a mole of gaseous CH_3OH, leaving behind a methyl methylphosphonate (MMP) surface group.[16, 39]
2) 1-to-1.6 conversion on meso-TiO_2 suggesting that each mole of DMMP may produce up to two moles of gaseous CH_3OH, leaving behind a methylphosphonate (MP) surface group.[2, 24, 26, 30]
3) 1-to-0.9 conversion on meso-Al_2O_3 suggesting that each mole of DMMP may produce a mole of gaseous CH_3OH, which partially undergoes oxidation to CO_2, CO, and H_2,[2, 14, 222] thereby explaining the mass balance discrepancy.

Table 4.2. Phosphorus Concentration of Cycled Mesoporous Metal Oxides

	Meso-Al_2O_3	**Meso-TiO_2**	**Meso-Fe_2O_3**
Observed[a] mg P/g material	14	6.1	5.5
Equivalent Amount of DMMP	0.9	1.6	1.0

[a]Observed values were calculated using ICP-AES to measure the P concentration at 178.3 nm.

The OMMs, Al_2O_3, Fe_2O_3, and TiO_2, have different adsorption sites allowing for the phosphoryl's oxygen to bind to the metal acid sites and surface hydroxyl groups through different interactions.[16] Unlike the other OMMs, meso-TiO_2 undergoes greater decomposition with the cleavage of a second methoxy group. This may be influenced by the rutile TiO_2 structure that provides the ideal coordination to facilitate increased DMMP decomposition.[223] Isotopic labelling experiments can provide more insight to this observation (further discussion in Chapter 5).

4.3.3 Evaluation of DMMP Adsorption/Decomposition Performance

The nature of the DMMP binding is stronger for the OMMs in comparison to carbon. DFT-calculations for DMMP adsorption on rutile TiO_2 (110) and α-Al_2O_3 (0001) surfaces were identified as chemisorption, which is evident by the high binding energies, 200.7 and 190.1 kJ mol^{-1}, respectively. These values represent the formation of a strong chemical bond between the phosphoryl oxygen and an under-coordinated surface metal atom (Figure 4.14). DMMP chemisorption to the highly reactive surface of Al_2O_3 and TiO_2, allows for 73 and 96% adsorbed DMMP decomposition, respectively. This differs from FDU-15, where 85% of the adsorbed DMMP remains fully intact on the inert carbon surface (Figure 4.15).

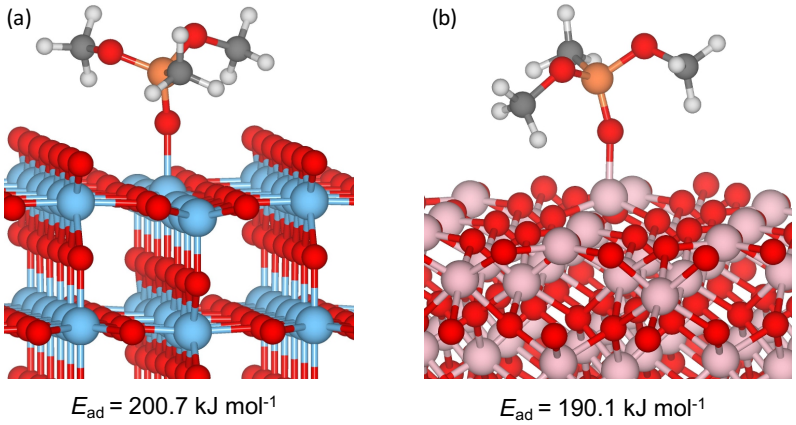

Figure 4.14. DMMP chemisorption on (a) rutile TiO_2 (110) surface and (b) α-Al_2O_3 (0001) surface. Preliminary data by Dr. Roman Tsyshevsky.

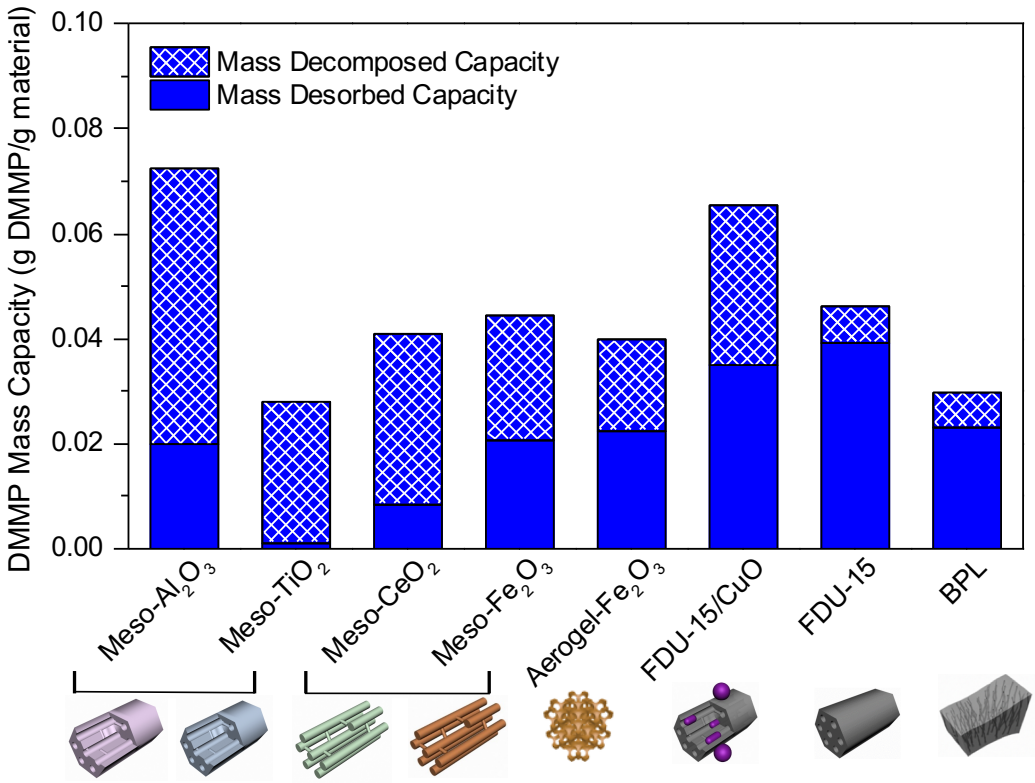

Figure 4.15. Graphical representation of the DMMP mass capacity of desorbed DMMP (solid bars) and decomposed DMMP (crisscross bars) for four different OMMs: meso-Al_2O_3, meso-TiO_2, meso-CeO_2, meso-Fe_2O_3, and disordered aerogel-Fe_2O_3, as well as carbon adsorbents: FDU-15/CuO (endo and exo-pore), FDU-15, and BPL.

Table 4.3. 5 h Mass Capacity of Decomposed DMMP, Desorbed DMMP, and Total Area Capacity for Various Adsorbents

Adsorbents	Decomposed DMMP (g/g)[a]	Desorbed DMMP (g/g)	Total Mass Capacity (g/g)
Meso-Al_2O_3	0.0528	0.0198	0.0726
Meso-TiO_2	0.0270	0.0011	0.0281
Meso-CeO_2	0.0325	0.0083	0.0408
Meso-Fe_2O_3	0.0237	0.0206	0.0443
Fe_2O_3 aerogel	0.0174	0.0225	0.0399
FDU-15/CuO	0.0304[b]	0.0349[b]	0.0653[b]
FDU-15	0.0070	0.0391	0.0461
BPL	0.0067	0.0231	0.0298

[a]Decomposed DMMP was calculated by applying a conversion factor for the mole ratio of DMMP to methanol from ICP-AES results (Table 4.2). The decomposed DMMP for CeO_2 was calculated by assuming a one-to-one conversion of DMMP to methanol.

[b]Measurements reported for the FDU-15/CuO composites were calculated after disregarding the CuO weight for a more accurate comparison.

DMMP decomposition, reported as the decomposed DMMP capacity, is 2 to 4 times higher for the OMMs than the carbon adsorbents, FDU-15 and BPL (Table 4.3). Illustrated in Figure 4.15, the total DMMP mass capacity decreases from meso-Al_2O_3 (175 m^2 g^{-1}) > meso-Fe_2O_3 (188 m^2 g^{-1}) > meso-CeO_2 (123 m^2 g^{-1}) > meso-TiO_2 (239 m^2 g^{-1}). It is evident that the mass capacity does not scale with the total surface area, as seen previously with carbon adsorbents in Chapter 2, and previously in the literature.[71, 76, 224] This deviation from surface area

dependence implies a shift from a physical adsorption mechanism to a chemical one, which agrees with our theoretical studies (Figure 4.14).

The desorbed (molecular) DMMP capacity for FDU-15 and FDU-15/CuO (endo and exo-pore) is higher than the mesoporous metal oxides, which we attribute to the larger surface area of the carbon-based adsorbents (600−760 m^2 g^{-1}) in comparison to the mesoporous metal oxides (123−239 m^2 g^{-1}). After normalizing the mass capacity to the surface area of each adsorbent, this allows for a comparison between DMMP adsorption and decomposition per m^2 of each material (Figure 4.16). After applying the surface area normalization, the area DMMP capacity for the mesoporous metal oxides are greater (>170%) than the carbon-based adsorbents, apart from meso-TiO_2. While meso-TiO_2 shows similar DMMP area capacity to FDU-15 and FDU-15/CuO, it is predominantly decomposed DMMP (Figure 4.16, Table 4.4). Our results imply that metal oxide surfaces have a higher reactivity in comparison to the carbon-based adsorbents.

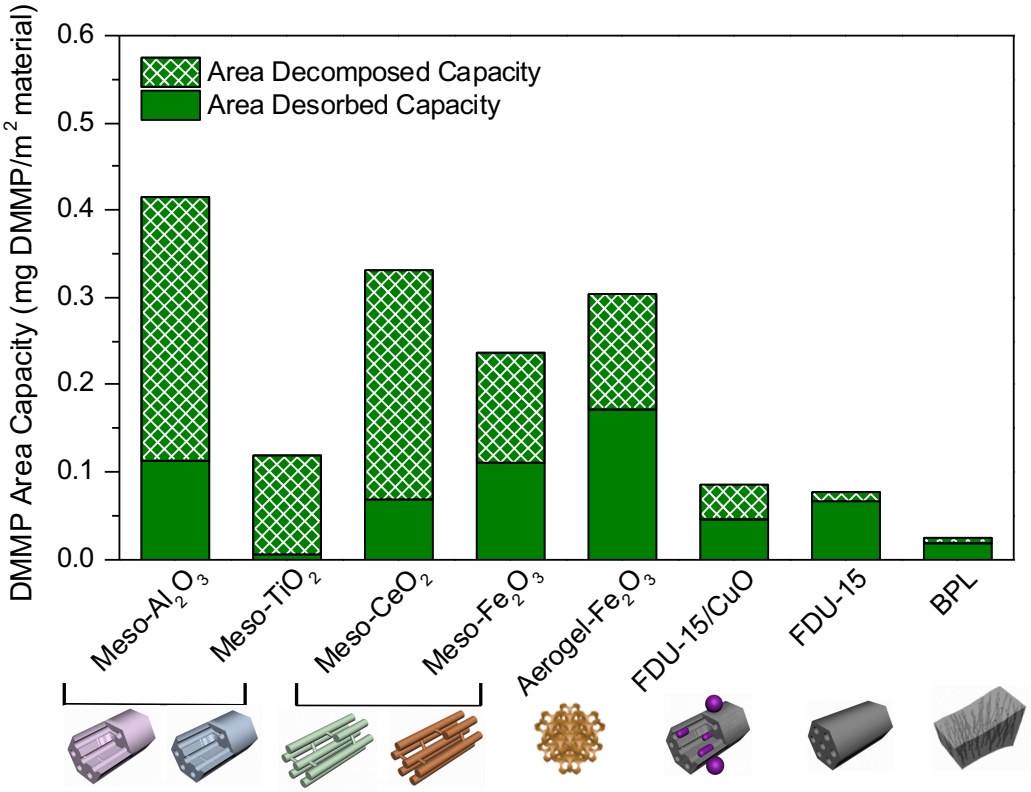

Figure 4.16. Graphical representation of the DMMP area capacity of desorbed DMMP (solid bars) and decomposed DMMP (crisscross bars) for four different OMMs: meso-Al_2O_3, meso-TiO_2, meso-CeO_2, meso-Fe_2O_3, and disordered aerogel-Fe_2O_3, as well as carbon adsorbents: FDU-15/CuO (endo and exo-pore), FDU-15, and BPL.

Table 4.4. 5 h Area Capacity of Decomposed DMMP, Desorbed DMMP, and Total Area Capacity for Various Adsorbents

Adsorbents	Decomposed DMMP (mg/m^2)[a]	Desorbed DMMP (mg/m^2)	Total Area Capacity (mg/m^2)[c]
Meso-Al_2O_3	0.3017	0.1131	0.4148
Meso-TiO_2	0.1144	0.0046	0.1190
Meso-CeO_2	0.2642	0.0675	0.3317
Meso-Fe_2O_3	0.1261	0.1096	0.2357
Fe_2O_3 aerogel	0.1328	0.1718	0.3046
FDU-15/CuO endo and exo-pore	0.0400[b]	0.0459[b]	0.0859[b]
FDU-15	0.0117	0.0652	0.0769
BPL	0.0055	0.0188	0.0243

[a]Decomposed DMMP was calculated by applying a conversion factor for the mole ratio of DMMP to methanol from ICP-AES results (Table 4.2). The decomposed DMMP for CeO_2 was calculated by assuming a one-to-one conversion of DMMP to methanol.

[b]Measurements reported for the FDU-15/CuO composites were calculated after disregarding the CuO weight for a more accurate comparison.

[c]Total area capacity was calculated by the mass capacity (Table 4.3) divided by the total surface area reported in Table 4.1.

Due to the large differences between metal oxide densities (3.95, 4.23, 7.22, 5.24, and 6.31 g cm^{-1}, for Al_2O_3, TiO_2, CeO_2, Fe_2O_3, and CuO, respectively), the DMMP mass capacity was further normalized by the density and pore volume of each material to determine the DMMP volume capacity. This allows for a comparison between DMMP adsorption and decomposition per cm^3 of each material. It was revealed that meso-Al_2O_3 achieved the greatest DMMP

total volume capacity in comparison to the other adsorbents. Figure 4.17 shows all OMMs (apart from meso-TiO_2) having a higher DMMP volume capacity than FDU-15 impregnated with endo and exo-pore CuO. However, meso-TiO_2 achieved the greatest DMMP decomposition by converting 96% of adsorbed DMMP to gaseous methanol. The lower surface area and disordered structure of aerogel Fe_2O_3 limits its ability to perform as well as the OMMs, yet it is still achieved greater DMMP decomposition in comparison to FDU-15 and BPL

(Table 4.5).

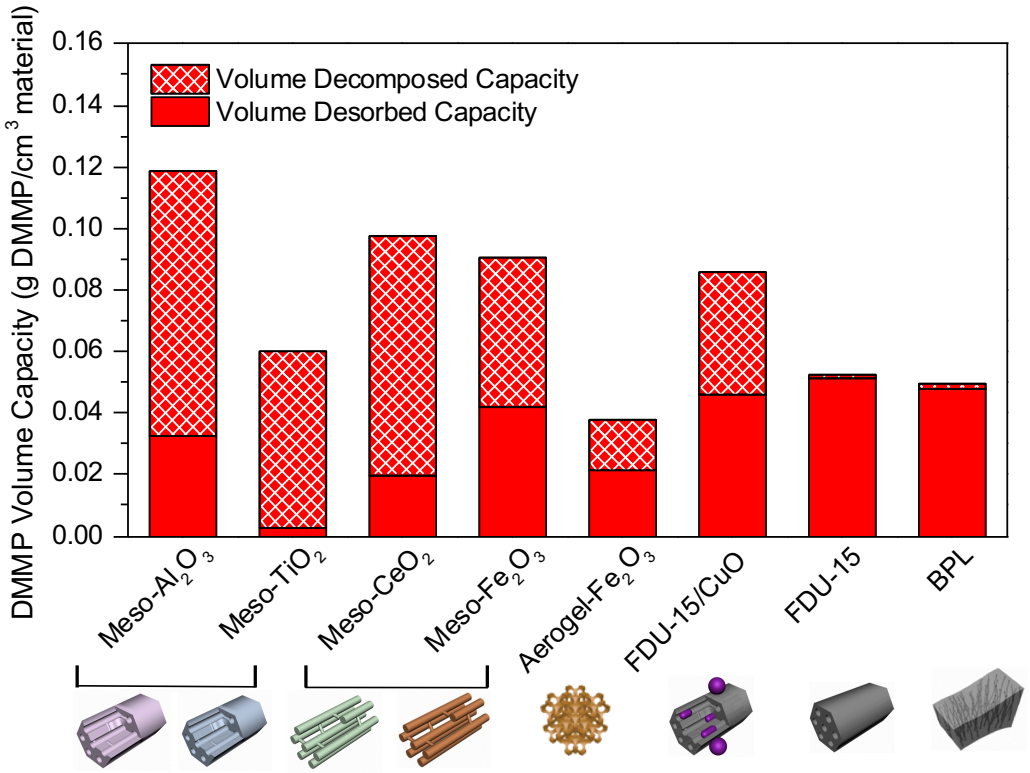

Figure 4.17. Graphical representation of the DMMP volume capacity of desorbed DMMP (solid bars) and decomposed DMMP (crisscross bars) for four different OMMs: meso-Al_2O_3, meso-TiO_2, meso-CeO_2, meso-Fe_2O_3, and disordered aerogel-Fe_2O_3, as well as carbon adsorbents: FDU-15/CuO (endo and exo-pore), FDU-15, and BPL.

Table 4.5. 5 h Volume Capacity of Decomposed DMMP, Desorbed DMMP, and Total Area Capacity for Various Adsorbents

Adsorbents	Decomposed DMMP (g/cm^3)[a]	Desorbed DMMP (g/cm^3)	Total Volume Capacity (g/cm^3)[c]
Meso-Al_2O_3	0.0862	0.0323	0.1185
Meso-TiO_2	0.0579	0.0024	0.0603
Meso-CeO_2	0.0777	0.0198	0.0975
Meso-Fe_2O_3	0.0483	0.0420	0.0903
Fe_2O_3 aerogel	0.0164	0.0212	0.0376
FDU-15/CuO endo and exo-pore	0.0398[b]	0.0458[b]	0.0856[b]
FDU-15	0.0010	0.0513	0.0523
BPL	0.0013	0.0479	0.0492

[a]Decomposed DMMP was calculated by applying a conversion factor for the mole ratio of DMMP to methanol from ICP-AES results (Table 4.2). The decomposed DMMP for CeO_2 was calculated by assuming a one-to-one conversion of DMMP to methanol.

[b]Measurements reported for the FDU-15/CuO composites were calculated after disregarding the CuO weight for a more accurate comparison.

[c]Total volume capacity calculated using the mass capacity (reported in Table 4.3) divided by the sum of the theoretical density and pore volume (Table 4.1). The theoretical densities used were 3.95, 4.23, 2.26, 7.22, 5.24, and 6.31 g cm^{-1}, for Al_2O_3, TiO_2, carbon, CeO_2, Fe_2O_3, and CuO, respectively.

4.4 CONCLUSIONS

In this investigation, we studied four different OMMs, Al_2O_3, TiO_2, CeO_2, and Fe_2O_3, with well-defined pore size, volume, and surface area. Disordered aerogel-Fe_2O_3 was also investigated for comparison. DRIFTS spectra of meso-TiO_2 and CeO_2 showed a strong interaction between the phosphoryl oxygen with a metal Lewis acid site or surface hydroxyl, characterized as chemisorption by DFT-based calculations. The decrease in absorbance of the surface OH groups further supports DMMP interaction with the hydroxyls on the surface of these metal oxides. These hydroxyl groups can promote binding and decomposition, which leads to methanol formation at low temperatures.

The extent of DMMP decomposition on the mesoporous metal oxides were measured by the evolution of gas-phase methanol. Our TPD measurements for meso-Al_2O_3 and meso-Fe_2O_3 suggest that DMMP conversion to methanol is roughly one-to-one, whereas meso-TiO_2 undergoes greater decomposition with the cleavage of a second methoxy group. This may be influenced by the rutile TiO_2 structure that provides the ideal coordination to facilitate increased DMMP decomposition.

The lower surface area and disordered structure limits the ability of aerogel Fe_2O_3 to adsorb high concentrations of DMMP, supported by the measured volume DMMP capacity (decomposed and desorbed), which was significantly lower than the OMMs. Meso-Al_2O_3 achieved the highest DMMP

total volume capacity in comparison to the other adsorbents. Conversely, meso-TiO_2 achieved the greatest DMMP conversion to methanol by decomposing 97% of adsorbed DMMP. Additional isotope labelling experiments are necessary to reveal mechanistic details in the decomposition of DMMP.

Chapter 5: Future Work and Outlook

This dissertation focused on understanding the adsorption properties and decomposition mechanisms of DMMP on different adsorbents to improve gas mask functionality. The effectiveness of these filters largely depends on the limited space available for physical adsorption in the pores, and the amount of reactive metal/metal oxides for chemical binding to the surface and/or decomposition. Our results revealed the significance of high surface area, large pore volume, and ordered structure for higher adsorption capacities, as well as abundant metal/metal oxide reactive sites for increased decomposition. The TPD/^{1}H-NMR methodology, coupled with ICP-AES bulk analysis was developed as a quantitative but generic tool that may be used to evaluate adsorption and/or decomposition of other simulants and agents (listed in Table 5.1).

The mesoporous metal oxides developed can be utilized by others to create catalytic materials resistant to phosphorus species deactivating the surface, which is one of the biggest limitations to ASZM-TEDA.[206, 207] Its been reported that TiO_2 is inert to P_2O_5 poisoning,[25] making it an ideal candidate for a new, more superior adsorbent; for example, mesoporous TiO_2 impregnated with CuO endo-pore nanoparticles. Meso-TiO_2/CuO may not replace ASZM-TEDA entirely, however, exchanging the second layer of ASZM-TEDA with highly reactive OMM/CuO would increase protection time, while using less material to make a smaller, lighter, and more portable gas mask, which is greatly desired for

field use (Figure 5.1). The impact of this work is not limited to gas mask filtration devices, but can also be expanded into fibers for protective clothing, and tarps for safe housing, in areas where CWAs are a persistent problem.

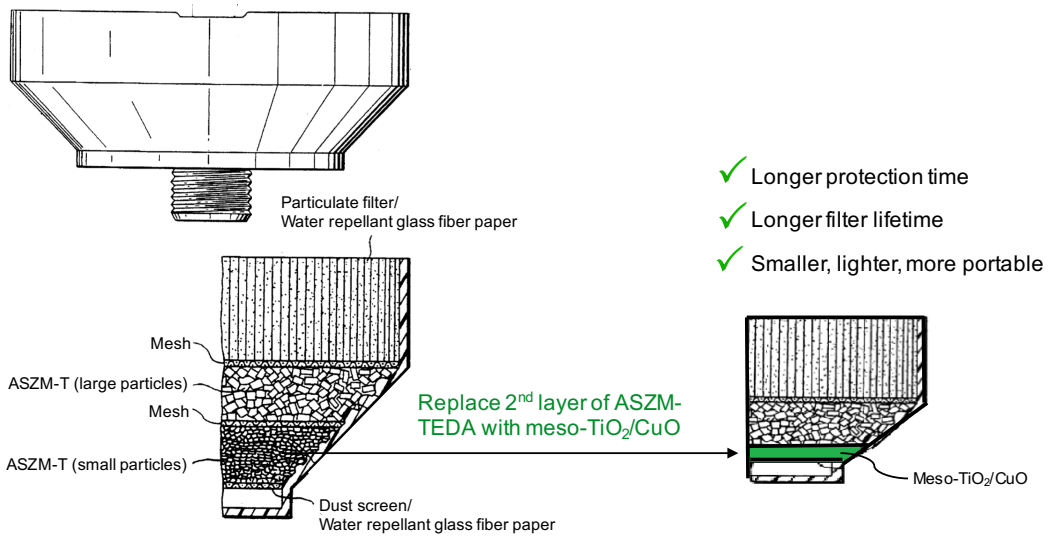

Figure 5.1. Schematic of a frustum layered canister with different sized ASZM-TEDA granules (to the left)[85] and a new canister with a mixture of ASZM-TEDA and meso-TiO_2/CuO (to the right).

There are still unanswered questions regarding the surface chemistry during DMMP decomposition. Trotochaud *et al.* proposed multiple mechanistic pathways for the formation of Cu−OCH_3 and O−CH_3 bonds on the CuO surface, which was observed using APXPS. The participation of O_{lat} in the formation of Cu−O_{lat}−P and O_{lat}−CH_3 bonds is also proposed, based on DFT calculations. Further investigation with deuterium labelled DMMP (Figure 5.2) and ^{18}O-labelled metal oxides can differentiate between the bond cleavages of P−OCH_3, PO−CH_3, and P−CH_3, and expose the role of lattice oxygens (O_{lat}) during the

decomposition of DMMP. Quantitative TPD experiments can reveal which pathways are more favorable and contribute additional insight on the surface chemistry of these metal oxides, which can further be used to rationally design superior gas mask devices.

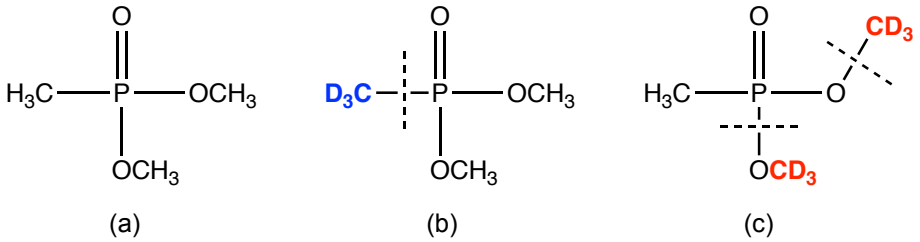

Figure 5.2. (a) Dimethyl methylphosphonate (DMMP), (b, c) Deuterium labelled DMMP, with possible bond cleavages are indicated with a dotted line.

Table 5.1. List of CWA simulants, sulfur mustard (HD/HT), sarin (GB), and VX.

HD/HT	GB	VX
2-chloroethyl ethyl sulfide (CEES)	diethyl methylphosphonate (DEMP)	diethyl methylphosphonate (DEMP)
2-chloroethyl phenyl sulfide (CEPS)	diisopropyl methylphosphonate (DIMP)	p-nitrophenyl diethylphosphate (PNPDEP or paraoxon)
di-n-butyl sulfide	diisopropyl phosphorofluoridate (DFP)	tri-n-butyl phosphate
methyl phenyl sulfide (thioanisole)	p-nitrophenyl diethylphosphate (PNPDEP or paraoxon)	O,S-diethyl methylphosphonothioate*
ethyl phenyl sulfide	p-nitrophenyl diphenylphosphate (PNPDPP)	O,S-diethyl phenylphosphonothioate

Publications

Huynh, K.; Holdren, S.; Hu, J.; Wang, L.; Zachariah, M. R.; Eichhorn, B. W., Dimethyl Methylphosphonate Adsorption Capacities and Desorption Energies on Ordered Mesoporous Carbons. *ACS Appl. Mater. Interfaces*, **2017**, *9,* 40638-40644.

Long, J.; Wallace, J.; Peterson, G.; Huynh, K. Manganese Oxide Nanoarchitectures as Broad-Spectrum Sorbents for Toxic Gases. *ACS Appl. Mater. Interfaces*, **2016**, *8 (2)*, 1184-1193.

References

1. Lenhart, M. K.; Tuorinsky, S. D., *Textbook of Military Medicine*. US Army Medical Department Center and School, Fort Sam Houston, TX, 2008.
2. Mera, N.; Hirakawa, T.; Sano, T.; Takeuchi, K.; Seto, Y.; Negishi, N., Removal of High Concentration Dimethyl Methylphosphonate in the Gas Phase by Repeated-Batch Reactions using TiO_2. *J. Hazard. Mater.* **2010,** *177*, 274-280.
3. Morita, H.; Yanagisawa, N.; Nakajima, T.; Shimizu, M.; Hirabayashi, H.; Okudera, H.; Nohara, M.; Midorikawa, Y.; Mimura, S., Sarin Poisoning in Matsumoto, Japan. *Lancet* **1995,** *346*, 290-293.
4. Suzuki, T.; Morita, H.; Ono, K.; Maekawa, K.; Nagai, R.; Yazaki, Y., Sarin Poisoning in Tokyo Subway. *Lancet* **1995,** *345*, 980-980.
5. Prentiss, A. M., *Chemicals in War. A Treatise on Chemical Warfare*. McGraw-Hill Book Company, Inc., Fort Sam Houston, TX, 1937; Vol. 2.
6. Khanday, W. A.; Majid, S. A.; Shekar, S. C.; Tomar, R., Synthesis and Characterization of Various Zeolites and Study of Dynamic Adsorption of Dimethyl Methylphosphate Over Them. *Mater. Res. Bull.* **2013,** *48*, 4679-4686.
7. Bartelt-Hunt, S. L.; Knappe, D. R. U.; Barlaz, M. A., A Review of Chemical Warfare Agent Simulants for the Study of Environmental Behavior. *Crit. Rev. Env. Sci. Technol.* **2008,** *38*, 112-136.
8. Li, Y. X.; Klabunde, K. J., Nanoscale Metal-Oxide Particles as Chemical Reagents - Destructive Adsorption of a Chemical-agent Simulant, Dimethyl Methylphosphonate, on Heat-treated Magnesium-Oxide. *Langmuir* **1991,** *7*, 1388-1393.
9. Graven, W. M.; Weller, S. W.; Peters, D. L., Catalytic Conversion of an Organophosphate Vapor Over Platinum-Alumina. *Ind. Eng. Chem. Process Des. Dev.* **1966,** *5*, 183.
10. Graven, W. M.; Paton, J. D.; Weller, S. W., Sorption of Dimethyl Methylphosphonate Vapor on an Amberlyst Cation Exchange Resin. *Ind. Eng. Chem. Prod. Res. Dev.* **1966,** *5*, 34.
11. Tzou, T. Z.; Weller, S. W., Catalytic-Oxidation of Dimethyl Methylphosphonate. *J. Catal.* **1994,** *146*, 370-374.
12. Oshea, K. E.; Beightol, S.; Garcia, I.; Aguilar, M.; Kalen, D. V.; Cooper, W. J., Photocatalytic Decomposition of Organophosphonates in Irradiated TiO_2 Suspensions. *J. Photochem. Photobiol., A* **1997,** *107*, 221-226.
13. Smentkowski, V. S.; Hagans, P.; Yates, J. T., Study of the Catalytic Destruction of Dimethyl Methylphosphonate-Oxidation Over MO(110). *J. Phys. Chem.* **1988,** *92*, 6351-6357.
14. Henderson, M. A.; Jin, T.; White, J. M., A TPD/AES Study of the Interaction of Dimethyl Methylphosphonate with alpha-Fe_2O_3 and SiO_2. *J. Phys. Chem.* **1986,** *90*, 4607-4611.

15. Ekerdt, J. G.; Klabunde, K. J.; Shapley, J. R.; White, J. M.; Yates Jr., J. T., Surface Chemistry of Organophosphorus Compounds. *J. Phys. Chem.* **1988**, *92*, 6182-6188.
16. Mitchell, M. B.; Sheinker, V. N.; Mintz, E. A., Adsorption and Decomposition of Dimethyl Methylphosphonate on Metal Oxides. *J. Phys. Chem. B* **1997,** *101*, 11192-11203.
17. Templeton, M. K.; Weinberg, W. H., Adsorption and Decomposition of Dimethyl Methylphosphonate on an Aluminum-Oxide Surface. *J. Amer. Chem. Soc.* **1985,** *107*, 97-108.
18. Lee, K. Y.; Houalla, M.; Hercules, D. M.; Hall, W. K., Catalytic Oxidative Decomposition of Dimethyl Methylphosphonate Over Cu-Substituted Hydroxyapatite. *J. Catal.* **1994,** *145*, 223-231.
19. Henderson, M. A.; White, J. M., Adsorption and Decomposition of Dimethyl Methylphosphonate on Platinum(111). *J. Am. Chem. Soc.* **1988,** *110*, 6939-6947.
20. Guo, X.; Yoshinobu, J.; Yates, J. T., Decomposition of an Organophosphonate Compound (Dimethyl Methylphosphonate) on the Ni(111) and Pd(111) Surfaces. *J. Phys. Chem.* **1990,** *94*, 6839-6842.
21. Hegde, R. I.; White, J. M., Interaction of Dimethyl Methylphosphonate with Oxidized Iron and the Effect of Coadsorbed Water. *Appl. Surf. Sci.* **1987,** *28*, 1-10.
22. Head, A. R.; Tsyshevsky, R.; Trotochaud, L.; Yu, Y.; Kyhl, L.; Karslioglu, O.; Kuklja, M. M.; Bluhm, H., Adsorption of Dimethyl Methylphosphonate on MoO_3: The Role of Oxygen Vacancies. *J. Phys. Chem. C* **2016,** *120*, 29077-29088.
23. Cao, L. X.; Suib, S. L.; Tang, X.; Satyapal, S., Thermocatalytic Decomposition of Dimethyl Methylphosphonate on Activated Carbon. *J. Catal.* **2001,** *197*, 236-243.
24. Moss, J. A.; Szczepankiewicz, S. H.; Park, E.; Hoffmann, M. R., Adsorption and Photodegradation of Dimethyl Methylphosphonate Vapor at TiO_2 Surfaces. *J. Phys. Chem. B* **2005,** *109*, 19779-19785.
25. Cao, L. X.; Segal, S. R.; Suib, S. L.; Tang, X.; Satyapal, S., Thermocatalytic Oxidation of Dimethyl Methylphosphonate on Supported Metal Oxides. *J. Catal.* **2000,** *194*, 61-70.
26. Rusu, C. N.; Yates, J. T., Adsorption and Decomposition of Dimethyl Methylphosphonate on TiO_2. *J. Phys. Chem. B* **2000,** *104*, 12292-12298.
27. Troya, D., Reaction Mechanism of Nerve-Agent Decomposition with Zr-Based Metal Organic Frameworks. *J. Phys. Chem. C* **2016,** *120*, 29312-29323.
28. O'Brien, C. J.; Greathouse, J. A.; Tenney, C. M., Dissociation of Sarin on a Cement Analogue Surface: Effects of Humidity and Confined Geometry. *J. Phys. Chem. C* **2016,** *120*, 28100-28109.
29. Vaiss, V. S.; Borges, I.; Leitao, A. A., Sarin Degradation Using Brucite. *J. Phys. Chem. C* **2011,** *115*, 24937-24944.

30. Obee, T. N.; Satyapal, S., Photocatalytic Decomposition of DMMP on Titania. *J. Photochem. Photobiol. A* **1998,** *118*, 45-51.
31. Trotochaud, L.; Tsyshevsky, R.; Holdren, S.; Fears, K.; Head, A. R.; Yu, Y.; Karshoglu, O.; Pletincx, S.; Eichhorn, B.; Owrutsky, J.; Long, J.; Zachariah, M.; Kuklja, M. M.; Bluhm, H., Spectroscopic and Computational Investigation of Room-Temperature Decomposition of a Chemical Warfare Agent Simulant on Polycrystalline Cupric Oxide. *Chem. Mater.* **2017,** *29*, 7483-7496.
32. DeCoste, J. B.; Peterson, G. W., Metal-Organic Frameworks for Air Purification of Toxic Chemicals. *Chem. Rev.* **2014,** *114*, 5695-5727.
33. Morrison, R. W., NBC Filter Performance. 2001.
34. Templeton, M. K.; Weinberg, W. H., Decomposition of Phosphonate Esters Adsorbed on Aluminum-Oxide. *J. Amer. Chem. Soc.* **1985,** *107*, 774-779.
35. Li, Y. X.; Koper, O.; Atteya, M.; Klabunde, K. J., Adsorption and Decomposition of Organophosphorus Compounds on Nanoscale Metal-Oxide Particles - in situ GC-MS Studies of Pulsed Microreactions Over Magnesium-Oxide. *Chem. Mater.* **1992,** *4*, 323-330.
36. Lin, S. T.; Klabunde, K. J., Thermally Activated Magnesium-Oxide Surface-Chemistry - Adsorption and Decomposition of Phosphorus-Compounds. *Langmuir* **1985,** *1*, 600-605.
37. Segal, S. R.; Suib, S. L.; Tang, X.; Satyapal, S., Photoassisted Decomposition of Dimethyl Methylphosphonate Over Amorphous Manganese Oxide Catalysts. *Chem. Mater.* **1999,** *11*, 1687-1695.
38. Mitchell, M. B.; Sheinker, V. N.; Tesfamichael, A. B.; Gatimu, E. N.; Nunley, M., Decomposition of Dimethyl Methylphosphonate (DMMP) on Supported Cerium and Iron Co-impregnated Oxides at Room Temperature. *J. Phys. Chem. B* **2003,** *107*, 580-586.
39. Sheinker, V. N.; Mitchell, M. B., Quantitative Study of the Decomposition of Dimethyl Methylphosphonate (DMMP) on Metal Oxides at Room Temperature and Above. *Chem. Mater.* **2002,** *14*, 1257-1268.
40. Head, A.; Tang, X.; Hicks, Z.; Wang, L.; Bleuel, H.; Holdren, S.; Trotochaud, L.; Yu, Y.; Kyhl, L.; Karsioglu, O.; Fears, K.; Owrutsky, J.; Zachariah, M.; Bowen, K.; Bluhm, H., Thermal Desorption of Dimethyl Methylphosphonate from MoO_3. Catal. Struct. React. **2017**, *3*, 112-118.

41. Doornkamp, C.; Ponec, V., The Universal Character of the Mars and Van Krevelen Mechanism. *J. Mol. Catal. Chem.* **2000,** *162*, 19-32.
42. Grootendorst, E. J.; Verbeek, Y.; Ponec, V., The Role of the Mars and van Krevelen Mechanism in the Selective Oxidation of Nitrosobenzene and the Deoxygenation of Nitrobenzene on Oxidic Catalysts. *J. Catal.* **1995,** *157*, 706-712.
43. Zhang, Z.; Yates Jr., J. T., *Defects at Oxide Surfaces*. Springer International Publishing: Switzerland, 2015.

44. Mars, P.; van Krevelen, D. W., Oxidation Carried Out by Means of Vanadium Oxide Catalysts. In *Conference on Oxidation Processes*, Amsterdam, 1954.
45. Freund, H. J.; Kuhlenbeck, H.; Libuda, J.; Rupprechter, G.; Baumer, M.; Hamann, H., Bridging the Pressure and Materials Gaps Between Catalysis and Surface Science: Clean and Modified Oxide Surfaces. *Top. Catal.* **2001,** *15*, 201-209.
46. Oosterbeek, H., Bridging the Pressure and Material Gap in Heterogeneous Catalysis: Cobalt Fischer-Tropsch Catalysts from Surface Science to Industrial Application. *Phys. Chem. Chem. Phys.* **2007,** *9*, 3570-3576.
47. Davis, M. E., Ordered Porous Materials for Emerging Applications. *Nature* **2002,** *417*, 813-821.
48. Hierarchically Structured Porous Materials: From Nanoscience to Catalysis, Separation, Optics, Energy, and Life Science. *Hierarchically Structured Porous Materials: from Nanoscience to Catalysis, Separation, Optics, Energy, and Life Science* **2012**, 1-651.
49. Thommes, M.; Kaneko, K.; Neimark, A. V.; Olivier, J. P.; Rodriguez-Reinoso, F.; Rouquerol, J.; Sing, K. S. W., Physisorption of Gases, with Special Reference to the Evaluation of Surface Area and Pore Size Distribution (IUPAC Technical Report). *Pure Appl. Chem.* **2015,** *87*, 1051-1069.
50. Thommes, M., Physical Adsorption Characterization of Nanoporous Materials. *Chem. Ing. Tech.* **2010,** *82*, 1059-1073.
51. Jagiello, J.; Thommes, M., Comparison of DFT Characterization Methods Based on N_2, Ar, CO_2, and H_2 Adsorption Applied to Carbons with Various Pore Size Distributions. *Carbon* **2004,** *42*, 1227-1232.
52. Hedden, R. C.; Lee, H. J.; Soles, C. L.; Bauer, B. J., Characterization of Pore Structure in a Nanoporous Low-Dielectric-Constant Thin Film by Neutron Porosimetry and X-ray Porosimetry. *Langmuir* **2004,** *20*, 6658-6667.
53. Vincent, O.; Marguet, B.; Stroock, A. D., Imbibition Triggered by Capillary Condensation in Nanopores. *Langmuir* **2017,** *33*, 1655-1661.
54. Everett, D. H., Solid-Gas Interface. *Chem. Br.* **1967,** *3*, 341.
55. Monson, P. A., Contact Angles, Pore Condensation, and Hysteresis: Insights from a Simple Molecular Model. *Langmuir* **2008,** *24*, 12295-12302.
56. Ball, P. C.; Evans, R., Temperature-Dependence of Gas-Adsorption on a Mesoporous Solid - Capillary Critically and Hysteresis. *Langmuir* **1989,** *5*, 714-723.
57. Ravikovitch, P. I.; Vishnyakov, A.; Russo, R.; Neimark, A. V., Unified Approach to Pore Size Characterization of Microporous Carbonaceous Materials from N_2, Ar, and CO_2 Adsorption Isotherms. *Langmuir* **2000,** *16*, 2311-2320.
58. Grosman, A.; Ortega, C., Capillary Condensation in Porous Materials. Hysteresis and Interaction Mechanism Without Pore Blocking/Percolation Process. *Langmuir* **2008,** *24*, 3977-3986.

59. Neimark, A. V.; Ravikovitch, P. I., Density Functional Theory of Adsorption Hysteresis and Nanopore Characterization. In *Characterization of Porous Solids V*, Unger, K. K.; Kreysa, G.; Baselt, J. P., Eds. 2000; *128*, 51-60.
60. Neimark, A. V.; Ravikovitch, P. I.; Vishnyakov, A., Adsorption Hysteresis in Nanopores. *Phys. Rev. E* **2000,** *62*, R1493-R1496.
61. Valiullin, R.; Naumov, S.; Galvosas, P.; Karger, J.; Woo, H. J.; Porcheron, F.; Monson, P. A., Exploration of Molecular Dynamics During Transient Sorption of Fluids in Mesoporous Materials. *Nature* **2006,** *443*, 965-968.
62. Thommes, M.; Kohn, R.; Froba, M., Sorption and Pore Condensation Behavior of Nitrogen, Argon, and Krypton in Mesoporous: MCM-48 Silica Materials. *J. Phys. Chem. B* **2000,** *104*, 7932-7943.
63. Nicolas, R.; Berube, F.; Kim, T. W.; Thommes, M.; Kleitz, F., Tailoring Mesoporosity and Intrawall Porosity in Large Pore Silicas: Synthesis and Nitrogen Sorption Behavior. *Zeolites and Related Materials: Trends, Targets and Challenges, Proceedings of the 4th International Feza Conference* **2008,** *174*, 141-148.
64. Fries, A. A.; West, C. J., *Chemical Warfare*. McGraw-Hill Book Company: New York, 1921.
65. Walk, R. D. The History of Military Mask Filters.
66. Deitz, V.; Puhala, R. J.; Stroup, D. B.; Dickey, G. F., Influence of Atmospheric Weathering on the Performance of Whetlerite. 1982.
67. Romero, J. V.; Smith, J. W. H.; White, C. L.; Trussler, S.; Croll, L. M.; Dahn, J. R., A Combinatorial Approach to Screening Carbon Based Materials for Respiratory Protection. *J. Hazard. Mater.* **2010,** *183*, 677-687.
68. Smith, J. W. H.; Romero, J. V.; Dahn, T. R.; Dunphy, K.; Croll, L. M.; Dahn, J. R., The Effect of Co-Impregnated Acids on the Performance of Zn-based Broad Spectrum Respirator Carbons. *J. Hazard. Mater.* **2012,** *235*, 279-285.
69. Saxena, A.; Singh, B.; Sharma, A.; Dubey, V.; Semwal, R. P.; Suryanarayana, M. V. S.; Rao, V. K.; Sekhar, K., Adsorption of Dimethyl Methylphosphonate on Metal Impregnated Carbons Under Static Conditions. *J. Hazard. Mater.* **2006,** *134*, 104-111.
70. Fortier, H.; Westreich, P.; Selig, S.; Zelenietz, C.; Dahn, J. R., Ammonia, Cyclohexane, Nitrogen and Water Adsorption Capacities of an Activated Carbon Impregnated with Increasing Amounts of $ZnCl_2$, and Designed to Chemisorb Gaseous NH_3 from an Air Stream. *J. Colloid Interface Sci.* **2008,** *320*, 423-435.
71. Nickolov, R. N.; Mehandjiev, D. R., Comparative Study on Removal Efficiency of Impregnated Carbons for Hydrogen Cyanide Vapors in Air Depending on their Phase Composition and Porous Textures. *J. Colloid Interface Sci.* **2004,** *273*, 87-94.
72. Liang, S. H.; Harrison, B. H.; Pagotto, J. G., Determination of the Impregnant Concentrations of ASC Type Charcoal. A Magnetic Susceptibility Study. Defence Research Establishment Ottawa: 1987; Report No. 973.

73. Mahle, J. J.; Peterson, G. W.; Schindler, B. J.; Smith, P. B.; Rossin, J. A.; Wagner, G. W., Role of TEDA as an Activated Carbon Impregnant for the Removal of Cyanogen Chloride from Air Streams: Synergistic Effect with Cu(II). *J. Phys. Chem. C* **2010,** *114*, 20083-20090.
74. Lee, Y. W.; Kim, H. J.; Park, J. W.; Choi, B. U.; Choi, D. K., Adsorption and Reaction Behavior for the Simultaneous Adsorption of NO-NO_2 and SO_2 on Activated Carbon Impregnated with KOH. *Carbon* **2003,** *41*, 1881-1888.
75. Park, S. W.; Park, H. S.; Lee, W. K.; Moon, H., Effect of Water-Vapor on Adsorption of Methyl-Iodide to Triethylenediamine-Impregnated Activated Carbons. *Sep. Technol.* **1995,** *5*, 35-44.
76. Wu, L. C.; Chang, T. H.; Chung, Y. C., Removal of Hydrogen Sulfide and Sulfur Dioxide By Carbons Impregnated with Triethylenediamine. *J. Air Waste Manag. Assoc.* **2007,** *57*, 1461-1468.
77. Rossin, J.; Petersen, E.; Tevault, D.; Lamontagne, R.; Isaacson, L., Effects of Environmental Weathering on the Properties of ASC-Whetlerite. *Carbon* **1991,** *29*, 197-205.
78. Park, S. H.; McClain, S.; Tian, Z. R.; Suib, S. L.; Karwacki, C., Surface and Bulk Measurements of Metals Deposited on Activated Carbon. *Chem. Mater.* **1997,** *9*, 176-183.
79. Hammarstrom, J. L.; Sacco, A., Investigation of Hydrogen Reactivity and its Use as a Surface Probe on High Surface-Area Copper Chromium Silver Impregnated Charcoal. *J. Catal.* **1986,** *100*, 293-304.
80. Hammarstrom, J. L.; Sacco Jr., A., Investigation of Deactivation Mechanisms of ASC Whetlerite Charcoal. *J. Catal.* **1988**, *112*, 267-281.
81. Rossin, J. A.; Morrison, R. W., Spectroscopic Analysis and Performance of an Experimental Copper-Zinc Impregnated, Activated Carbon. *Carbon* **1991,** *29*, 887-892.
82. Bac, N.; Hammarstrom, J. L.; Sacco, A., Thermal-Decomposition Studies on Copper-Chromium-Silver Impregnated Activated-Charcoal. *Carbon* **1987,** *25*, 545-549.
83. Ehrburger, P.; Lahaye, J.; Dziedzinl, P.; Fangeat, R., Effect of Aging on the Behavior of Copper-Chromium Compounds Supported on Activated Carbon. *Carbon* **1991,** *29*, 297-303.
84. Doughty, D.; Groose, J. Chromium-Free Impregnated Activated Carbon for Adsorption of Toxic Gases and/or Vapors. **1991**.
85. Newton, R. A. Frustrum Layered Canister. **1997**.
86. Sewell, T.; Balboa, A.; Peterson, G. W.; Karwacki, C. J. *Chemisorption of Arsine on Activated, Impregnated Carbon Adsorbents*; US Army Edgewood Chemical and Biological Center, Aberdeen Proving Ground, MD.
87. Newton, R. A.; Jones, P.; Morrison, R. W. *Layering ASZM-TEDA Carbon Beds of Varying Particle Sizes to Optimize Filter Performance*; Soldier Biological Chemical Command Aberdeen Proving Ground, MD, **2003.**

88. Ramaseshan, R.; Ying-Jun, L.; Sundarrajan, S.; Ramakrishna, S., Can the Activated Carbon That is Currently Used in NBC Protective Wear Be Replaced. *Advanced Structural and Functional Materials for Protection* **2008,** *136*, 1-21.
89. Karwacki, C. J.; Morrison, R. W., Adsorptive Retention of Volatile Vapors for Nondestructive Filter Leak Testing. *Ind. Eng. Chem. Res.* **1998,** *37*, 3470-3480.
90. Peterson, G. W.; Karwacki, C. J.; Rossin, J. A. *Novel Collective Protection Filters for Emerging TIC Requirements: Axial and Radial-Flow Filter Designs*; Edgewood Chemical Biological Center. U.S. Army Research, Development and Engineering Command, **2005**.
92. Knapke, M. J.; Rossin, J. A. Processes for Filtering Chemicals from Air Streams. **2017**.
94. Harris, R. K.; Thompson, T. V.; Norman, P. R.; Pottage, C., Phosphorus-31 NMR Studies of Adsorption Onto Activated Carbon. *Carbon* **1999,** *37*, 1425-1430.
95. Suzin, Y.; Buettner, L. C.; LeDuc, C. A., Behavior of Impregnated Activated Carbons heated to the Point of Oxidation. *Carbon* **1998,** *36*, 1557-1566.
96. van der Merwe, M. M.; Bandosz, T. J., A Study of Ignition of Metal Impregnated Carbons: the Influence of Oxygen Content in the Activated Carbon Matrix. *J. Colloid Interface Sci.* **2005,** *282*, 102-108.
97. Tsunoda, R., Asdorption of Organic Vapors on Active Carbons. *J. Colloid Interface Sci.* **1989,** *130*, 60-68.
98. Wood, G. O., Activtaed Carbon Adsorption Capacities for Vapors. *Carbon* **1992,** *30*, 593-599.
99. Furtado, A. M. B.; Wang, Y.; LeVan, M. D., Carbon Silica Composites for Sulfur Dioxide and Ammonia Adsorption. *Microporous and Mesoporous Mater.* **2013,** *165*, 48-54.
100. Sullivan, P.; Moate, J.; Stone, B.; Atkinson, J. D.; Hashisho, Z.; Rood, M. J., Physical and Chemical Properties of PAN-Derived Electrospun Activated Carbon Nanofibers and their Potential for Use as an Adsorbent for Toxic Industrial Chemicals. *Adsorption.* **2012,** *18*, 265-274.
101. Britt, D.; Tranchemontagne, D.; Yaghi, O. M., Metal-Organic Frameworks with High Capacity and Selectivity for Harmful Gases. *Proc. Natl. Acad. Sci. U.S.A.* **2008,** *105*, 11623-11627.
102. Petit, C.; Karwacki, C.; Peterson, G.; Bandosz, T. J., Interactions of Ammonia with the Surface of Microporous Carbon Impregnated with Transition Metal Chlorides. *J. Phys. Chem. C* **2007,** *111*, 12705-12714.
103. Kaplan, D.; Shmueli, L.; Nir, I.; Waysbort, D.; Columbus, I., Degradation of Adsorbed Sarin on Activated Carbons: A P-31-MAS-NMR Study. *Clean-Soil Air Water* **2007,** *35*, 172-177.
104. Ding, L. P.; Bhatia, S. K., Vacancy Solution Theory for Binary Adsorption Equilibria in Heterogeneous Carbon. *AlChE J.* **2002,** *48*, 1938-1956.

105. Keaney, A.; Alder, J. F., Mechanistic Study of the Effect of Sulphur Dioxide and Nitrogen Dioxide Exposure of ASC/T, Whetlerised BPL and Whetlerised Chlorinated BPL Activated Aarbons on the Chemisorption of Hydrogen Cyanide from Air. *Adsorpt. Sci. Technol.* **1998,** *16*, 101-115.
106. Lee, J. K.; Hudgins, R. R.; Silveston, P. L., SO_2 Oxidation in a Periodically Operated Trickle Bed: Comparison of Activated Carbon Catalysts. *Environ. Prog.* **1996,** *15*, 239-244.
107. Barton, S. S.; Evans, M. J. B.; Liang, S.; McDonald, J. A. F., The Influence of Surface Modification of BPL Carbons on Aging. *Carbon* **1996,** *34*, 975-982.
108. Tsai, W. T.; Chang, C. Y., Surface Characterization and Thermodynamics of Adsorption of Methylene-Chloride on Activated Carbons. *J. Environ. Sci. Health A Tox. Hazard Subst. Environ. Eng.* **1995,** *30*, 525-535.
109. Tsai, W. T.; Chang, C. Y., Surface-Chemistry of Activated Carbons and its Relevance for Effects of Relative-Humidity on Adsorption of Chlorinated Organic Vapors. *Chemosphere* **1994,** *29*, 2507-2515.
110. Tsai, W. T.; Chang, C. Y., Adsorption of Methylene-Chloride Vapor on Activated Carbons. *J. Chem. Technol. Biotechnol.* **1994,** *61*, 145-151.
111. Eissmann, R. N.; Levan, M. D., Coadsorption of Organic-Compounds and Water-Vapor on BPL Activated Carbon 2,1,1,2-Trichloro-1,2,2-Trifluoroethane and Dichloromethane. *Ind. Eng. Chem. Res.* **1993,** *32*, 2752-2757.
112. Brea, P.; Delgado, J. A.; Agueda, V. I.; Uguina, M. A., Modeling of Breakthrough Curves of N_2, CH_4, CO, CO_2 and a SMR Type Off-Gas Mixture on a Fixed Bed of BPL Activated Carbon. *Sep. Purif. Technol.* **2017,** *179*, 61-71.
113. Fan, W.; Chakraborty, A.; Kayal, S., Adsorption Cooling Cycles: Insights Into Carbon Dioxide Adsorption on Activated Carbons. *Energy* **2016,** *102*, 491-501.
114. Alvarez-Gutierrez, N.; Gil, M. V.; Martinez, M.; Rubiera, F.; Pevida, C., Phenol-Formaldehyde Resin-Based Carbons for CO_2 Separation at Sub-Atmospheric Pressures. *Energies* **2016,** *9*.
115. Delgado, J. A.; Agueda, V. I.; Uguina, M. A.; Sotelo, J. L.; Brea, P.; Grande, C. A., Adsorption and Diffusion of H_2/CO, CH_4, and CO_2 in BPL Activated Carbon and 13X Zeolite: Evaluation of Performance in Pressure Swing Adsorption Hydrogen Purification by Simulation. *Ind. Eng. Chem. Res.* **2014,** *53*, 15414-15426.
116. McEwen, J.; Hayman, J. D.; Yazaydin, A. O., A Comparative Study of CO_2, CH_4 and N_2 Adsorption in ZIF-8, Zeolite-13X and BPL Activated Carbon. *Chemical Physics* **2013,** *412*, 72-76.
117. Paez, C. A.; Contreras, M. S.; Leonard, A.; Blacher, S.; Olivera-Fuentes, C. G.; Pirard, J. P.; Job, N., Effect of CO_2 Activation of Carbon Xerogels on the Adsorption of Methylene Blue. *Adsorption.* **2012,** *18*, 199-211.

118. Liu, Z. S.; Wang, Q.; Zou, Z. S.; Tan, G. L., Arrhenius Parameters Determination in Non-Isothermal Conditions for the Uncatalyzed Gasification of Carbon By Carbon Dioxide. *Thermochim. Acta* **2011,** *512*, 1-4.
119. Martin, C. F.; Stockel, E.; Clowes, R.; Adams, D. J.; Cooper, A. I.; Pis, J. J.; Rubiera, F.; Pevida, C., Hypercrosslinked Organic Polymer Networks as Potential Adsorbents for Pre-combustion CO_2 Capture. *J. Mater. Chem.* **2011,** *21*, 5475-5483.
120. Banerjee, R.; Furukawa, H.; Britt, D.; Knobler, C.; O'Keeffe, M.; Yaghi, O. M., Control of Pore Size and Functionality in Isoreticular Zeolitic Imidazolate Frameworks and their Carbon Dioxide Selective Capture Properties. *J. Amer. Chem. Soc.* **2009,** *131*, 3875.
121. Nguyen, T. X.; Bhatia, S. K., Kinetic Restriction of Simple Gases in Porous Carbons: Transition-State Theory Study. *Langmuir* **2008,** *24*, 146-154.
122. Sullivan, P. D.; Stone, B. R.; Hashisho, Z.; Rood, M. J., Water Adsorption with Hysteresis Effect onto Microporous Activated Carbon Fabrics. *Adsorption* **2007,** *13*, 173-189.
123. Liu, J. C.; Monson, P. A., Monte Carlo Simulation Study of Water Adsorption in Activated Carbon. *Ind. Eng. Chem. Res.* **2006,** *45*, 5649-5656.
124. Sattler, M. L.; Rosenberk, R. S., Removal of Carbonyl Sulfide Using Activated Carbon Adsorption. *J. Air Waste Manag. Assoc.* **2006,** *56*, 219-224.
125. Nan, Q.; LeVan, M. D., Adsorption Equilibrium Modeling for Water on Activated Carbons. *Carbon* **2005,** *43*, 2258-2263.
126. Nguyen, T. X.; Bhatia, S. K.; Nicholson, D., Prediction of High-Pressure Adsorption Equilibrium of Supercritical Gases Using Density Functional Theory. *Langmuir* **2005,** *21*, 3187-3197.
127. Belmabkhout, Y.; De Weireld, G.; Frere, M., High-Pressure Adsorption Isotherms of N_2, CH_4, O_2, and Ar on Different Carbonaceous Adsorbents. *J. Chem. Eng. Data* **2004,** *49*, 1379-1391.
128. Sward, B. K.; LeVan, M. D., Frequency Response Method for Measuring Mass Transfer Rates in Adsorbents via Pressure Perturbation. *Adsorption* **2003,** *9*, 37-54.
129. Sun, J.; Chen, S.; Rood, M. J.; Rostam-Abadi, M., Correlating N_2 and CH_4 Adsorption on Microporous Carbon Using a New Analytical Model. *Energy Fuels* **1998,** *12*, 1071-1078.
130. Tanida, K.; Sato, Y.; Masuoka, H., Measurement and Correlation of Supercritical Carbon Dioxide Adsorption on Activated Carbon. *Kagaku Kogaku Ronbun.* **1996,** *22*, 385-391.
131. Shen, C. M.; Worek, W. M., Cosorption Characteristics of Solid Adsorbents. *Int. J. Heat Mass Transfer* **1994,** *37*, 2123-2129.
132. Hassan, N. M.; Ghosh, T. K.; Hines, A. L.; Loyalka, S. K., Adsorption of Water-Vapor on BPL Activated Carbon. *Carbon* **1991,** *29*, 681-683.

133. Nastaj, J.; Witkiewicz, K.; Chybowska, M., Modeling of Multicomponent and Multitemperature Adsorption Equilibria of Water Vapor and Organic Compounds on Activated Carbons. *Adsorpt. Sci. Technol.* **2016,** *34*, 144-175.
134. Delgado, J. A.; Agueda, V. I.; Uguina, M. A.; Sotelo, J. L.; Garcia-Sanz, A.; Garcia, A., Separation of Ethanol-Water Liquid Mixtures By Adsorption on BPL Activated Carbon with Air Regeneration. *Sep. Purif. Technol.* **2015,** *149*, 370-380.
135. Mitchell, L. A.; Schindler, B. J.; Das, G.; dos Ramos, M. C.; McCabe, C.; Cummings, P. T.; LeVan, M. D., Prediction of n-Alkane Adsorption on Activated Carbon Using the SAFT-FMT-DFT Approach. *J. Phys. Chem. C* **2015,** *119*, 1457-1463.
136. Wang, Y.; Mahle, J. J.; Furtado, A. M. B.; Glover, T. G.; Buchanan, J. H.; Peterson, G. W.; Levan, M. D., Mass Transfer and Adsorption Equilibrium for Low Volatility Alkanes in BPL Activated Carbon. *Langmuir* **2013,** *29*, 2935-2945.
137. Glover, T. G.; Peterson, G. W.; Schindler, B. J.; Britt, D.; Yaghi, O., MOF-74 Building Unit has a Direct Impact on Toxic Gas Adsorption. *Chem. Eng. Sci.* **2011,** *66*, 163-170.
138. Nabatilan, M. M.; Moe, W. M., Effects of Water Vapor on Activated Carbon Load Equalization of Gas Phase Toluene. *Water Res.* **2010,** *44*, 3924-3934.
139. Nabatilan, M. M.; Harhad, A.; Wolenski, P. R.; Moe, W. M., Activated Carbon Load Equalization of Transient Concentrations of Gas-Phase Toluene: Effect of Gas Flow Rate During Pollutant Non-Loading Intervals. *Chem. Eng. J.* **2010,** *157*, 339-347.
140. Glover, T. G.; Wang, Y.; Levan, M. D., Diffusion of Condensable Vapors in Single Adsorbent Particles Measured via Concentration-Swing Frequency Response. *Langmuir* **2008,** *24*, 13406-13413.
141. Schindler, B. J.; Buettner, L. C.; Levan, M. D., Transition to Henry's law in Ultra-Low Concentration Adsorption Equilibrium for n-Pentane on BPL Activated Carbon. *Carbon* **2008,** *46*, 1285-1293.
142. Wang, Y.; Levan, M. D., Nanopore Diffusion Rates for Adsorption Determined by Pressure-Swing and Concentration-Swing Frequency Response and Comparison with Darken's Equation. *Ind. Eng. Chem. Res.* **2008,** *47*, 3121-3128.
143. Glover, T. G.; LeVan, M. D., Sensitivity Analysis of Adsorption Bed Behavior: Examination of Pulse Inputs and Layered-bed Optimization. *Chem. Eng. Sci.* **2008,** *63*, 2086-2098.
144. Moe, W. M.; Collins, K. L.; Rhodes, J. D., Activated Carbon Load Equalization of Gas-Phase Toluene: Effect of Cycle Length and Fraction of Time in Loading. *Environ. Sci. Technol.* **2007,** *41*, 5478-5484.

145. Hung, H. W.; Lin, T. F., Prediction of the Adsorption Capacity for Volatile Organic Compounds onto Activated Carbons by the Dubinin-Radushkevich-Langmuir Model. *J. Air Waste Manag. Assoc.* **2007,** *57*, 497-506.
146. Walton, K. S.; Cavalcante, C. L.; Levan, M. D., Adsorption of Light Alkanes on Coconut Nanoporous Activated Carbon. *Braz. J. Chem. Eng.* **2006,** *23*, 555-561.
147. Crespo, D.; Yang, R. T., Adsorption of Organic Vapors on Single-Walled Carbon Nanotubes. *Ind. Eng. Chem. Res.* **2006,** *45*, 5524-5530.
148. Kim, D.; Cai, Z. L.; Sorial, G. A., Determination of Gas Phase Adsorption Isotherms - A Simple Constant Volume Method. *Chemosphere* **2006,** *64*, 1362-1368.
149. Walton, K. S.; Levan, M. D., Natural Gas Storage Cycles: Influence of Nonisothermal Effects and Heavy Alkanes. *Adsorption* **2006,** *12*, 227-235.
150. Chiang, H. L.; Lin, K. H.; Chen, C. Y.; Choa, C. G.; Hwu, C. S.; Lai, N., Adsorption Characteristics of Benzene on Biosolid Adsorbent and Commercial Activated Carbons. *J. Air Waste Manag. Assoc.* **2006,** *56*, 591-600.
151. Li, X.; Guo, H. F.; Chen, H. M., Determination of the Activation Energy for Desorption by Derivative Thermogravimetric Analysis. *Adsorpt. Sci. Technol.* **2006,** *24*, 907-914.
152. He, Y. F.; Seaton, N. A., Monte Carlo Simulation and Pore-Size Distribution Analysis of the Isosteric Heat of Adsorption of Methane in Activated Carbon. *Langmuir* **2005,** *21*, 8297-8301.
153. Seaton, N. A.; Walton, J.; Quirke, N., A New Analysis Method for the Determination of the Pore-Size Distribution of Porous Carbons from Nitrogen Adsorption Measurements. *Carbon* **1989,** *27*, 853-861.
154. Himeno, S.; Okubo, K.; Fujita, S., Prediction of Non-Ideal Binary Gas Adsorption Equilibria of Volatile Organic Compounds by the Thermodynamic Non-Ideal Adsorbed Solution Model. *Kagaku Kogaku Ronbun.* **2006,** *32*, 79-87.
155. Moe, W. M.; Li, C. N., A Design Methodology for Activated Carbon Load Equalization Systems Applied to Biofilters Treating Intermittent Toluene Loading. *Chem. Eng. J.* **2005,** *113*, 175-185.
156. Qi, N.; LeVan, M. D., Coadsorption of Organic Compounds and Water Vapor on BPL Activated Carbon. 5-Methylethylketone, Methylisobutylketone, Toluene, and Modeling. *Ind. Eng. Chem. Res.* **2005,** *44*, 3733-3741.
157. Walton, K. S.; Pigorini, G.; LeVan, M. D., Simple Group Contribution Theory for Adsorption of Alkanes in Nanoporous Carbons. *Chem. Eng. Sci.* **2004,** *59*, 4425-4432.
158. He, Y. F.; Yun, J. H.; Seaton, N. A., Adsorption Equilibrium of Binary Methane/Ethane Mixtures in BPL Activated Carbon: Isotherms and Calorimetric Heats of Adsorption. *Langmuir* **2004,** *20*, 6668-6678.
159. Jorge, M.; Seaton, N. A., Predicting Adsorption of Water/Organic Mixtures Using Molecular Simulation. *AlChE J.* **2003,** *49*, 2059-2070.

160. Ye, X. H.; Qi, N.; Ding, Y. Q.; LeVan, M. D., Prediction of Adsorption Equilibrium Using a Modified D-R Equation: Pure Organic Compounds on BPL Carbon. *Carbon* **2003,** *41*, 681-686.
161. Ye, X. H.; Qi, N.; LeVan, M. D., Prediction of Adsorption Equilibrium Using a Modified D-R Equation: Organic-Water Vapor Mixtures on BPL Carbon. *Carbon* **2003,** *41* (13), 2519-2525.
162. MacDonald, J. A. F.; Evans, M. J. B., Adsorption and enthalpy of phenol on BPL carbon. *Carbon* **2002,** *40* (5), 703-707.
163. LeVan, M. D.; Pigorini, G., Group-contribution theory for coadsorption of gases and vapors on solid surfaces. *Foundations of Molecular Modeling and Simulation* **2001,** *97* (325), 296-299.
164. Davies, G. M.; Seaton, N. A.; Vassiliadis, V. S., Calculation of pore size distributions of activated carbons from adsorption isotherms. *Langmuir* **1999,** *15* (23), 8235-8245.
165. Tsai, W. T.; Chang, C. Y.; Ho, C. Y.; Chen, L. Y., Adsorption Properties and Breakthrough Model of 1,1-Dichloro-1-fluoroethane on Activated Carbons. *J. Hazard. Mater.* **1999,** *69*, 53-66.
166. Taqvi, S. M.; Appel, W. S.; LeVan, M. D., Coadsorption of Organic Compounds and Water Vapor on BPL Activated Carbon. 4. Methanol, Ethanol, Propanol, Butanol, and Modeling. *Ind. Eng. Chem. Res.* **1999,** *38*, 240-250.
167. Zhao, X. S.; Ma, Q.; Lu, G. Q. M., VOC Removal: Comparison of MCM-41 with Hydrophobic Zeolites and Activated Carbon. *Energy Fuels* **1998,** *12*, 1051-1054.
168. Lehmann, C. M. B.; Rostam-Abadi, M.; Rood, M. J.; Sun, J., Reprocessing and Reuse of Waste Tire Rubber to Solve Air-Quality Related Problems. *Energy Fuels* **1998,** *12*, 1095-1099.
169. Russell, B. P.; LeVan, M. D., Coadsorption of Organic Compounds and Water Vapor on BPL Activated Carbon. 3. Ethane, Propane, and Mixing Rules. *Ind. Eng. Chem. Res.* **1997,** *36*, 2380-2389.
170. Sun, J.; Rood, M. J.; RostamAbadi, M.; Lizzio, A. A., Natural Gas Storage with Activated Carbon from a Bituminous Coal. *Gas Sep. Purif.* **1996,** *10*, 91-96.
171. Shojibara, H.; Sato, Y.; Takishima, S.; Masuoka, H., Adsorption Equilibria of Benzene on Activated Carbon in the Presence of Supercritical Carbon-Dioxide. *J. Chem. Eng. Jpn.* **1995,** *28*, 245-249.
172. Rudisill, E. N.; Hacskaylo, J. J.; Levan, M. D., Coadsorption of Hydrocarbons and Water on BPL Activated Carbon. *Ind. Eng. Chem. Res.* **1992,** *31*, 1122-1130.
173. Herrera, L. F.; Fan, C. Y.; Nguyen, V.; Do, D. D.; Horikawa, T.; Nicholson, D., A Self-Consistent Method to Determine Accessible Volume, Area and Pore Size Distribution (APSD) of BPL, Norit and AX-21 Activated Carbon. *Carbon* **2012,** *50*, 500-509.
174. Russell, B. P.; LeVan, M. D., Pore Size Distribution of BPL Activated Carbon Determined by Different Methods. *Carbon*, *32*.

175. Smith, S. J.; Hern, J. A. Broad Spectrum Filter System for Filtering Contaminants from Air or Other Gases. **2002.**
189. Bering, B. P.; Dubinin, M. M.; Serpinsky, V. V., Theory of Volume Filling for Vapor Adsorption. J. Colloid Interface Sci. **1966,** *21*, 378-393.
190. Yang, L.; Shroll, R. M.; Zhang, J. X.; Lourderaj, U.; Hase, W. L., Theoretical Investigation of Mechanisms for the Gas-Phase Unimolecular Decomposition of DMMP. *J. Phys. Chem. A* **2009,** *113*, 13762-13771.
191. Ahmadian, N.; Ganji, M. D.; Laffafchy, M., Theoretical Investigation of Nerve Agent DMMP Adsorption onto Stone-Wales Defected Single-Walled Carbon Nanotube. *Mater. Chem. Phys.* **2012,** *135*, 569-574.
192. Li, Z. Y.; Liu, Y. S.; Yang, X.; Xing, Y.; Wang, Z. Y.; Yang, Q.; Yang, R. T., Desorption Kinetics of Naphthalene and Acenaphthene over Two Activated Carbons via Thermogravimetric Analysis. *Energy Fuels* **2015,** *29*, 5303-5310.
193. Zacharia, R.; Ulbricht, H.; Hertel, T., Interlayer Cohesive Energy of Graphite from Thermal Desorption of Polyaromatic Hydrocarbons. *Phys. Rev. B* **2004,** *69*, 7.
194. Li, Z. Y.; Liu, Y. S.; Yang, X.; Xing, Y.; Tsai, C. J.; Wang, Z. Y.; Yang, Q.; Yang, R. T., Desorption of Polycyclic Aromatic Hydrocarbons on Mesoporous Sorbents: Thermogravimetric Experiments and Kinetics Study. *Ind. Eng. Chem. Res.* **2016,** *55*, 1183-1191.
195. Li, Z. Y.; Liu, Y. S.; Yang, X.; Xing, Y.; Tsai, C. J.; Meng, M. M.; Yang, R. T., Performance of Mesoporous Silicas and Carbon in Adsorptive Removal of Phenanthrene as a Typical Gaseous Polycyclic Aromatic Hydrocarbon. *Microporous Mesoporous Mater.* **2017,** *239*, 9-18.
196. Liu, Y. S.; Li, Z. Y.; Yang, X.; Xing, Y.; Tsai, C. J.; Yang, Q.; Wang, Z. Y.; Yang, R. T., Performance of Mesoporous Silicas (MCM-41 and SBA-15) and Carbon (CMK-3) in the Removal of Gas-Phase Naphthalene: Adsorption Capacity, Rate and Regenerability. *RSC Adv.* **2016,** *6*, 21193-21203.
197. Zhang, B.; Qin, X.; Li, G. R.; Gao, X. P., Enhancement of Long Stability of Sulfur Cathode by Encapsulating Sulfur into Micropores of Carbon Spheres. *Energy Environ. Sci.* **2010,** *3*, 1531-1537.
198. Johnson, S. A.; Brigham, E. S.; Ollivier, P. J.; Mallouk, T. E., Effect of Micropore Topology on the Structure and Properties of Zeolite Polymer Replicas. *Chem. Mater.* **1997,** *9*, 2448-2458.
199. Meng, Y.; Gu, D.; Zhang, F. Q.; Shi, Y. F.; Yang, H. F.; Li, Z.; Yu, C. Z.; Tu, B.; Zhao, D. Y., Ordered Mesoporous Polymers and Homologous Carbon Frameworks: Amphiphilic Surfactant Templating and Direct Transformation. *Angew. Chem. Int. Ed.* **2005,** *44*, 7053-7059.
200. Jun, S.; Joo, S. H.; Ryoo, R.; Kruk, M.; Jaroniec, M.; Liu, Z.; Ohsuna, T.; Terasaki, O., Synthesis of New, Nanoporous Carbon with Hexagonally Ordered Mesostructure. *J. Amer. Chem. Soc.* **2000,** *122*, 10712-10713.
201. Kim, T. W.; Kleitz, F.; Paul, B.; Ryoo, R., MCM-48-like Large Mesoporous Silicas with Tailored Pore Structure: Facile Synthesis Domain in a

Ternary Triblock Copolymer-Butanol-Water System. *J. Amer. Chem. Soc.* **2005,** *127*, 7601-7610.
202. Lastoskie, C.; Gubbins, K. E.; Quirke, N., Pore-Size Heterogeneity and the Carbon Slit Pore - A Density-Functional Theory Model. *Langmuir* **1993,** *9*, 2693-2702.
203. Lastoskie, C.; Gubbins, K. E.; Quirke, N., Pore-Size Distribution Analysis of Microporous Carbons - A Density-Functional Theory Approach. *J. Phys. Chem.* **1993,** *97*, 4786-4796.
203. McGarvey, W. R.; Creasy, W. R. *Headspace Gas Chromatography Method for Studies of Reaction and Permeation of Volatile Agents with Solid Materials*; Edgewood Chemical Biological Center. U.S. Army Research, Development and Engineering Command. Aberdeen Proving Ground, MD 21010-5424., **2005**; 1-34.
204. Starink, M., The Determination of Activation Energy from Linear Heating Rate Experiments: A Comparison of the Accuracy of Isoconversion Methods. *Thermochim. Acta* **2003,** *404*, 163-176.
205. Starink, M. J., A New Method for the Derivation of Activation Energies from Experiments Performed at Constant Heating Rate. *Thermochim. Acta* **1996,** *288*, 97-104.
206. Graydon, J. W.; Thorpe, S. J.; Kirk, D. W., Interpretation of Activation-Energies Calculated from Nonisothermal Transformation of Amorphous Metals. *Acta Metall. Mater.* **1994,** *42*, 3163-3166.
206. Sing, K. S. W.; Everett, D. H.; Haul, R. A. W.; Moscou, L.; Pierotti, R. A.; Rouquerol, J.; Siemieniewska, T., Reporting Physisorption Data for Gas Solid Systems with Special Reference to the Determination of Surface Area and Porosity. (Recommendation 1984). *Pure Appl. Chem.* **1985,** *57*, 603-619.
207. Khanday, W. A.; Majid, S. A.; Shekar, S. C.; Tomar, R., Dynamic Adsorption of DMMP over Synthetic Zeolite-Alpha. *Arabian J. Chem.* **2014,** *7*, 115-123.
208. Kanan, S. M.; Waghe, A.; Jensen, B. L.; Tripp, C. P., Dual WO_3 Based Sensors to Selectively Detect DMMP in the Presence of Alcohols. *Talanta* **2007,** *72*, 401-407.
209. Delafuente, G. F.; Huheey, J. E., The Synthesis and Characterization of Mixed (Alkylamino) and (Arylamino)phenylphosphonium Compounds. *Phosphorus, Sulfur Silicon Relat. Elem.* **1993,** *78*, 23-36.
210. Wilmsmeyer, A. R.; Uzarski, J.; Barrie, P. J.; Morris, J. R., Interactions and Binding Energies of Dimethyl Methylphosphonate and Dimethyl Chlorophosphate with Amorphous Silica. *Langmuir* **2012,** *28*, 10962-10967.
211. Dabrowski, A.; Podkoscielny, P.; Hubicki, Z.; Barczak, M., Adsorption of Phenolic Compounds by Activated Carbon - a Critical Review. *Chemosphere* **2005,** *58*, 1049-1070.
212. Fortier, H.; Zelenietz, C.; Dahn, T. R.; Westreich, P.; Stevens, D. A.; Dahn, J. R., SO_2 Adsorption Capacity of K_2CO_3-impregnated Activated Carbon as

a Function of K_2CO_3 Content Loaded by Soaking and Incipient Wetness. *Appl. Surf. Sci.* **2007,** *253*, 3201-3207.
213. Westreich, P.; Fortier, H.; Flynn, S.; Foster, S.; Dahn, J. R., Exclusion of Salt Solutions from Activated Carbon Pores and the Relationship to Contact Angle on Graphite. *J. Phys. Chem. C* **2007,** *111*, 3680-3684.
214. Ji, X. M.; Yao, W.; Peng, J.; Ren, N.; Zhou, J.; Huang, Y. P., Evaluation of Cu-ZSM-5 Zeolites as QCM Sensor Coatings for DMMP Detection. *Sens. Actuators, B* **2012,** *166*, 50-55.
215. Peterson, G. W.; Friday, D.; Shrewsbury, M. *Residual Life Indicator for Physical Adsorption Capacity of NBC Filters. Part I. Acetone Vapor Pulses and the Effect of Moisture Content on Retention Characteristics*; U.S. Army Research, Development and Engineering Command: Hunter Applied Research Center, **2008**.
216. Atteya, M.; Klabunde, K. J., Nanoscale Metal-Oxide Particles as Chemical Reagents - Heats of Adsorption of Heteroatom-Containing Organics on Heat-Treated Magnesium Oxide Samples of Varying Surface-Areas. *Chem. Mater.* **1991,** *3*, 182-187.
217. Kagel, R. O.; Greenler, R. G., Infrared Study of Adsorption of Methanol and Ethanol on Magnesium Oxide. *J. Chem. Phys.* **1968,** *49*, 1638.
218. Ma, S.; Zhou, J.; Kang, Y. C.; Reddic, J. E.; Chen, D. A., Dimethyl Methylphosphonate Decomposition on Cu Surfaces: Supported Cu Nanoclusters and Films on TiO_2(110). *Langmuir* **2004,** *20*, 9686-9694.
219. Smiechowski, M. F.; Feaver, W. B., AC Impedance Monitoring of Activated Carbon Filter Contamination. *Impedance Techniques: Diagnostics and Sensing Applications* **2012,** *41*, 57-67.
220. Bao, J. J.; Giurgiutiu, V.; Rubel, G. O.; Peterson, G. W.; Ball, T. M. In *Active Carbon Filter Health Condition Detection with Piezoelectric Wafer Active Sensors*, Conference on Sensors and Smart Structures Technologies for Civil, Mechanical, and Aerospace Systems 2011, San Diego, CA, Mar 07-10; San Diego, CA, **2011**.
221. Li, Y. X.; Schlup, J. R.; Klabunde, K. J., Fourier-Transform Infrared Photoacoustic-Spectroscopy Study of the Adsorption of Organophosphorus Compounds on Heat-Treated Magnesium-Oxide. *Langmuir* **1991,** *7*, 1394-1399.
222. Utamapanya, S.; Klabunde, K. J.; Schlup, J. R., Nanoscale Metal-Oxide Particles Clusters as Chemical Reagents - Synthesis and Properties of Ultrahigh Surface-Area Manesium Hydroxide and Magnesium-Oxide. *Chem. Mater.* **1991,** *3*, 175-181.
223. Wang, X.; Pan, D. H.; Xu, Q.; He, M.; Chen, S. W.; Yu, F.; Li, R. F., Synthesis of Ordered Mesoporous Alumina with High Thermal Stability using Aluminum Nitrate as Precursor. *Mater. Lett.* **2014,** *135*, 35-38.
224. Fan, J.; Boettcher, S. W.; Stucky, G. D., Nanoparticle Assembly of Ordered Multicomponent Mesostructured Metal Oxides via a Versatile Sol-Gel Process. *Chem. Mater.* **2006,** *18*, 6391-6396.

225. Brinker, C. J.; Lu, Y. F.; Sellinger, A.; Fan, H. Y., Evaporation-Induced Self-Assembly: Nanostructures Made Easy. *Adv. Mater.* **1999,** *11*, 579.
226. Long, J. W.; Logan, M. S.; Rhodes, C. P.; Carpenter, E. E.; Stroud, R. M.; Rolison, D. R., Nanocrystalline Iron Oxide Aerogels as Mesoporous Magnetic Architectures. *J. Amer. Chem. Soc.* **2004,** *126*, 16879-16889.
227. Gash, A. E.; Tillotson, T. M.; Satcher, J. H.; Hrubesh, L. W.; Simpson, R. L., New Sol-Gel Synthetic Route to Transition and Main-Group Metal Oxide Aerogels Using Inorganic Salt Precursors. *J. Non-Cryst. Solids* **2001,** *285*, 22-28.
228. Gash, A. E.; Tillotson, T. M.; Satcher, J. H.; Poco, J. F.; Hrubesh, L. W.; Simpson, R. L., Use of Epoxides in the Sol-Gel Synthesis of Porous Iron(III) Oxide Monoliths from Fe(III) Salts. *Chem. Mater.* **2001,** *13*, 999-1007.
229. Blochl, P. E., Pprojector Augmented-Wave Method. *Phys. Rev. B* **1994,** *50*, 17953-17979.
230. Kresse, G.; Hafner, J., Ab Initio Molecular-Dynamics for Liquid-Metals. *Phys. Rev. B* **1993,** *47*, 558-561.
231. Kresse, G.; Furthmuller, J., Efficient Iterative Schemes for Ab Initio Total-Energy Calculations Using a Plane-Wave Basis Set. *Phys. Rev. B* **1996,** *54*, 11169-11186.
232. Badri, A.; Binet, C.; Lavalley, J. C., Use of Methanol as an IR Molecular Probe to Study the Surface of Polycrystalline Ceria. *J. Chem. Soc. Faraday Trans* **1997,** *93*, 1159-1168.
233. Lamotte, J.; Moravek, V.; Bensitel, M.; Lavalley, J. C., FT-IR Study of the Structure and Reactivity of Methoxy Species on ThO_2 and CeO_2. *React. Kinet. Catal. Lett.* **1988,** *36*, 113-118.
234. Aurianblajeni, B.; Boucher, M. M., Interaction of Dimethyl Methylphosphonate with Metal-Oxides. *Langmuir* **1989,** *5*, 170-174.
235. Novakova, J.; Jiru, P.; Zavadil, V., Oxidation of Methanol and Formaldehyde on Fe_2O_3 in Comparison with MoO_3 and a Mixed $Mo^{6+}Fe^{3+}O$ Catalyst. *J. Catal.* **1971,** *21*, 143.
236. Morgan, B. J.; Watson, G. W., A DFT+U Description of Oxygen Vacancies at the TiO_2 Rutile (110) Surface. *Surf. Sci.* **2007,** *601*, 5034-5041.
237. Bandosz, T. J., On the Adsorption/Oxidation of Hydrogen Sulfide on Activated Carbons at Ambient Temperatures. *J. Colloid Interface Sci.* **2002,** *246*, 1-20.